III International Symposium

TOPICAL PROBLEMS OF BIOPHOTONICS

NANOBIOPHOTONICS

Chairs

Juergen Popp, Friedrich Schiller University of Jena; Institute for Photonic Technology, Germany

Konstantin (Kostia) Sokolov, UT M.D. Anderson Cancer Center; University of Texas at Austin, USA

Elena Zagaynova, Nizhny Novgorod Medical Academy, Russia

Program Committee

Tom Brown, University of St. Andrews, UK

Colin Campbell, School of Chemistry, University of Edinburgh, UK

Volker Deckert, Institute for Analytical Sciences, Germany

Sergey Deev, Institute of Bioorganic Chemistry RAS, Russia

Wolfgang Fritzsche, Institute for Photonic Technology, Germany

Stefan Hell, Max-Planck-Institute for Biophysical Chemistry, Germany

Sergey Lukyanov, Institute of Bioorganic Chemistry, Moscow, Russia; Nizhny Novgorod Medical Academy, Russia

Dennis Matthews, NSF Center for Biophotonics, University of California, Davis, USA

Alexander Savitsky, Institute of Biochemistry RAS, Russia

Victor Timoshenko, Moscow State University, Russia

Andrey Vasiliev, Koltzov Institute of Developmental Biology, Russia

Alexey Zheltikov, Moscow State University, Russia

OXIDATIVE PHOTOCONVERSION OF GFPs *IN VITRO* AND *IN VIVO*

A.M. Bogdanov[1], **A.V. Titelmaer**[1], and **K.A. Lukyanov**[1]

[1] M.M. Shemyakin and Yu.A. Ovchinnikov Institute of Bioorganic Chemistry RAS, Moscow, Russia
noobissat@ya.ru

The last 15 years in bioimaging can be characterized as the GFP era. Unusual properties of fluorescent proteins made them usual instruments for almost all branches of cellular and molecular biology and even biomedical researches. For a long time GFPs have been considered to be the passive light absorbers/emitters not involved in intermolecular biochemical interactions. Recently we showed that some members of GFP family can play a role of electron donors in redox-photoreactions with different compounds, including biologically relevant ones (Bogdanov et al., 2009). This process is accompanied by a green-to-red photoconversion, the so-called reddening. Reddening is a completely new type of FPs photoactivation that can occur in living systems, including tissues of transgenic animals without any additional treatments. Surprisingly, living cells demonstrated strong variability in their reddening "performance". We suppose that efficiency of the oxidative GFP photoconversion is a measure for the individual intracellular redox-state.

What was the starting point for this topic?

GFP photoactivation possibly occurring due to intermolecular interaction was first described in 1997 [1]. This phenomenon was represented by a weak green-to-red photoconversion observed in protein solutions and *E. coli* cells under low-oxygen conditions. There were not any reasonable ideas on the basic mechanism of the process and there wasn`t particular interest to it from the commercial point of view. In ten years, however, we made several steps to continue researches of low-oxygen photoactivation and obtain some data allowing to speak about its mechanism in terms of redox reaction where GFP chromophore plays a role of an electron acceptor [unpublished data]. While checking EGFP photobehaviour under different conditions we have accidentally encountered a new phenomenon. Green-to-red photoconversion took place in usual (aerobic) conditions in the presence of different electron acceptors. We called this new photoactivation "oxidative reddening".

Oxidative reddening

Reddening is a green-to-red photoconversion of EGFP and almost all known green fluorescent proteins occurring under intense blue irradiation in the presence of electron acceptors. EGFP`s red-shifted form has emission maximum at 607 nm. In this one-photonic reaction a GFP molecule donates two electrons to an acceptor molecule. Although reddening reaction intermediates haven`t been clearly detected yet, we suppose two-step process with the stable radical intermediate (this hypothesis is based on both experimental and computational data). We showed that oxidative photoconversion could be promoted by the wide spectrum of electron acceptors including biologically relevant ones. For example, it has been proved that EGFP can reduce oxidized cytochrome *c* and NAD^+ in solutions.

Surprisingly, we could easily detect red fluorescence appearance even in living mammalian cells transfected by EGFP-containing vectors. One can observe such a phenomenon using fluorescent microscopy without necessity to treat the cells with any additional compounds. Different cell lines (HeLa, PhoenixEco, HEK293, 3T3, LoVo, etc.) demonstrated strong variability in their relative reddening efficiencies. Moreover, each individual cell line showed significant internal heterogeneity in this respect. Thus, among individual HEK293 cells of the same passage we detected up to 10-fold difference in reddening relative efficiency. Finally, we found that intracellular compartments have their unique reddening profile [2]. Similar results were obtained in experiments with transgenic mouse fresh tissue slices, where the cells of particular specialization had individual reddening abilities. Taken together, these facts allow us to form the hypothesis that the oxidative GFP photoconversion efficiency can be used as a measure for an individual cellular redox-state.

We also found that the oxidative reddening can be induced *in vivo* in tissue of the coral polyp naturally producing GFPs. This remarkable observation forms the ground for some new ideas about fluorescent proteins natural function [2].

Surprisingly, GFPs redox reactions gave new information on the photostability problem. Our measurements showed that in case of living cells fluorescent imaging up to 90% of photobleaching is

connected to green-to-red photoconversion. To restrict reddening and additional bleaching, respectively, one needs to modify imaging medium by decreasing redox-active compounds` concentrations in it [3].

What's new?

The main goal of our recent works is to construct completely new molecular redox-sensors based on the reddening phenomenon. We are moving preferably in two directions. The first direction is to create the artificial electron-transfer chains which could potentially serve either as amplifiers of fluorescent response to redox-signal or optogenetical "modulators" of intracellular redox-events. At the moment, several constructs based on EGFP fused to flavodoxin and ribonucleotide reductase small subunit are ready. They show circa 10-fold higher redox-sensitivity compared to EGFP alone *in vitro*. The second direction is to study EGFP reddening in different model systems trying to find some correlations between the photoconversion profile and the physiological or functional cell state. For example, mouse embryonic stem cells (ES) cannot induce oxidative photoactivation at all. At the same time, we make new attempts to enhance photostability of the most popular GFPs in living cells visualization by modification of the imaging media.

Acknowledgements

Part of this work was supported by the MCB program of the Russian Academy of Sciences, Russian Federal Agency for Science and Innovations (grant 02.513.12.3013), HHMI grant 55005618, EC FP6 Integrated Project LSHG-CT-2003-503259, and the program "State Support of the Leading Scientific Schools" (NS-2395.2008.4). Current studies are also supported by the Russian Fundation for Basic Research (11-04-01861-a).

References

1. M.B. Elowitz, M.G. Surette, P.E. Wolf, J. Stock, S. Leibler, *Curr Biol.,* 1997, Oct 1, **7**(10), 809-12.
2. A.M. Bogdanov, A.S. Mishin, I.V. Yampolsky, V.V. Belousov, D.M. Chudakov, F.V. Subach, V.V. Verkhusha, S. Lukyanov, K.A. Lukyanov, *Nature Chem. Biol.,* 2009, **5**, 459-461.
3. A.M. Bogdanov, E.A. Bogdanova, D.M. Chudakov, T.V. Gorodnicheva, S. Lukyanov, K.A. Lukyanov, *Nature Methods*, 2009, **6**, 859-860.

Invited

SERS NANOSENSORS ENGINEERED TO MONITOR INTRACELLULAR REDOX POTENTIAL

C.A.R. Auchinvole, H. McNab, K. Donaldson, and **C.J. Campbell**

University of Edinburgh, Department of Chemistry
The King's Buildings, West Mains Road, Edinburgh, Scotland, EH9 3JJ
craig.auchinvole@ed.ac.uk; colin.campbell@ed.ac.uk

1. Introduction

Redox potential is a highly regulated, compartmentalised cellular property playing a key role in a host of cellular functions [1]. Perturbation of a cell's redox homeostasis by an increase in the generation of reactive oxygen species (ROS) or by a reduction in capability of the cell's antioxidant defences, such as glutathione [2] or thioredoxin [3] can have dire consequences. Redox disregulation to pro-oxidative states has been linked to a number of disease states including: cancers [4] cardiovascular diseases [5] and neurodegenerative diseases [6]. Despite this, current methods for measuring cellular redox potential are cumbersome [7], invasive [8] and destructive [9].

2. Results and Discussion

We have developed and implemented nanosensors based on surface enhanced Raman spectroscopy (SERS) to monitor the redox potential inside NIH3T3 fibroblast cells as they respond to reductive and oxidative stimuli. Our nanosensors utilise gold nanoshells (NS) functionalised with an array of substituted quinone molecules. These probe molecules possess SERS fingerprints sensitive to changes in oxidation state allowing them to report the quantities of oxidised and reduced species and thus calculate intracellular redox potential according to the Nernst equation. As well as being non-toxic, our strategy permits the quantitative measurement of intracellular redox potential over a wider potential range than the current 'gold standard' with unrivalled spatiotemporal resolution.

Through SERS spectroelectrochemistry (where nanosensors immobilised on the surface of microfabricated gold electrodes were subjected to varying potentials) a quantitative/ratiometric relationship between SERS fingerprint and oxidation state of quinone molecules has been demonstrated. Below is an example of our naphthoquinone nanosensor (NQ-NS).

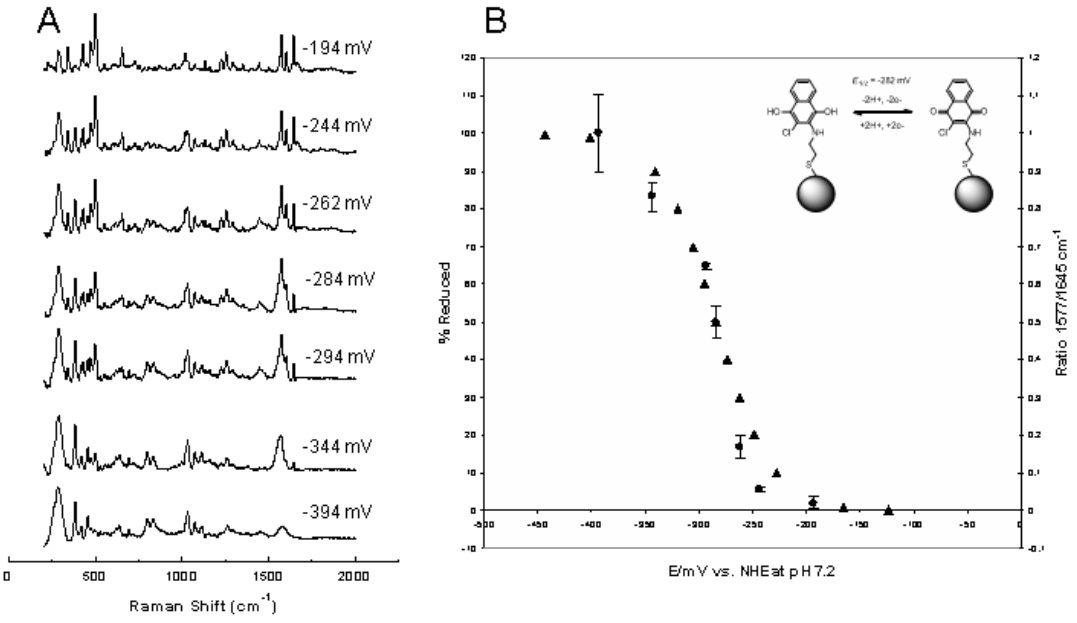

Fig. 1. A) SERS Spectroelectrochemistry of NQ-NS. **B)** Redox potential range covered by NQ-NS. Error bars show the standard deviation of three independent measurements. Points indicate SERS spectroscopic measurements and triangles represent plots of the Nernst Equation on the basis of half-wave potentials measured using cyclic voltammetry

Cytoplasmic redox potential has been measured accurately and in real-time as it changes in response to the reductant dithiothreitol (DTT) and ROS generator 2, 2'- azobis- 2- methyl-propanimidamide, dihydrochloride (AAPH).

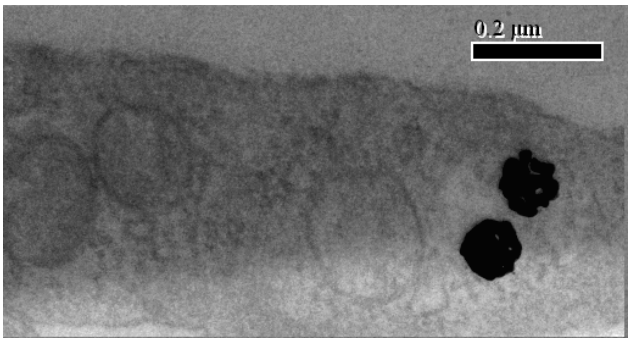

Fig. 2. TEM image of nanosensors in the cytoplasm of NIH3T3 fibroblast cells

SERS nanosensors present a new and exciting tool for the measurement of intracellular redox potential. They are non-toxic, tuneable and robust in their function. With these nanosensors the potential for targeted organelle delivery exists as does the opportunity to use them in diagnosis and indeed to better understand the role redox disregulation plays in harming cells.

3. Acknowledgements

The authors would like to thank the University of Edinburgh School of Chemistry for funding. They also acknowledge the technical contributions of Professor Hamish McNab (University of Edinburgh).

References

1. S.G. Menon and P.C. Goswami, "A redox cycle within the cell cycle: ring in the old with the new", *Oncogene*, 2007, **26**, 1101-1109.
2. F.Q. Schafer and G.R.Buettner, "Redox state of the cell as viewed through the glutathione disulfide/glutathione couple", *Free Radic Biol Med*., 2001, **30**, 1191-1212.
3. J. Nordberg and E. Arnér, "Reactive oxygen species, antioxidants, and the mammalian thioredoxin system", *Free Radic. Biol. Med.*, 2001, **31**, 1287–312.
4. B. Halliwell, "Oxidative stress and cancer: have we moved forward?", *J. Biochem*., 2007, **401**, 1-11.
5. S. Parthasarathy, N. Khan-Merchant, M. Penumetcha, and N. Santanam, "Oxidative stress in cardiovascular disease", *J. Nucl. Cardiol*., 2001, **8**, 379-389.
6. K.J. Barnham, C.L. Masters, and A.I. Bush, "Neurodegenerative diseases and oxidative stress", *Nat. Rev. Drug Discov*., 2004, **3**, 205-214.
7. G.T. Hanson, R. Aggeler, D. Oglesbee, M. Cannon, R.A. Capaldi, R.Y. Tsien, and S.J. Remington, "Investigating mitochondrial redox potential with redox-sensitive green fluorescent protein indicators", *J. Biol. Chem*., 2004, **279**, 13044-13053.
8. N.C. Smith, M. Dunnett, P.C. Mills, "Simultaneous quantitation of oxidised and reduced glutathione in equine biological fluids by reversed-phase high-performance liquid chromatography using electrochemical detection", *J. Chromatogr. B*, 1995, **673**, 35-41.
9. M.E. Anderson, "Determination of glutathione and glutathione disulfide in biological samples", *Methods Enzymol*., 1985, **113**, 548-555.

Invited

PLASMONIC BIOCHIPS – FROM INSTRUMENTATION TO NANO-MICRO-STRUCTURED SUBSTRATES

M. Canva, A. Bellemain, and **J. Moreau**

Laboratoire Charles Fabry de l'Institut d'Optique
Institut d'Optique Graduate School, Univ Paris Sud, CNRS - Palaiseau, France
michael.canva@institutoptique.fr

Introduction

Propagating plasmons are electromagnetic mode which are located at a metal:dielectric interface. As they are very sensitive to minute changes in the optical index of the dielectric in the vicinity of the metal, they have been widely used as basis of optical sensing systems. Such systems allow precise monitoring of binding and unbinding reactions of biomolecular targets with probe-biofunctionalized surface. Such characterization method does not require any labeling procedure and allows access to the dynamical data of the surface temporal evolution. Originally used as single or multi-channel systems, this technique has been upgraded, about a decade ago, using optical imaging system to allow parallel large field surface characterization. This field is known as surface plasmon resonance biochips.

Plasmonic imaging systems

We have developed, over the years, quite a variety of surface plasmon resonance imaging (SPRI) systems, ranging from the "classical", with fixed wavelength and angle, recording changes in reflectivity $R(x, y, t)$ – x and y being the spatial coordinate on the biochip surface, and t the time – to more sophisticated systems capable of monitoring a larger voxel of information as $R(x, y, t, \theta, \lambda, P)$ – θ being the coupling angle of incidence of the illuminating beam and λ its tunable wavelength, P representing the direction of propagation in dual system capable of quantifying anisotropy within the dielectric medium – our last system even adding the possibility to characterize the chip using conventional microscopy from above $M(x, y, t)$.

Biochips and biomedical applications

Such systems are indeed very sensitive to minute changes in the dielectric material placed in direct contact, with tens of nanometers, of the metal film. In association with proper gold film biofunctionalization and structuration, SPRI has been used for biochip applications. The substrate usually consist of a 50 nm gold film. Different chemistries have been used, most starting with a thiol-functionalized molecule binding to the gold and ending with an avidin-functionalized surface where biotin-functionalized probe molecule can be spotted onto. Such biochips have proven to work for many different applications; we will detail our model case of DNA:DNA interactions and application to medical molecular genotyping diagnostic of hereditary disease cystic fibrosis, discriminating single Nucleotide Polymorphism (SNP) for the three possible genotypes (homozygote wild, homozygote muted and heterozygote).

Towards structuration

As pointed out recently by M. Piliarik and J. Homola in a paper, precisely entitled "Surface Plasmon Resonance sensors: approaching their limits?" [Optics Express 17, 16505 (2009)], such plasmonic sensors systems based on propagating plasmon (PP) on homogeneous thin metallic film are close to their maximum performances in terms of sensitivity. On another hand, much work has been devoted by the community to sensing using metal nano-particles based on localized plasmons (LP), with some advantages and disadvantages. We are targeting the study of the intermediate regime ranging from quasi propagating plasmon (QPP) to coupled localized plasmons (QLP). Together with our partners, we focus on their potential use as plasmonic sensing substrates, evaluating the different structures angulo-specral reflectivities as well as change in reflectivities.

Nano-Micro-structured biochip simulation

Simulations make use of different numerical codes based on RCWA (Rigorous Coupled Wave Analysis), FDTD (Finite Difference Time Domain) as well as hybrid using coupled Finite Element Method and Fourier Modal Method (FEM + FMM) modeling.

Nano-Micro-structured biochip substrates realization

Samples we investigate are being made by a variety of lithographic techniques including e-beam, deep UV, sphere, soft imprint, … and structure details vary within the nanometer to micrometer range on areas sub-millimeter wide organized onto centimeter sized chips.

Plasmonic characterization

The angulo-spectral imaging set-up is the best suited for these plasmonic investigations as it allows characterizing in parallel tens of different structures and their behaviors as index and thin-film sensors in identical conditions. The angulo-spectral range allows accessing the different resonant positions of each individual structure.

Conclusions and perspectives

Plasmonic biochip systems have substantially improved over the past decade and reached market and end-user applications. However, as always, improved performances are required in order to meet new demands in sensitivity, in lowering the amount of probe and especially target material required, in accessing higher total throughput of molecular characterization at lower cost, in time and consumables, … thus initiating news studies requiring fundamental and applied understanding, in particular in the fields of plasmonics and chemistry, applying to sensors and associated biochips.

Acknowledgements

The authors acknowledge numerous collaborations in these topics especially including Michel Goossens *et al.* from Hospital Henri Mondor in Créteil, France as well as past and current group members. Institut d'Optique graduate school (IOGS), CNRS is a core member of the European Network of Excellence in Biophotonics, Photonics for Life, P4L.

Author's References

1. M. Nakkach, A. Duval, B. Ea-Kim, J. Moreau, and M. Canva, "Angulo spectral surface plasmon resonance imaging of nanofabricated grating surfaces", *Optics Letter*, 2010, **35**(13), 2209-2211.
2. F. Bardin, A. Bellemain, G. Roger, and M. Canva, "Surface plasmon resonance spectro-imaging sensor for biomolecular surface interaction characterization", *Biosensors and BioElectronics*, 2009, **24**, 2100-2105.
3. J. Hottin, J. Moreau, G. Roger, J. Spadavecchia, M.C. Millot, M. Goossens, and M. Canva, "Plasmonic DNA: towards genetic diagnosis chips", *Plasmonics*, 2007, "Plasmonics and DNA" special issue, **2**, 201-215.
4. P. Lecaruyer, E. Maillart, M. Canva, and J. Rolland, "Generalization of the Rouard method to an absorbing thin film stack and application to surface plasmon resonance", *Applied Optics*, 2006, **45**, 8419-8423.
5. A. Duval, A. Laisné, D. Pompon, S. Held, A. Bellemain, J. Moreau, and M. Canva, "Polarimetric surface plasmon resonance imaging biosensor", *Optics Letter*, 2009, **34**(23), 3634-3636.
6. Dhawan, A. Duval, M. Nakkach, G. Barbillon, J. Moreau, M. Canva, and T. Vo-Dinh, "Deep UV Nano-Micro-Structuration of Substrates for Surface Plasmon Resonance Imaging", *Nanotechnology*, 2011, **22**, 165301.
7. I. Mannelli, V. Courtois, P. Lecaruyer, G. Roger, M.C. Millot, M. Goossens, and M. Canva, "Surface plasmon resonance imaging (SPRI) system and real-time monitoring of DNA biochip for human genetic mutation diagnosis of DNA amplified samples", *Sensors and Actuators* B, 2006, **119**, 583-591.

Invited

NANODIAMOND USED FOR BIO IMAGING AND DRUG DELIVERY

C.-L. Cheng[1], **E. Perevedentseva**[1, 3], **A.V. Logoustov**, and **A.V. Priezzhev**[2]

[1] Department of Physics, National Dong Haw University, Hualien, Taiwan, clcheng@mail.ndhu.edu.tw
[2]International Laser Center, Moscow State University, Moscow, Russia
[3]P.N. Lebedev Institute of Physics, Russian Academy of Science, Moscow, Russia

Nanodiamond (ND) is emerging to be an important nanomaterial for bio- and medical applications due to their superb physical and chemical properties. The recent proved biocompatibility renders ND promising application in bio systems. In this report, we will demonstrate several cases of using ND as an effective bio label for biomolecules interaction with cells or bio objects. Biomolecules can be immobilized onto diamond surface via various chemical/physical methods. Spectroscopic methods, such as IR and Raman spectroscopy, can be used to characterize the immobilization of bio molecules on ND surfaces. The intrinsic defect-related N-V color centers in ND give rise to fluorescence signals can be used for imaging. In addition, the carbon sp^3 Raman spectral signal of ND (at 1332 cm^{-1}) provides another spectral marker for imaging. The application of nanometer-sized diamond used as Raman detectable bio- labeling was realized [1]. To demonstrate this, protein lysozyme-ND complexes were produced. The interaction of lysozyme-ND complex with bacteria *E. coli* was observed via Raman mapping using diamond Raman signal as the labeling marker. The results are compared with scanning electron microscope observation; and the adsorbed lysozyme's functionality was analyzed. High antibacterial activity of lysozyme-nanodiamond complex was observed, equivalent to active lysozyme in solution. The results suggest nanodiamond labeling can be effective and applied in ambient condition without complicate sample pre-treatments. With this result, we propose to use nanodiamond as a biocompatible nanoparticle for bio labeling of bio molecule's interaction with cells or bio objects. These applications utilizing ND's spectroscopic properties, such as unique Raman signal and its natural fluorescence, as bio markers to probe the interactions of bio molecules with cell and bacteria in the single cellular level; in the same time ND serves as transportation vehicle for the bio molecules. Further, ND can be developed into an efficient drug delivery vehicle for more safe and efficient drug delivery/release [2].

Different methods were developed to functionalize the surface of nanodiamond with various functional groups, which allow further conjugation with bio molecules via either physical (electrostatic interaction) or chemical (covalent bonding) interactions. For this purpose, the surface spectroscopy of nanodiamond is analyzed using infrared and Raman spectroscopy. The biocompatibility, ND interaction with cells and detection are evaluated for various sizes NDs on human lung A549 epithelial cells and HFL-1 normal fibroblasts. Results find ND did not reduce the cell viability and alter the protein expression profile in the test cells. The developed ND-biomolecule conjugate serves as a nano-bio-probe to label bio-interaction. We successfully used nanodiamond to label the interaction of growth hormone (GH) and growth hormone receptor (GHR) on human lung cancer cell (A549) membrane surface [3].

To apply ND in animal or human models, the interaction of ND with blood system demands careful study. For this purpose, we studied the interaction of different sizes NDs with several blood elements, including human red blood cells (RBC) and blood proteins such as hemoglobin (Hb), human serum albumin and gamma-globulin. The NDs influence on blood's oxygenation/deoxygenation, and microrheology, in particular, the ability of RBCs to deform in shear flow and to spontaneously aggregate in whole blood were examined. Raman results indicate some size-dependent effects of the RBC oxygenation/deoxygenation time upon ND interaction, and the effects depend on the process conditions (pH, deoxygenating gas flow, partial pressure, etc.). Raman results imply 100 nm ND in physiological condition does not cause conformational changes for hemoglobin; neither does it induce observable hemolysis of RBC. However, there is a concentration dependent negative effect of NDs on both deformability and aggregation kinetics of RBCs. In particular, smaller NDs (5 nm) in lower concentrations decrease the formation time of both linear and 3D RBC aggregates and enhance the amplitude of spontaneous RBC aggregation in whole blood, which are overall negative physiologic effects. The effect is attributed to nonpenetration of large ND aggregates into the RBCs through their membranes. The RBC deformability index is reduced all through the range of tested shear stresses

(from 3 to 60 Pa). The reduction increased at higher concentrations (100 μg/ml). Given the nanoparticles are to be delivered to the targets in most biomedical applications via the blood flow, our studies are indicative of the importance of thorough studies of the effect of NDs on blood rheologic properties. Our results in general suggest that optimal conditions for ND bio-applications can be selected.

The issue of potential toxicity of nanomaterial has been the major concern, although nanoparticles were intensively developed for biomedical applications. A non-toxic and biocompatible nanomaterial is required for clinical use. Recently, the intravenous injection of ND particles into mice did not significantly induce symptoms of abnormality. As a result, ND is a relative safe nanomaterial based on its non-cytotoxicity and biocompatibility; however, further rigorous evaluation before clinical applications is needed. Furthermore, ND is a detectable nanomaterial using its fluorescence property but without photobleaching. We have shown that ND can be used for the labeling and tracking of cancer cells. Accordingly, the properties of biocompatible and detectable ND are very useful for biomedical applications. In another test case; we manipulated nanodiamond to covalently link anti cancer drug paclitaxel for cancer drug delivery and therapy. Treatment with 0.1-50 μg/mL ND-paclitaxel for 48 h significantly reduced the cell viability in the A549 human lung carcinoma cells. ND-paclitaxel induced both mitotic arrest and apoptosis in A549 cells. However, ND alone or denatured ND-paclitaxel did not induce the damage effects on A549 cells. In an animal test, ND-paclitaxel markedly blocked the tumor growth and formation of lung cancer cells in xenograft SCID mice. Together, we provide a functional covalent conjugation of ND-paclitaxel, which can be delivered into lung carcinoma cells and preserves the anticancer activities on the induction of mitotic blockage, apoptosis, and anti-tumorigenesis [4]. We provide a functional ND-paclitaxel conjugate developing for novel strategy on cancer drug delivery and therapy.

The success of these experiments demonstrated nanodiamond's great potential in bio/medical applications; based on the properties of uptake ability, delectability and little cytotoxicity in human cells.

Acknowledgements

The authors would like to thank the National Science Council for financially supporting this project under a National Nano Science and Technology Program, No. NSC-(97-99)-2120-M-259-001 and a joint collaboration project between Taiwan (NSC) and Russia (RFBR) under a grant No. NSC-97-2923-M-259-001-MY3.

References

1. E. Perevedentseva, C.-Y. Cheng, P.-H. Chung, J.-S. Tu, Y.-H. Hsieh, and C.-L. Cheng, *Nanotechnology*, 2007, **18**, 315102.
2. J.-I. Chao, E. Perevedentseva, P.-H. Chung, K.-K. Liu, I.-L. Hsu, C.-Y. Cheng, C.-C. Chang, C.-L. Cheng, *Biophysical J*., 2007, **93**, 2199-2208.
3. C.-Y. Cheng, E. Perevedentseva, J.-S. Tu, P.-H. Chung, C.-L. Cheng, K.-K. Liu, J.-I. Chao, P.-H. Chen, C.-C. Chang, *Appl. Phys. Lett*., 2007, **90**, 163903.
4. J.-I. Chao, W.-W. Zheng, K.-K. Liu, Y.-C. Chiu, C.-L. Cheng, Y.-S. Lo, C. Chen, *Nanotechnology*, 2010, **21**(31), 315106.

FLUORESCENCE IMAGING OF THE TUMOR – MESENCHIMAL STEM CELLS INTERACTION

E.I. Cherkasova[1], E.A. Minakova[1], M.V. Shirmanova[1], E.V. Kiseleva[2], E.B. Dashinimaev[2], M.S. Kleshnin[3], E.A. Sergeeva[3], I.V. Turchin[3], and **E.V. Zagaynova[1]**

[1] N.I. Lobachevsky University of Nizhny Novgorod, Russia, cherkasova.el@yandex ru
[2] N.K. Koltsov Institute of Developmental Biology RAS, Moscow, Russia
[3] Institute of Applied Physics RAS, Nizhny Novgorod, Russia

The goal of the research is investigation of the interactions in the "recipient–tumor–stem cells (SC)" system by the methods of *in vivo* fluorescence bioimaging using tagged stem cells with fluorescent proteins of different origin.

First of all the sensitivity of the surface fluorescence imaging device to small fluorophore concentrations was studied. Toward this end, fluorescence of proteins of different concentration was observed. After that the "recipient–tumor–SC" system was investigated in animal experiments.

In vivo fluorescence imaging was performed on the experimental setup for surface bioimaging (Institute of Applied Physics RAS, Nizhny Novgorod) in which a studied object is illuminated by a narrow-band source of optical radiation (light diodes) and fluorescence is registered by a cooled CCD-camera (Hamamatsu, Japan), with the radiation exciting fluorescence being cutoff by the interference filters. The setup had original software for image processing.

Preliminary observation of Green fluorescent protein (GFP) and Red fluorescent protein (subcutaneous) (Evrogen, Moscow) fluorescence with subcutaneous injection into nonlinear mice showed that minimal concentration detected by the experimental setup for surface bioimaging was about 0.3 and 0.1 mkg, respectively (fig. 1). Therefore, in the subsequent main studies we used RFP TurboFP635(588/635) with absorption maxima and emission at 585 and 635 nm, respectively, in the region of biotissue transparency window.

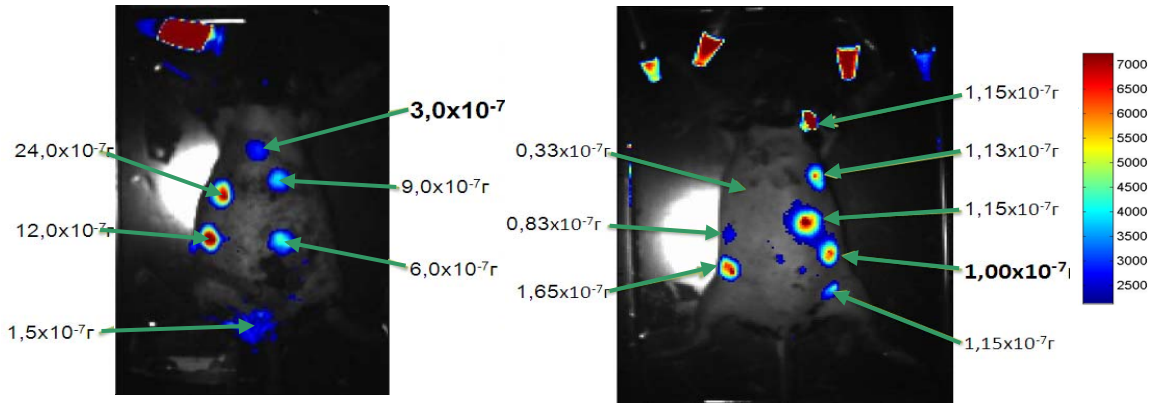

Fig. 1. Results of observation of different concentrations of GFP (a) and RFP (b). Injection sites are shown by arrows; relative fluorescence intensity scale is on the right; estimates of the minimal concentration observed by the described method is boldfaced

We used in our work two types of stem cells transfected with the gene of fluorescence protein Turbo FP635(588/635): mesenchimal adipose-derived adult stem (ADAS) cells and amniotic fluid-derived stem (AFS) cells of humans. The cells were liposome transfected using a vector plasmid design (Evrogen, Moscow).

The objects of research were nude female mice with transplanted tumor SKOV-3 (ovarian adenocarcinoma) with intravenously and topically injected tagged stem cells. Intact mice of the same strain were used for control.

Stem cells (ADAS, AFS) with the concentration of $3x10^6$ in 150µl PBS were injected into the experimental animals with tumor models at different stages of angiogenesis (14–28 days). The fluorescent signal was detected every 3 days for 40 days on the experimental setup for surface fluorescence imaging.

Results of image processing did not show unambiguous localization of fluorophore tagged stem cells. Insufficient sensitivity of the technique has several causes: deep localization of the stem cells injected into the animal organism (more than 3 mm from the surface), insufficient amount of stem cells in the growth sites, and self-fluorescence of tissues in the marker protain fluorescence range. The sensitivity of the technique may be improved by spectral separation self-fluorescence and fluorescence of stem cells.

We compared results obtained on the setup for surface bioimaging and those of fluorescence microscopy ex vivo on the setup for confocal laser scanning microscopy Axiovert 200M LSM 510 META (Carl Zeiss, Germany). We investigated internal organs of animals (liver, spleen, brain, intestines, lungs, heart, kidneys, skin, marrow) and tumor tissues. The obtained images were processed with the Zeiss LSM Image browser software, version 4.0.0.91. It was shown that with intravenous injection of AFS, bright fluorescent structures with spectral characteristics corresponding to TurboFP635(588/635) protein are locally accumulated in the marrow and tumor tissues of animals (fig. 2).

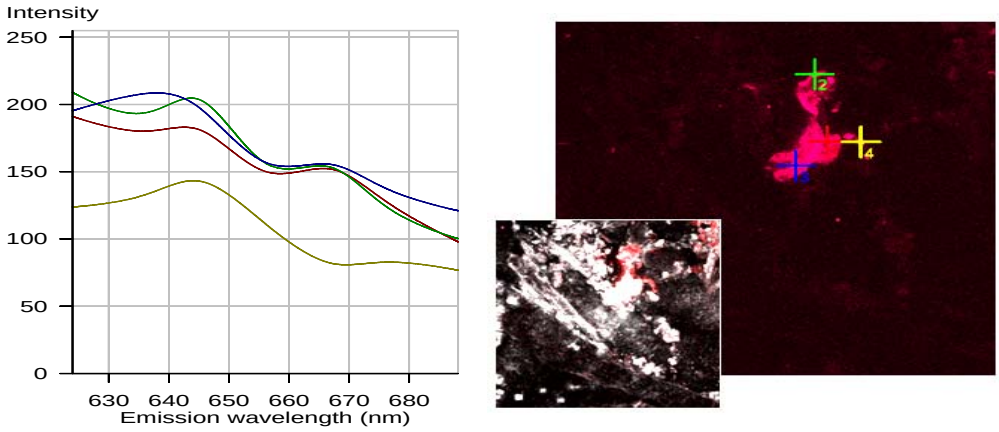

Fig. 2. Results of fluorescence microscopy of the marrow of experimental animals. Left – spectra of fluorescent points labeled by crosses of analogous color on the right. Right – fluorescence images (624-688 nm channel) and smaller images resulting from superposition of images in reflected light and in the fluorescence mode

Thus, it was found that stem cells of at least one type – AFS – integrate in the animal organism with transplanted tumor, but because of deep localization and weak signal they cannot be identified by the surface bioimaging techniques. It is expected that further studies will enable using other, more organic models of the tumor–stem cell interaction and developing more efficient software for processing results obtained using the surface fluorescence imaging setup.

Acknowledgements

This work was partly supported by the Russian Foundation for Basic Research (10-02-01109, 11-02-01199), by the Science and Innovations Federal Russian Agency (projects 02.740.11.0086, 16.512.11.2140, 16.120.11.1909-MK), and by the Program of Fundamental Researches of the Presidium of the Russian Academy of Sciences.

Invited

PROTEIN SELF-ASSEMBLER FOR SYNTHESIS OF MULTIFUNCTIONAL HETEROSTRUCTURES

S.M. Deyev

Shemyakin & Ovchinnikov Institute of Bioorganic Chemistry, Miklukho-Maklaya str., 16/10
117997 Moscow, Russia; e-mail: deyev@ibch.ru

This study is aimed at designing a panel of uniform particulate biochemical reagents and testing them in specific bioassays. Standard procedures for design of targeted imaging and therapeutic compounds are based on an attachment of recognizing molecules to visualizing agents or drugs. In the frame of this approach the fully genetically encoded anti-receptor antibody-photosesitizer [1] and immunoRNase [2] were constructed. A fluorescent protein, Killer Red, and a ribonuclease barnase were used as toxic principles. They were fused to the single-chain scFv-fragment of anti-HER2/neu antibody 4D5 that recognizes the extracellular domain of cancer marker HER2. Both bifunctional fusion proteins demonstrated specific cytotoxic effect on HER2-positive human carcinoma cells.

A novel strategy for design of heterostructures based on the ribonuclease barnase and its inhibitor, barstar, was suggested [3, 4]. Avidin and biotin are widely used in immunoassays as a universal linker between an antibody and a contrast agent. But the eukaryotic origin of the avidin and biotin often results in false-positive background signals in human protein-assays due to non-specific binding. We report on the quantitation of such a background signal under several assay conditions. We find that the background signal in such assays exhibits high fluctuation. Prokaryotic barstar and barnase on the other hand prove to be immune to such non-specific background signals, promising an alternative to avidin and biotin in performing such assays, with an improved and reproducible signal to noise factor.

The barnase and barstar are small, stable, very soluble, resistant to proteases proteins. The complex between them is extremely tight with $K_d \sim 10^{-14}$ M. The N- and C-terminal parts of both proteins are localized outside of the barnase·barstar interface and are therefore accessible for fusion with targeting, visualizing or toxic compounds. The fusions thus constructed, anticancer miniantibodies-barnase (scFv-barnase or scFv-dibarnase) and scFv-barstar, then form extremely stable dimers (or trimers) due to the practically irreversible pairing of the ligands through their native interface. It was shown that the constructed oligomers provide effective delivery of radioisotope to the xenografted HER2/neu overexpressing human adenocarcinoma SKOV3 in mice. The barnase fusion with fluorescent protein EGFP was used for visualization of cancer cells by assembling two fusion proteins, EGFP-barnase and anti-HER2/neu scFv-barstar. Efficient killing of cancer was achieved when instead of fluorescent protein the toxic agent, pseudomonas exotoxin A, was linked to barstar and assembled with anticancer scFv-barnase. The suggested strategy is applicable to virtually any proteins that can be functionally attached to the barstar and barnase molecules. It seems particularly well suited to the production of heterooligomeric constructs because the extremely specific barnase·barstar interaction eliminates reliably the mispairing problems. The important advantage of barnase·barstar over the majority of other dimerization modules is that their interaction ratio is precisely 1:1, and neither of the partners is aggregation prone.

To describe the "Protein-assisted NanoAssembler" method, we would like to introduce the following glossary: individual single-functional particles are *conjugated* with one of the proteins (barnase or barstar) to form *modules*; modules are *assembled* together to form *superstructures*. Since the link between the modules is mediated by proteins and is very strong or quazicovalent, we say that the assembly is specific or *protein-assisted* to distinguish from ordered packing or ordinary agglomeration.

The presented concept was tested with the use of scFv antibody fragments that were recombinantly fused to barstar and barnase, while inorganic nanoparticles – colloid gold, semiconductor nanocrystals [5], magnetic particles [6], polymer particles (150 – 800 nm) [7, 8] – were linked to partner proteins, barnase and barstar, respectively. A high efficiency and specificity of the labeling were achieved in all the listed cases. The assembly has demonstrated that the bond between these proteins is strong enough to hold macroscopic (5 nm – 1μm) particles together. The properties of the assembled superstructures can be programmed on demand by linking different agents designated for specific goals (Figure).

This universal platform provides a straight-forward technology to design a multifunctional nanoheterostructures "when the whole is greater than the sum of the parts".

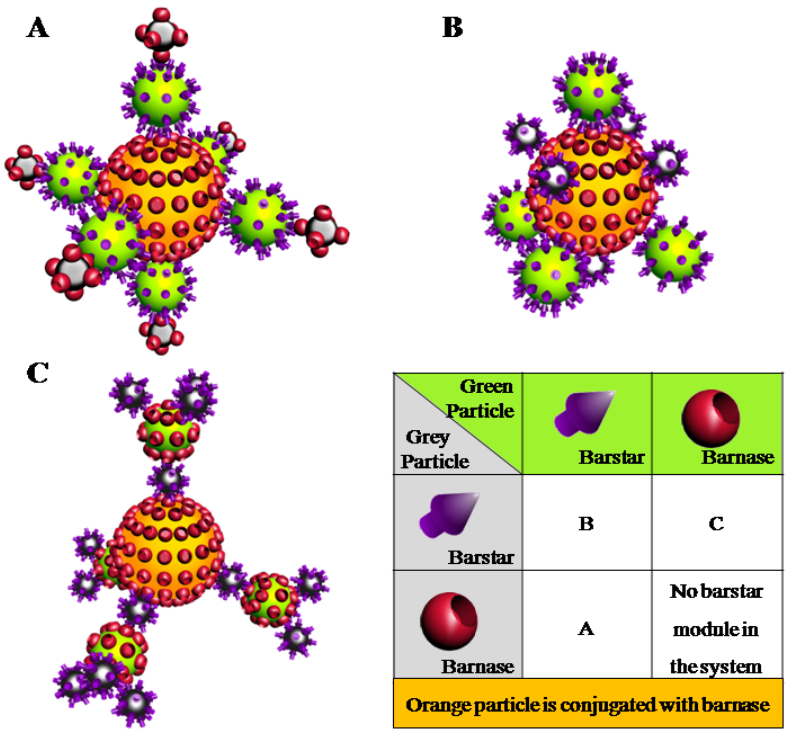

Possible variants for assembling three particles into a superstructure by the "Protein-assisted NanoAssembler" method. Correspondence of different combinations of BBS proteins conjugated with the green and grey particles and the structure number (*A, B, C*) is shown in the table. Barnase is chosen as the protein conjugated with the core orange particle

The work was supported by the Russian Academy of Sciences Programs Molecular & Cellular Biology and Nanotechnologies & Nanomaterials, the Russian Foundation for Basic Research Grants No. 09-04-01201, the Russian Federal Agency for Science and Innovation.

References

1. E.A. Serebrovskaya, E. Edelweiss, O. Stremovskiy, K. Lukyanov, D. Chudakov, and S.M. Deyev, *Proc. Natl. Acad. Sci. USA*, 2009, **106**, 9221-9225.
2. E. Edelweiss, T.G. Balandin, J.L. Ivanova, G.V. Lutsenko, O.G. Leonova, V.I. Popenko, A.M. Sapozhnikov, and S.M. Deyev, *PLoS ONE,* 2008, **3,** e2434.
3. S.M. Deyev, R. Waibel R., E.N. Lebedenko, A.P. Schubiger, and A. Plückthun, *Nat. Biotechnol*., 2003, **21**, 1486-1492.
4. S.M. Deyev and E.N. Lebedenko, *BioEssays,* 2008, **30**(9)**,** 904-918.
5. T.A. Zdobnova. S.G. Dorofeev, P.N. Tananaev, R.B. Vasiliev, T.G. Balandin, E.F. Edelweiss, O.A. Stremovskiy, I.V. Balalaeva, I.V. Turchin, E.N. Lebedenko, V.P. Zlomanov, and S.M. Deyev, *J. Biomed. Opt.*, 2009, **14**, 021004.
6. M.P. Nikitin, T.A. Zdobnova, S.V. Lukash, O.A. Stremovskiy, and S.M. Deyev, *Proc. Natl Acad. Sci. USA,* 2010, **107**(13), 5827-5832.
7. V.K.A. Sreenivasan, E.A. Ivukina, W. Deng, T.A. Kelf, T.A. Zdobnova, S.V. Lukash, B.V. Veryugin, O.A. Stremovskiy, A.V. Zvyagin, and S.M. Deyev, *J. Materials Chemistry,* 2011, **21**(1), 65-68.
8. A.N. Generalova, S.V. Sizova, T.A. Zdobnova, M.M. Zarifullina, M.V. Artemyev, A.V. Baranov, V.A. Oleinikov, V.P. Zubov, and S.M. Deyev, *Nanomedicine*, 2011, **6**(2), 195-209.

THE COMBINED INFLUENCE OF GOLD NANOPARTICLES AND LASER RADIATION ON CANCER CELLS *IN VITRO*

V.V. Elagin[1,2], **A.A. Brilkina**[2], **E.A. Sergeeva**[3], **M.A. Bugrova**[1], **V.A. Nadtochenko**[4], and **E.V. Zagaynova**[1]

[1] Nizhny Novgorod State Medical Academy, Russia, elagin.vadim@gmail.com
[2] Nizhny Novgorod State University, Russia
[3] Institute of Applied Physics of the Russian Academy of Sciences, Nizhny Novgorod, Russia
[4]N.N. Semenov Institute of Chemical Physics RAS, Moscow, Russia

In recent years researches in the field of nanotechnologies have been actively developed. A huge amount of nanoparticles with different shapes and structures have been obtained from different materials. Gold nanoparticles attract the greatest interest. Gold nanoparticles are known to have hypotoxicity and high compatibility with internal environment. Therefore, they may be used in biomedical applications. Moreover, high absorption and scattering coefficients of nanoparticles enable their use as diagnostic agents. Nanoparticles surfaces can be easily conjugated with specific macromolecules, such as polyethylene glycol, folic acid and an antibody. This property is extremely useful for target delivery. High efficiency of converting light energy to heat allows nanoparticles application as thermal-sensitizing agents for laser hyperthermia.

Therefore, the work is devoted to an integrated study of the interaction between gold nanoparticles and cancer cells using high-resolution microscopy techniques. In addition, another goal of the study is to assess efficacy of laser treatment with gold nanoparticles to destroy cancer cells.

The work was carried out on human ovarian adenocarcinoma SKOV-3 cells. The gold nanorods used in this work had a plasmon resonance peak at 75 nm. The nanoparticles surfaces were coated with polyethylene glycol with 6000 and 40000 D molecular weight. The interaction between the nanoparticles and cells was investigated by the transmission electron microscopy (TEM) and two-photon luminescence microscopy techniques. Nonlinear excitation of luminescence was stimulated by a 770 nm femtosecond laser, but luminescence registration was detected in the 565-615 nm range. The cells were treated by a 810 nm cw laser with the output power of 0.5–3 W for 10 min. The cells viability was estimated by MTT.

First, the efficiency of the light-heat conversion of different nanoparticles types (2 types of nanoshells and one of nanorods) was assessed. The gold nanoparticles solutions were treated at 3 W for 2 min. Then the temperature increase was estimated. The maximum temperature increase was registered for the gold nanorods (49°C), whereas the temperature increase for the nanoshells was 42°C (fig. 1). That is why the gold nanorods were chosen for the future studies.

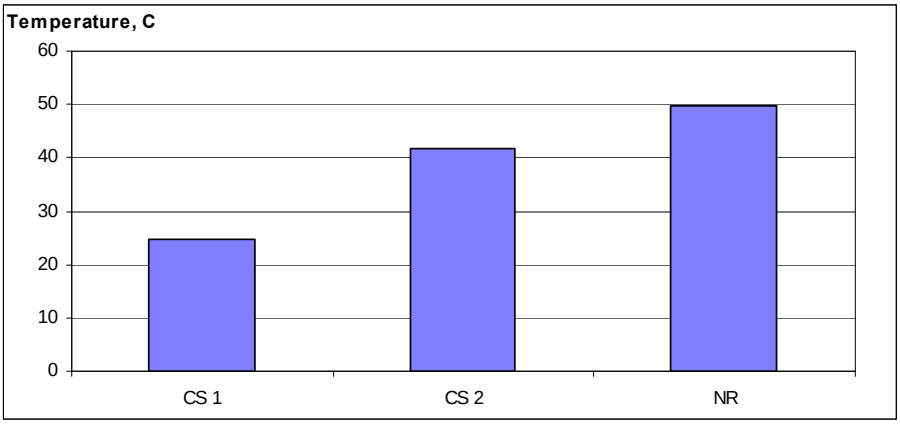

Fig. 1. Efficiency of light-heat conversion

The next stage included investigation of gold nanorods penetration into cells. The cells were grown in 96-well plates. After 1 hour incubation with the gold nanoparticles solution the cells were rinsed 3 times with the phosphate-buffered saline from the unbound nanoparticles. Finally, the samples were analyzed by microscopic techniques or were treated by a laser.

A huge amount of the gold nanoparticles coated with PEG-6000 were found to penetrate into the cells. Also the gold nanoparticles were detected on the cells outer surfaces. The gold nanoparticles coated with PEG-40000 did not penetrate into the cells and were located on the outer side of the plasma membrane. These results were confirmed by transmission electron microscopy (fig. 2).

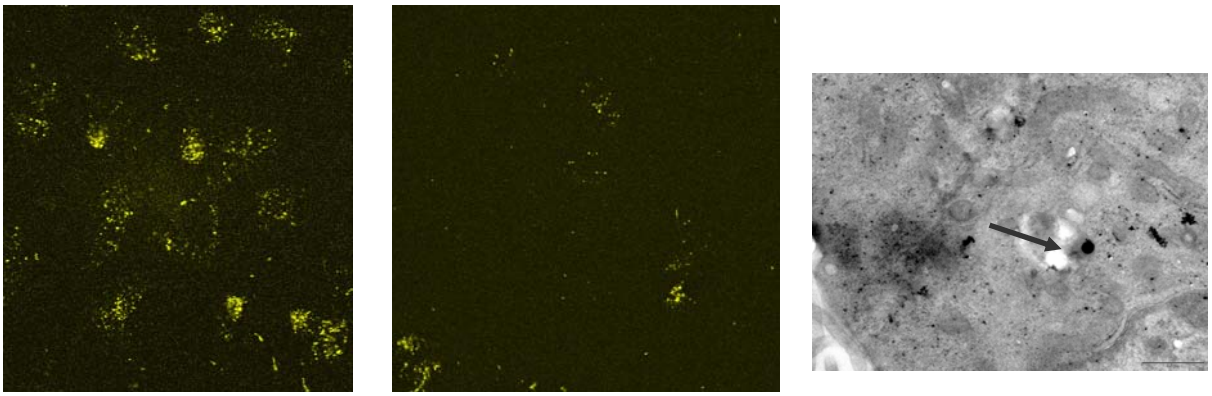

a b c

Fig. 2. Interaction between cells and gold nanorods: a) two-photon luminescence microscopy nanorods of gold coated with PEG-6000; b) two-photon luminescence microscopy of gold nanorods coated with PEG-40000; c) TEM of gold nanorods coated with PEG-6000

Finally, the influence of laser on viability of cancer cells was studied. The laser treated cells were incubated for 3 hours to ensure development of cellular response. It was found that the cells without nanoparticles didn't die after the laser treatment with the power up to 2 W. However, 65 and 70 % of the cells were killed after exposure at 2.5 and 3 W. The cells with nanoparticles were noted to die even at 0.5 W and reached a 90 % level at 3 W (fig. 3).

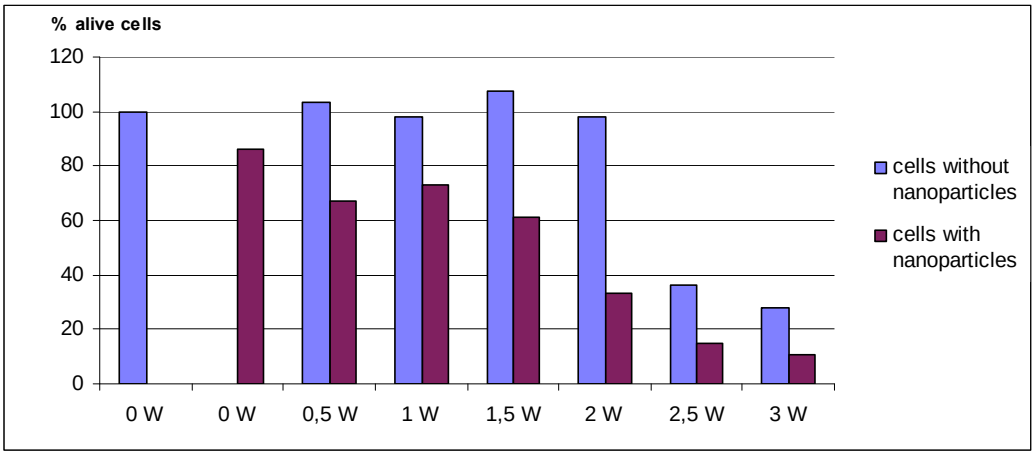

Fig. 3. Viability of cells after laser treatment

Thus, the gold nanorods penetration into the cells depends on coating materials. In addition, the gold nanorods have better light-heat conversion than the nanoshells. So, they may be used as nanothermosensitizers for cancer treatment.

Acknowledgements

This work was supported by the Russian Foundation for Basic Research (project No.~09-02 00539a) and the Ministry of Education and Science of the Russian Federation (projects Nos. 02.740.11.0713, 16.512.11.2053, 11.G.34.31.0017).

Invited

MEASUREMENTS OF LASER INDUCED TEMPERATURE FIELDS IN GOLD COLLOIDS USING LIGHT MICROSCOPY

I.V. Fedosov[1], **I.S. Nefedov**[2], **B.N. Khlebtsov**[3], and **V.V. Tuchin**[1]

[1] Dept of Optics & Biophotonics, Saratov State University, Russia, fedosov@optics.sgu.ru
[2] Helsinki University of Technology, Finland
[3]Institute of Biochemistry and Physiology of Plants and Microorganisms RAS, Saratov, Russia

Introduction

Light to heat conversion by noble metal nanoparticles has attracted the interest of many researches in connection with significant problems of nanophotonics including laser therapy, optical trapping and micromanipulation of nanoparticles [1–4]. Functionalized nanoparticles are employed to contrast a tumor in order to increase light absorption in malignant tissue. This enables killing cancer cells by means of topical hyperthermia induced with laser irradiation of the nanoparticles [1]. Obviously light-to-heat conversion enabled by metal nanoparticles plays a key role in the success of the procedure. On the other hand, laser induced heating is not desirable in optical trapping and manipulation of micro and nanoparticles with tightly focused laser beam [2]. The technique referred to optical tweezers is widely used in molecular biology and material science to measure piconewton forces applied to micrometer sized dielectric particles trapped with a laser beam. Optical trapping of metal nanoparticles is promising for different applications but it is still challenging because of strong heating of metal nanoparticles with laser radiation. Laser induced heating leads to thermal fluctuations breaking particle confinement [2].

The issues listed above require a detailed study of laser induced heating of individual nanoparticles immersed into liquid media. Although a number of theoretical considerations of the problem were published to date only a limited number of experimental studies were performed because of the lack of suitable methods and instrumentation [3, 4] Temperature estimation of a single nanoparticle is still challenging because conventional methods of nanoscale research like electron and scanning probe microscopy provide poor possibilities for observing nanoparticles immersed in liquid media and no way to measure their temperature. Alternatively, the use of light microscopy for the same purposes faces diffraction resolution limit, poor visibility and high diffusivity of nanoparticles in fluid. But in contrast to the electron microscopy, it allows studying nanoparticles dynamics in fluid media [5]. Earlier we reported the application of light microscopy for studies of laser induced flows in colloids and nanopartice diffusivity characterization [6]. In this paper we present results of experimental studies of laser induced heating of individual gold nanoparticles in a colloid solution.

Materials and methods

The goal of our study was to determine the temperature of gold nanoparticles immersed in water and irradiated with a focused laser beam. We used a PEG stabilized colloid solution of 40 nm gold nanoparticles in distilled water with a concentration of about 10^{11} particles/ml. The solution was placed inside a rectangular micro cell made of custom designed SPIM imaging system based on Carl Zeiss Axio Scope A1 microscope with W N-Achroplan 63×0.9 water immersion lens. The colloid solution was illuminated perpendicularly to the microscope lens axis with a 437 nm cw DPSS laser providing 60 mW output. The laser beam was focused on the microscope object plane into elliptical waist with 2×60 μm cross section. To acquire nanoparticle images Basler A602f non-intensified CMOS camera was attached to the microscope through additional optical system to provide 100 nm per pixel resolution. To analyze nanoparticle dynamics a statistical particle tracking velocimetry (SPTV)[5] based approach was implemented in the custom software developed using the National Instruments LabVIEW 8.5 Professional Development System [6]. The arrangement enables reconstructing the 2D field of ensemble averaged velocity of nanoparticles in colloids with spatial resolution of 1 μm and ensemble averaged field of particle temperature with the same resolution.

A 1 W 532 nm cw DPSS laser was used to heat nanoparticles. The laser beam was focused on the object plane of microscope in a circular waist of 11 nm in diameter at e^{-2} intensity level while it was counter propagating with one of 473 nm laser. Output power of 532 nm laser was measured with Newport Laser power meter. A short pass filter was introduced in the optical path of the microscope

order to block the intense radiation of 532 nm laser and let pass to camera 473 nm illuminator light only. Each measurement procedure included recording of a series of 5000 grayscale images of nanoparticles with resolution of 640×480 pixels. At chosen concentration of colloid typically several tens of particles appeared on each image. Then the whole series was processed to detect particle position. Finally, the resulting array of particle coordinates was analyzed with our SPTV software.

Results and summary

Typical results obtained with the arrangement described above are presented in fig. 1. While 532 nm was turned off no ordered motion of nanoparticles was observed (fig. 1(a), plot 1) and particle temperature was the same as the ambient one – 25 degree centigrade (fig. 1(b) plot 1). Plot (2) represents particle velocity (fig. 1(a)) and temperature (fig. 1(b)) in the case when 532 nm laser is turned on. Laser beam power in the plane of micro cell was 0.5 W that corresponds to 1.2 MW/cm^2 peak light flux of Gaussian beam with 11 μm waist diameter. Measured particle temperature at laser beam axis was 60°C. The result agrees with the theoretical consideration predicting surface temperature of 40°C for a single gold nanoparticle of 40 nm in diameter at incident light flux of 10^5 W/cm^2 at λ = 520 nm [4].

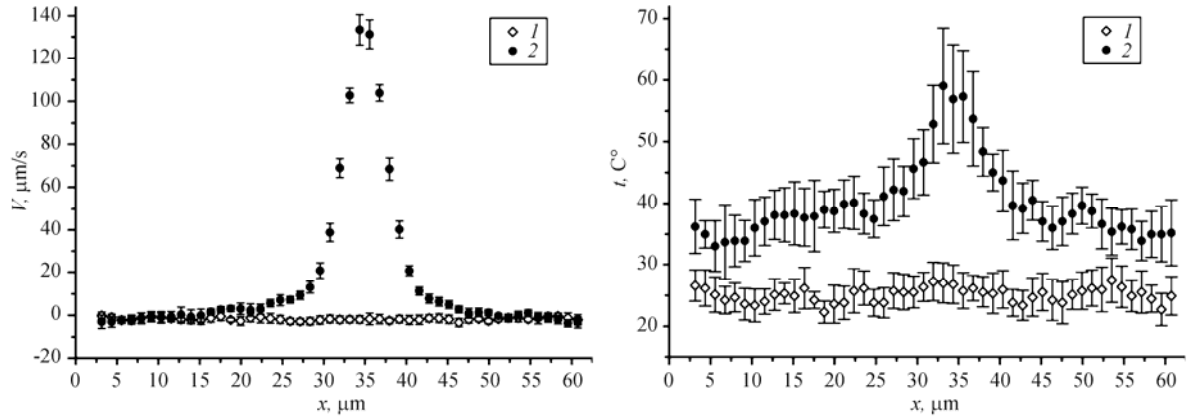

a) b)

Fig. 1. Distributions of velocity (z-component) (a) and temperature (b) in colloid solution when 532 nm laser is off (1) and then 532 nm laser provides 0.5 W in micro cell plane (2). Confidence level corresponds to p = 0.9

Acknowledgements

The work is supported by grant #224014 Network of Excellence for Biophotonics of the EU 7th Framework Programme; grants REC-006 and RUB1-2932-SR-08 of the US Civilian Research and Development Foundation for the IS of FSU; RF Government contracts 02.740.11.0484, 02.740.11.0770 and 02.740.0879.

References

1. J.R. Cole, N.A. Mirin, M.W. Knight *et al.*, *J. Phys. Chem. C,* 2009, **113**, 12090-12094.
2. C. Selhuber-Unkel, I. Zins, O. Schubert *et al.*, *Nano Lett.*, 2008, **8**(9), 2998-3003.
3. A.O. Govorov, W. Zhang, T. Skeini *et al.*, *Nanoscale Res. Lett.*, 2006, **1**, 84-90.
4. H.H. Richardson, M.T. Carlson, P.J. Tandler *et al., Nano Lett.*, 2009, **9**(3), 1139-1146.
5. J.S. Guasto, K.S. Breuer, *Exp. Fluids*, 2008, **45**, 157-166.
6. I.V. Fedosov, I.S. Nefedov, B.N. Khlebtsov, and V.V. Tuchin, *Opt. and Spectr.*, 2009, **107**(6), 846-852.

Invited

PLASMONIC NANOPARTICLES FOR BIOANALYTICS AND THERAPY AT THE LIMIT

A. Csaki, Th. Schneider, N. Jahr, J. Wirth, F. Garwe, O. Stranik, and **W. Fritzsche**

Institute of Photonic Technology (IPHT) Jena, Germany
fritzsche@ipht-jena.de

Noble metal nanoparticles show special optical properties with potential for labeling, sensing as well as manipulation at the nanoscale. Due to the established compatibility with the molecular world as documented in DNA- or protein-particle conjugates for microscopy labels or for DNA chip detection, these nanostructures will have a significant impact in nanobiotechnological applications [1].

Sensors based on localized surface plasmon resonance (LSPR)

Metal (especially gold) nanoparticles exhibit unique optical based on localized surface plasmon resonance as an interaction between light and the conduction electrons [2]. The resonance wavelength is influenced by material, size, and geometry of the particle, as well as by the properties of the immediate surrounding. This last dependence represents the base for sensoric applications: When the refractive index of the surrounding changes, the resonance wavelength will be changed, and the peak shift could be detected as sensoric signal. This effect can be observed both for particle ensembles – either in solution or as a surface coating (e.g. in glass fibers [3]) – as well as at the single particle level. For single particle studies, optical dark field mode is utilized that visualizes metal particles even of sub-wavelength dimensions due to their strong light scattering abilities. This technique, more than 100 years ago developed by Siedentopf and Zsigmondy, allowed then for the first time to see nanoparticles and represented thereby a breakthrough for nanosciences [4]. Using correlative microscopy of optical dark field as well as AFM, particles can be characterized and selected for spectral characterization by microspectroscopy. Thereby the light of only a small portion of the sample can be selectively collected and studied in a spectrometer coupled by a glass fiber. By collecting light from only a single particle, single particle experimenets can be conducted and the influence of the binding of (bio) molecules and the resulting spectral shift can be investigated at the single particle level.

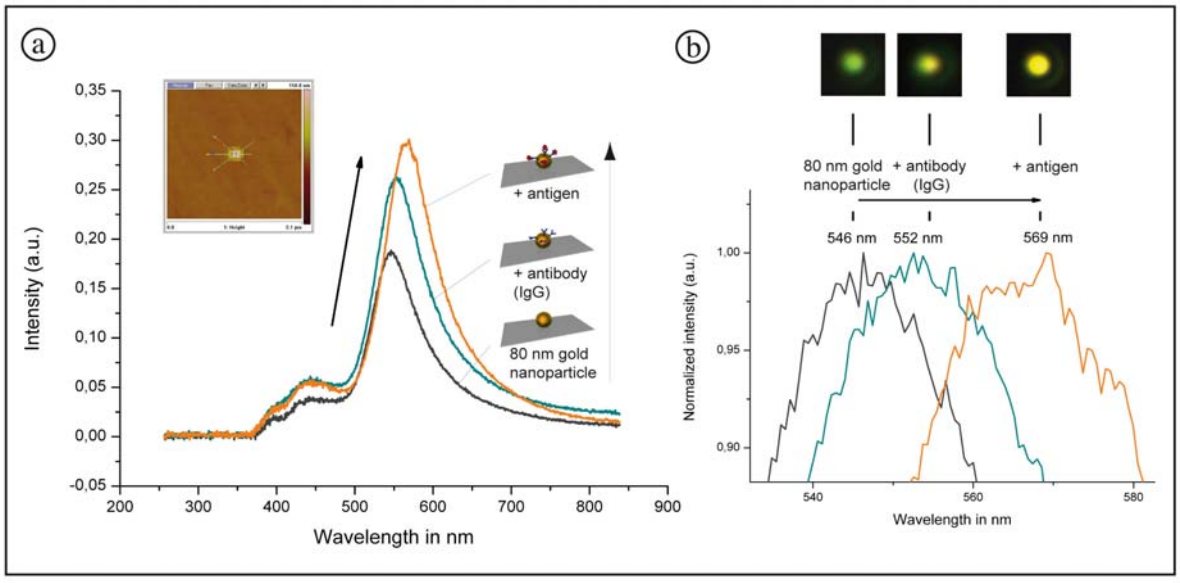

Single-particle biosensor: A 80 nm gold nanoparticle was covered with antibody prior to incubation with the respective antigen. Every step lead to a redshift of the localized surface plasmon resonance peak. a) overview b) Zoom showing the original noise level

Metal particles for sub-wavelength scale optical manipulation

Beside this sensoric part, plasmonic particles can also act in a more active way: When excited by fs pulsed laser light, particles can lead to damages highly localized at the size of their original diameter. So an optical manipulation at the nanoscale is possible. Utilizing this effect, we could demonstrate a sequence-specific manipulation at metaphase chromosomes [5] as well as DNA restriction [6]. Also we observed an unusual transport of the plasmonic excitation energy along DNA structure over several micrometers [7]. Two possible mechanisms to explain the transfer of energy from the particle to the DNA seem reasonable. We discuss these hypotheses.

Linear light excitation and resonant scattering effect on metallic nanoparticles with applications for analytical jobs as well as the nonlinear fs laser excitation and high energetic electrons in nanoparticles with applications in fields such as lithography, nanoplasmonics or molecular electronics are applicable at the nanoscale, thereby providing unique optical tools for technology and biology such as intracellular measurements and manipulations.

Acknowledgements

Funding for research initiative "MicroInter" (Beutenberg fellowship, TMWFK PE-113-1) and for research project "Multishell tuning of plasmonic core–shell nanoparticles" (DFG Fr1348/12-1) is gratefully acknowledged. We thank A. Ihring, K. Kandera, K. Pippardt, H. Porwol, M. Sossna, D. Horn, J. Albert, G. Schmidl, and U. Hübner for assistance with sample preparation and P.Wustelt for assistance with the laser experiments.

References

1. A. Csaki, T. Schneider, J. Wirth, N. Jahr, A. Steinbrück, O. Stranik, F. Garwe, R. Müller, & W. Fritzsche, "Molecular Plasmonics – light meets molecules at the nanoscale", *Philosophical Transactions A*, 2011, **369** (in press).
2. U. Kreibig & M. Vollmer, "Optical Properties of Metal Clusters", *Springer Series in Material Science* (Springer, Berlin, 1995).
3. A. Csaki et al., "Nanoparticle Layer Deposition for Plasmonic Tuning of Microstructured Optical Fibers", 2010, Small 6, 2584.
4. C. Sönnichsen & W. Fritzsche, "100 Years of Nanoscience with the Ulramicroscope – The work of Richard Zsigmondy" (Shaker, Aachen, 2007).
5. A. Csaki, F. Garwe, A. Steinbrück, G. Maubach, G. Festag, A. Weise, I. Riemann, K. König, & W. Fritzsche, "A Parallel Approach for Subwavelength Molecular Surgery Using Gene-Specific Positioned Metal Nanoparticles as Laser Light Antennas", *Nano Letters*, 2007, **7**, 247.
6. F. Garwe, U. Bauerschäfer, A. Csaki, A. Steinbrück, K. Ritter, A. Bochmann, G. Hüttmann, W. Paa, J. Popp, & W. Fritzsche, "Optically controlled thermal management on the nanometer length scale", *Nanotechnology*, 2008, **19**, 055207.
7. J. Wirth, F. Garwe, G. Hähnel, A. Csaki, N. Jahr, O. Stranik, W. Paa, & W. Fritzsche, "Plasmonic nanofabrication by long-range excitation transfer via DNA nanowire", *Nano Letters*, 2011, **11** (in press).

OPTICAL PROPERTIES OF COLLOIDAL SILICON NANOPARTICLES FOR APPLICATIONS IN BIOMEDICINE

M.B. Gongalsky, **A.Yu. Kharin, S.A. Korolev, L.A. Osminkina**, and **V.Yu. Timoshenko**

[1] M.V. Lomonosov Moscow State University, Faculty of Physics, E-mail: mgong@mail.ru

Applications of silicon nanocrystals (nc-Si) and other Si nanoparticles in biomedicine are motivated by biocompatibility and biodegradability of nc-Si [1]. Recently the biocompatibility of nc-Si has been also proved *in vivo* [2]. The biodegradability was measured in the number of papers and found to be dependent on average size of nanoparticles, their surface coverage chemistry and pH [1, 3]. The most explored applications are bioimaging, drug delivery [3], and photosensitization of the singlet oxygen generation [4]. Hydrogen passivated nc-Si particles, which are photosensitizers of the singlet oxygen generation, can be used in photodynamic therapy (PDT) of cancer [5]. Since Si nanoparticles with sizes less than 100 nm can penetrate into the living cells it should be taken into account for the applications both in diagnostics and therapy. It is known that the optical properties of nc-Si are drastically different from the bulk crystalline Si. For instance, the quantum confinement effect influences the optical and electronic properties of nc-Si with sizes less than 10 nm. Such small nc-Si can also exhibit efficient photoluminescence (PL) in the red and near infrared spectral range, which is attributed to the radiative recombination of excitons confined in nc-Si [4]. The exciton PL intensity at 1.2–1.8 eV could be rather efficient (quantum yield up to 10%) and it can be obviously used for bioimaging. Relatively long lifetimes (10–100 microseconds) of the PL are remarkable features of nc-Si, which ensure both convenience for luminescent diagnostics and favorable conditions for singlet oxygen photosensitization bun c-Si [5]. Indeed, the long-lived PL signals on nc-Si-related labels can be easily distinguished from fast fluorescence of biomolecules. In the present work we have investigated porous silicon (PSi) consisting of nc-Si with average diameter of 2–5 nm as a possible candidate for luminescent bioimaging and singlet oxygen photosensitization.

Samples of PSi were formed by a standard method of electrochemical etching of (100)-oriented c-Si wafers (p-type, boron doped to the specific resistance of 2...5 Ohm*cm) in a mixture of hydrofluoric acid (48%) and ethanol (1:1). The porosity of samples was about 80% and the average diameter of pores was 3-5 nm. Prior to the investigations, the PSi films were dried in air for one day and then mechanically grinded (milled) to get powders of nc-Si.

The singlet oxygen generation in PSi in oxygen ambient is spectrally detected by the PL measurements at 0.98 eV or 1270 nm (see Fig. 1), which is a fingerprint of singlet oxygen molecule [6]. We found that the intensity of this line exhibited an effect of the photobleaching. Indeed, the luminescence intensity decreases continuously during the laser irradiation (see Fig. 2). This effect can be caused by the interaction of singlet oxygen molecules with nc-Si. The dependence of the luminescence intensity on illumination time follows a power law, which is typical of disordered systems such as PSi. We suggest that this phenomenon could be controlled by porosity of PSi, which influences mean distances between nc-Si.

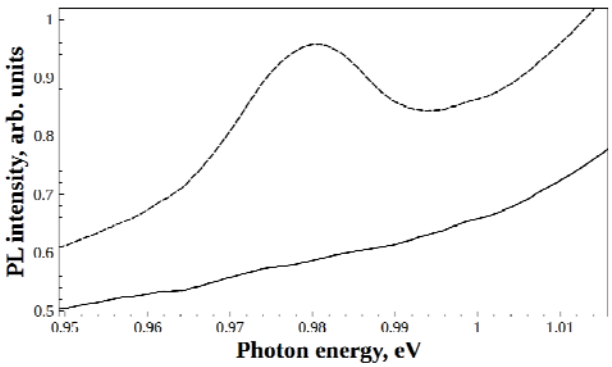

Fig. 1. Intensity of the PL of PSi powder in vacuum (solid line) and in oxygen ambient (dashed line). Peak at 0.98 eV corresponds to the photosensitized singlet oxygen luminescence. Laser irradiation at 2.33 eV. Temperature 300 K

PSi samples were also investigated in aqueous suspensions. In suspensions Si nanoparticles seem to be agglomerated with average diameter of the grains of about 200 nm according to dynamic light scattering data. The photobleaching was observed in both powders and suspensions and the Pl degradation effect correlated with the presence of oxygen molecules. In water it was decreased after bubbling with nitrogen and increased after bubbling with oxygen.

The intrinsic exciton PL at 1.2–1.8 eV of PSi was found to be stable under laser irradiation in vacuum. The singlet oxygen generation was accompanied with the photobleaching of the exciton PL (Fig. 2). This effect can be explained by defect formation due to photoinduced oxidation of nc-Si surface. The latter is probably reduced because of the photobleaching of the singlet oxygen generation (compare the curves in Fig. 2).

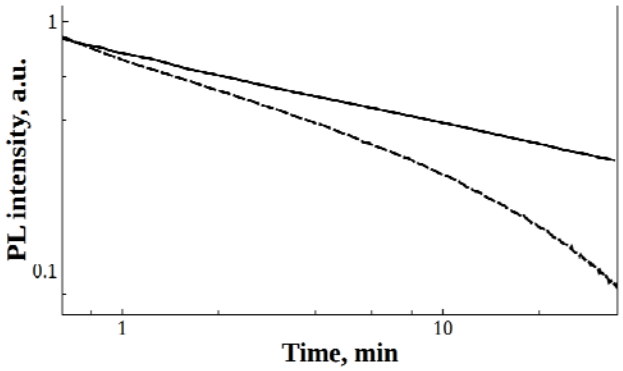

Fig. 2. PL intensity of nc-Si at 1.6 eV (solid line) and luminescence of photosensitized singlet oxygen (dashed line) *vs* time of laser irradiation at 2.33 eV. Temperature 300 K

In conclusion, PSi formed by electrochemical etching of c-Si demonstrates the PL properties, which are dependent on the molecular ambient and illumination time. The singlet oxygen generation by nc-Si in PSi powder and suspension can be deactivated after several hours of laser radiation. This effect should be considered for possible applications in PDT. Along with some limitations this points to the advantage of such photosensitizers: the patient should not avoid ambient light after procedure. As for the bioimaging applications nc-Si in PSi samples should be probably well oxidized or protectively covered by any shell (e.g., polymer, silicon carbide, etc.) in order to suppress oxygen-induced photodegradation. Since such coverage can significantly decrease the efficiency of singlet oxygen generation, a special attempt has to be made to improve the photosensitizing properties of nc-Si. This could be probably realized by further grinding of PSi or by using other methods of nc-Si formation (e.g., laser ablation, plasma-enhanced chemical vapor deposition, etc.).

Acknowledgment

This work has been performed using the equipment of the Center of User's Facilities of MSU.

References

1. L.T. Canham, *Nanotechnology*, 2007, **18**, 185704.
2. A.D. Durnev et al., *Int. J. Biomed. Nanosci. & Nanotech.*, 2011, **1**, 70.
3. J. Park et al., *Nature Materials*, 2009, **8**, 331.
4. E. Gross, et al., *Phys. Rev. B*, 2003, **68**, 115405.
5. V.Yu. Timoshenko et al., *JETP Lett.*, 2006, **83**, 423.
6. A.A. Krasnovsky Jr., *Chem. Phys. Lett.*, 1981, **81**, 443.

STUDYING THE SPECIFIC PROTEIN-PROTEIN INTERACTIONS BETWEEN UBIQUITIN SYSTEM COMPONENTS

E.L. Guryev[1], **A.S. Zhabereva**[1], **E.V. Kondratieva**[1], **A.L. Chernorudskiy**[1,2], **A.S. Ivanov**[3], **Yu.V. Mezentsev**[3], **V.G. Zgoda**[3], **A.T. Kopylov**[3], and **M.R. Gainullin**[1,4]

[1]Institute of Applied and Fundamental Medicine, Nizhny Novgorod Medical Academy, 603005 Nizhny Novgorod, Russia, ksonm@rambler.ru
[2]IFOM, the FIRC Institute for Molecular Oncology Foundation, 20139 Milan, Italy
[3]Institute of Biomedical Chemistry of the Russian Academy of Medical Sciences, 119121 Moscow, Russia
[4]Biomedical Institute for Research in Light and Image, University of Coimbra, 3000-548 Coimbra, Portugal

Introduction

A hetero-dimeric complex consisting of ubiquitin-conjugating enzyme UBE2N and adaptor protein UEV1A catalyzes formation of multiubiquitin chains polymerized via K63. This type of multiubiquitylation does not lead to protein degradation by the 26S proteasome, but mostly plays a role in the error-free DNA repair pathway and contributes to the cell survival after DNA damage. Also, UBE2N-UEV1A acts together with the ubiquitin-protein ligases HLTF and SHPRH in the K63-linked multiubiquitylation of PCNA upon genotoxic stress, which is required for DNA repair. It was recently shown, that UBE2N is able to recruit many other ubiquitin-protein ligases, however these pathways are not well characterised yet. In the absence of UEV1A, ubiquitin moieties are transferred to UBE2N´s own lysine residue. The mechanism and physiological role of UBE2N autoubiquitylation is not well studied. In this survey we investigated specific interactions between ubiquitin system components using a surface plasmon resonance (SPR) technique.

Materials and methods

Ubiquitylation reaction in vitro contained 5 μM UBE2N, 0.1 μM E1, 10 mM ATP, 10 mM dithiothreitol, 10 mM $MgCl_2$, 50 mM NaCl, 25 mM TrisHCl (pH 7.5) and ubiquitin in concentration 0.5 mg/ml. The mixture was incubated at 30^o C for 4 hours and then chilled to 0^o C.

For real-time monitoring of protein-protein interactions we used an automatic optical biosensor Biacore 3000. Immobilization of UEV1A protein on CM5 chip carboxymethyldextran surface was carried out in acetate buffer (pH 4.5) with N-hydroxysuccinimide и 1-ethyl-3-(3-dimethylaminopropyl) carbodiimide hydrochloride. Residual active ether groups were inactivated with ethanolamine. Analytes were dissolved in buffer containing 10 mM HEPES (pH 7.4), 150 mM NaCl, 3 mM EDTA and 0.005% P20 surfactant. Products of in vitro ubiquitylation reaction, dissolved in reaction buffer, were directly injected to the biosensor. The flow rate was 5 μl/min. The system was cleaned before and after the injection of each analyte.

Data analysis and sensogram plotting were performed with GraphPad Prism 5 program.

Results and discussion

We investigated protein-protein interactions between ubiquitin-conjugating enzyme UBE2N, adaptor protein UEV1A and ubiquitin. Recombinant protein UEV1A was covalently immobilized on CM5 chip surface and used as ligand. Signal level of immobilized UEV1A protein was from 1700 to 3700 RU. A non-specific binding signal about 480-500 RU was revealed in the control channels of biosensor (inactivated dextran).

UEV1A protein consists an ubiquitin-binding domain (UEV), which plays role in K63-polymerased multiubiquitin chains formation. We probed binding ability of this domain to the free monomer ubiquitin and find it extremely low. There was no significant binding level when ubiquitin in concentration 300 μg/ml (35 μM) was injected in CM5 chip. Low affinity of UEV domain to ubiquitin is supposed. Also, non-optimal orientation of UEV domain on the chip surface and restricted steric accessibility of protein-protein interaction area may affect binding efficiency.

The interaction between different concentrations of unmodified recombinant UBE2N and immobilized UEV1A was studied (Fig. 1.A). We used the following concentrations of recombinant unmodified UBE2N in analytes: 10 μg/ml, 20 μg/ml, 50 μg/ml and 100 μg/ml. The results show that the signal proportionally grows from 10 mkg/ml to 100 mkg/ml. Based on this data, we calculated the

kinetic parameters for UBE2N/UEV1A complex forming (Fig. 1.B). It must be emphasized that the affinity of UEV1A to UBE2N was higher by 4 orders than to ubiquitin.

Protein-protein interactions between adapter protein UEV1A, immobilized on CM5 chip surface, and autoubiquitylated form as well as unmodified form of UBE2N were studied. After providing in vitro ubiquitilation, UBE2N modification was confirmed by immunoblotting with anti-UBE2N and anti-ubiquitin antibodies. Uev1a displays a slightly higher ability to bind autoubiquitylated UBE2N, if compared with unmodified protein (Fig. 2).

A

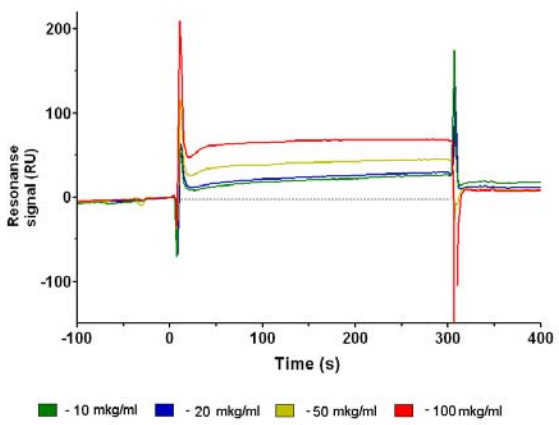

B

K_D, 10^{-8}M	K_A, $10^7 M^{-1}$	k_{on}, $M^{-1}s^{-1}$	k_{off}, $10^{-6}s^{-1}$	x^2
2.6±0.4	3.9±0.6	83±5	2.1±0.2	0.6

Fig. 1. A. Overlay plot of sensorgrams showing interaction between different concentrations of unmodified recombinant UBE2N and immobilized UEV1A. "0" piont – time of samples injection. Resulting sensograms – difference between signal intensivities in 2 channels of biosensor: 1) inactivated dextran (control); 2) covalently immobilized UEV1A (sample). B. Kinetic parameters for UBE2N/UEV1A complex forming

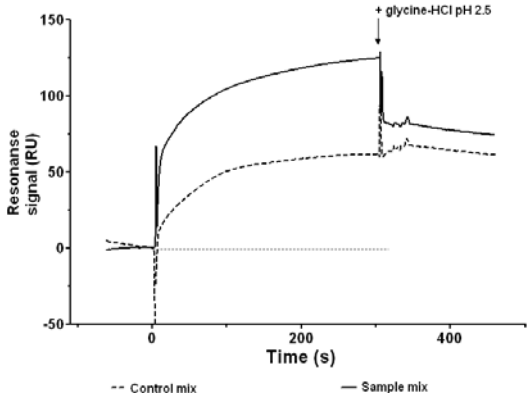

Fig. 2. Overlay plot of sensorgrams showing interaction between auto-ubiquitylated and unmodified form of UBE2N with immobilazed UEV1A.
"0" piont – time of samples injection; Sample – ubiquitilation reaction mix; Control – ubiquitilation reaction mix without ATP. Resulting sensograms – difference between signal intensivities in 2 channels of biosensor: 1) inactivated dextran (control); 2) covalently immobilized UEV1A (sample)

The observed effect can be explained by a synergism of the UEV1A-UBE2N and UEV1A-ubiquitin interactions. Also, interactions of UEV domain with UBE2N-ubiquitin complex may be more efficient than with free monomer ubiquitin. We suggest that covalently immobilized ubiquitim molecule is more precisely positioned relative to protein-protein interaction area of the ubiquitin-binding domain. Previously K92 was identified as predominant UBE2N autoubiquitylation site. Based on our findings, suppose that K92 mono-ubiquitylation is a specific recognition signal for ubiquitin-binding domain containing proteins. Additionally, the modified form of UBE2N (Ubc13) was identified as by-product, formed under the action of the whole set of ubiquitylating enzymes. Together, these data help to refine mechanisms of UBE2N-mediated ubiquitylation and shed light on the functional role of its autoubiquitylation.

Acknowledgements

This work was supported by Russian Foundation for Basic Research grants 08-04-01816 and 08-04-97107.

References

1. A. Al-Hakim, C. Escribano-Diaz, M.C. Landry, L. O'Donnell, S. Panier, R.K. Szilard, D. Durocher, *DNA Repair(Amst)*, 2010, **9**(12), 1229-1240.
2. Y. David, T. Ziv, A. Admon, A. Navon, *The journal of biological chemistry*, 2010, **285**(12), 8595-8604.
3. D. Hoeller, C.M. Hecker, S. Wagner, V. Rogov, V. Dotsch, I. Dikic, *Mol. Cell.*, 2007, **26**(6), 891-898.

DNA DELIVERY AND GENE EXPRESSION BY GOLD NANORODS EXCITED BY FEMTOSECOND LASER

Hao He[1*], **K.T. Chan**[2], **Y.F. Li**[1], **M.L. Hu**[1], and **C.Y. Wang**[1]

[1] Ultrafast Laser Laboratory, College of Precision Instrument and Optoelectronics Engineering
Tianjin Univerisity, Tianjin, P.R. China
*Email: hhe@ee.cuhk.edu.hk
[2]Department of Electronic Engineering, the Chinese University of Hong Kong, Hong Kong

Transfection is a key technique in cell and molecular biology with many important biochemical applications. Optical transfection by Ti: Sapphire femtosecond (fs) lasers developed in 2002 [1] have been expected a high-efficiency and clean approach. However, the focused laser beam could transfect only a single cell in one time limiting its practical applications. Recently, a breakthrough has been made by combining microfluidic system with fs lasers for high throughput photoporation [2], which is potentially able to deal with thousands of cells in one hour. But the setup is complicated and the amount of cells in one experimental run is still much smaller than traditional biological method.

Nano-particles as novel probes and carriers in biological science have attracted great interest from worldwide researchers. Gold nanorods (GNRs) can diffuse into cells freely with little toxic and have responses to single and multi- photons at visible and near infrared (NIR) bands [3, 4]. GNRs have been used as carrier to deliver RNA for H1N1 influenza therapy by complicatedly connecting GNRs with RNA molecules to form nano-plex [5]. To be simple, it was reported DNA molecules could be firstly added with –SH, connect with GNRs by Au-S bond, and form DNA-GNR conjunctions [6]. The DNA plasmids were then delivered into cells by the free diffusion of GNRs. Finally, DNA molecules would be released from melted and deformed GNRs by fs laser heating. This method needs long-time optical exposure (>1 min) by high-energy fs pulses to melt the GNRs, and if the laser power is high enough, milliliters of cell solution containing hundreds of thousands cells can be treated in one time. But such illumination would harm cells a lot and photo-break the DNA molecules, causing very low transfection efficiency (< 20%). Here we connected GNRs with green fluorescence protein (GFP) DNA plasmid simply by static electrical charge. The GNRs delivered the DNA molecules into HeLa cells and were then illuminated by fs lasers to release DNA. GFP expressions were observed 36 hours after the exposure and the transfection efficiency was 18%.

1. Materials Preparation

Bare GNRs (Nanopartz) with the scattering peak at 930 nm (0.2 pM, 20 μL) were mixed with GFP DNA plasmid solution (10 μg/mL, 0.3 mL) by shacking at vortex shakers for 2 minutes and then incubated at 4°C for 10 minutes. Since DNA molecules are naturally negatively charged, they will connect by the electrical force to form DNA-GNR conjunctions. The rate and efficiency of this connecting need to be further studied. The mixture was then centrifuged to remove excess GNRs. HeLa cells were prepared at a concentration 2×10^5 /mL at RPMI1640 medium (Sigma). For microscopic studies, cells were seeded on a 35 mm culture petri dish with a glass slide (0.17 mm thick) at the bottom (MatTek), 1 mL cell solution for each petri dish.

2. Diffusion and Distribution of GNRs in Cells

The GNRs have a scattering peak at 930 nm and a secondary peak at 510 nm due to different modes of the surface plasma resonance (SPR) as shown in Fig. 1(a). They would emit red light (fluorescence) when excited by white light or laser beam at 488 nm as Fig. 1 (b) and (c). To study the diffusion and distribution of GNRs in cells, the solution of GNR-DNA conjunctions were added into the cell dish and incubated for 30 min at 37°C, and then scanned by a confocal microscope (Nikon C1). If the cells were suspending in medium, clusters of GNRs were found in cell membrane with very regular distribution (Fig. 1(d)). If the cells have been already adherent and flatten onto the glass, GNR clusters were also found in the membrane by total intra reflection fluorescence (TIRF) imaging as shown in Fig. 1 (e). However, those clusters were not observed in all cells and it can be found in Fig. 1(f) that GNRs would exist in a uniform manner inside the cytoplasm.

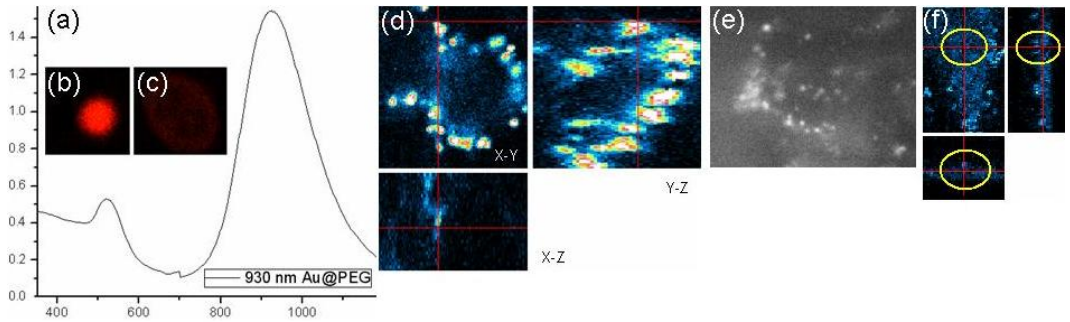

Fig. 1. GNRs in Cells. (a) the scattering spectrum of the GNRs. Red fluorescence of GNRs when illuminated by white light (b) and beam at 488 nm (c). (d) Confocal scanning of GNRs clusters in membrane of suspending cells. (e) TIRF imaging of GNRs clusters in membrane of adherent cells. (f) GNRs inside cytoplasm

3. DNA Release Excited by Femtosecond Laser and GFP Expression

Homemade Yb-doped fiber fs laser has a central wavelength at 1041 nm, with the pulse width 200 fs, repetition rate 9 MHz, and mean power 300 mW. The laser beam was expanded to a diameter of 10 mm to expose cells. The power density was only around 0.1 W/cm^2, compared with 10^8 W/cm^2 for photoporation. The solution of GNR-DNA conjunctions was added into the cell dish and then incubated for 2 hours. The expanded fs laser beam irradiated the mixed cell solution for 1 s (10 mm area), and around 2×10^4 cells were treated in total, which were then cultured for 36 hours. GFP expression was observed as shown in Fig. 2, and the transfection efficiency was around 18%. There was no GFP expression when the laser power was decreased to 150 mW. However, the transfection efficiency did not change when the power density increased to 1.6 W/cm^2, either when the exposure time up to 5 s. Probably the transfection efficiency was limited by two factors: 1) the excitation efficiency by the laser at 1040 nm, and 2) the connecting efficiency of DNA molecules with GNRs.

Control experiments were performed to confirm the role of fs laser excitation. A group of cells incubated with the GNR-DNA conjunctions at the same conditions without any laser treatment did not show any GFP expression, which means the DNA molecules can not release themselves in this case. Another group of cells was at first incubated with DNA solutions at the same concentration without any GNRs, irradiated at the same power density for 1 s. No GFP fluorescence was observed either, indicating the chance of DNA molecules diffusing into cells during the photoporation by the fs beam is very little at such low DNA concentration.

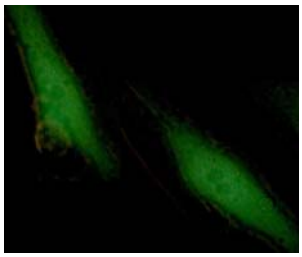

Fig. 2. GFP expression in HeLa cells 36 hours after laser treatment

4. Conclusion

Here we demonstrated a novel transfection method with DNA molecules delivered by GNRs. The genes could be released from GNRs excited by fs beams, and GFP expressions were observed at an efficiency of 18%. Thousands of cells were transfected in 1 s. The efficiency may be improved by changing a shorter wavelength which is close to the scattering peak of GNRs to induce higher SPR. The laser power density can be only 10^{-9} times of photoporation. This novel transfection method thus has great potential for large-amount cell engineering.

References

1. U.K. Tirlapur and K. Konig, *Nature*, 2002, **418**, 290-291.
2. R.F. Marchington, et al., *Biomedical Optics*, CLEO/QELS, Miami, Florida 2010, BTuD92.
3. H. Wang, et al., *Prod. Nat. Acd. Sci. USA*, 2005, **102**, 15752-15756.
4. O. Schwartz and D. Oron, *Nano Letters*, 2009, **9**, 4093-4097.
5. K.V. Chakravarthy, et al., *Prod. Nat. Acd. Sci. USA*, 2010, **107**, 10172–10177.
6. C.C. Chen, et al., J. AM. CHEM. SOC. 2006, **128**, 3709-3715.

Invited

IMAGING THE *IN VIVO* CELL BIOLOGY OF CANCER

R.M. Hoffman

AntiCancer Inc., San Diego, California, USA, email: all@anticancer.com
Dept. of Surgery, University of California, San Diego, California, USA

In order to visualize single cancer cell nuclear dynamics in the brain, U87 human glioma cells were injected into the brain stereotactically, or Lewis lung mouse carcinoma (LLC) cells were injected into the carotid artery of nude mice. Both cancer cells types express GFP in the nucleus and RFP in the cytoplasm. A craniotomy open window was made over the right parietal bone for real-time imaging of cancer cells on the brain. Mitotic and apoptotic cancer cells in the brain were imaged in real time. Temozolomide (TMZ) and UVC light were used for induction of cancer cell apoptosis. Imaging showed that approximately 86% of Lewis lung carcinoma cells irradiated with UVC light underwent apoptosis and died in contrast to U87 cells which were resistant to UVC. Real-time subcellular imaging in the brain showed TMZ-induced apoptosis of both U87 and LLC cells. Imaging could be carried out for at least two weeks through the craniotomy window enabling treatment to be evaluated on cancer cells in the brain at the subcellular level. The subcellular real-time imaging model of cancer cells in the brain will be of important use for discovery and evaluation of novel drugs active against brain cancer and brain metastasis.

Materials and Methods

Craniotomy open window. The scalp was retracted and the skull was exposed. Using a skin biopsy punch, a 4 mm diameter craniotomy was made over the right parietal bone (Fig. 1-a,b). The bone fragment was removed carefully in order not to injure the meninges and brain tissue. The craniotomy open window was covered only by the scalp. Thus, only scalp retraction was needed in order to image single cancer cells in the brain. The incision was then closed with 6-0 surgical sutures.

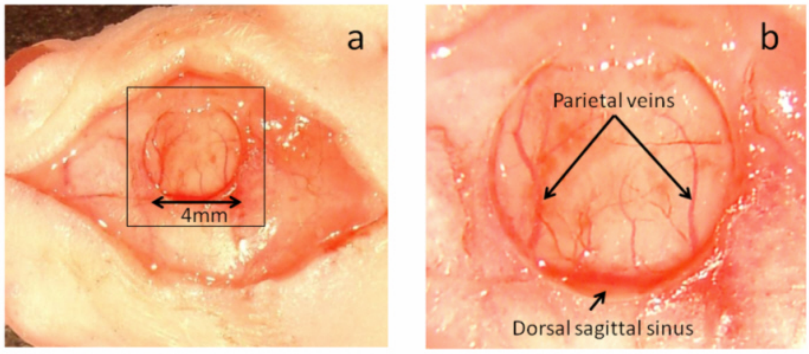

Fig. 1. The craniotomy open window.
(a) Using a skin biopsy punch, a 4 mm diameter craniotomy was made over the right parietal bone
(b) The brain tissue and veins were observed through the craniotomy open window

Stereotactic injection of cancer cells in the brain. After the craniotomy open window was made, 1 µl containing 1×10^5 dual-color U87 cells was injected stereotactically into the mouse brain using a 10 µl Hamilton syringe. Cells were injected in the middle of the craniotomy open window to a depth of 0.5 mm.

Internal carotid artery injection of cancer cells. An incision was made in the skin at the center of the neck. The artery was exposed by blunt dissection from the common carotid artery at the point of division into the internal and external carotid arteries. After the external artery was clamped, dual-color LLC cells (1×10^6 cells in 20 µl) were slowly injected with a 31-gauge needle into the right internal carotid artery. The skin was closed with a 5-0 surgical suture.

Fluorescence imaging of dual color cancer cells in the brain. The brain was observed repeatedly through the craniotomy open window to observe behavior of the cancer cells. All fluorescence images were obtained with the Olympus OV100 Small Animal Imaging System.

Chemotherapy of cancer cells in the brain. Seven days after tumor-cell inoculation, mice were treated daily with TMZ (100 mg/kg, i.p.) for 5 days. TMZ was dissolved in 30% dimethyl sulphoxide and 70% normal saline.

UVC treatment of cancer cells in the brain. The brain was irradiated with an 11.0-watt hand-held UVC light source (265 nm) (UVP LLC, Upland, CA) seven days after cancer cell inoculation. Irradiation was through the craniotomy open window for 60 seconds. The cells were observed during the following 24 hours through the open window. Five mice were used in this experiment. The experimental data are expressed as the mean ± SEM. Statistical analysis was performed using the Student's *t*-test.

Results and Discussion

Single cancer cells (U87 and LLC) in the brain were observed through a craniotomy open window (Fig. 2) in live mice using the OV100 Small Animal Imaging System. Colonies of both cell types were observed as well (Fig. 2). GFP-expressing nuclei and RFP-expressing cytoplasm could be observed in single cancer cells. Therefore mitosis and apoptotic changes of the cancer cells could be distinguished easily and clearly. Figure 3 shows time course imaging of a dual-color LLC cell undergoing mitosis in the brain. TMZ and UV-C light induced apoptosis in dual-color LLC cells in the brain as observed in live mice. Aggregation of chromatin at the nuclear membrane, fragmented nuclei and destruction of cytoplasm of the cancer cell were followed in real time in the brain.

The brain was irradiated for 60 seconds with UVC light through the craniotomy open window. Twenty four hours after UVC light irradiation, the number of LLC cells in the brain decreased significantly. Approximately 86% of LLC cells irradiated with UVC light died and disappeared. In contrast, the number of U87 cells in the brain was not significantly different before and after UVC irradiation. No hemorrhage was observed and the blood vessels were not destroyed after irradiation.

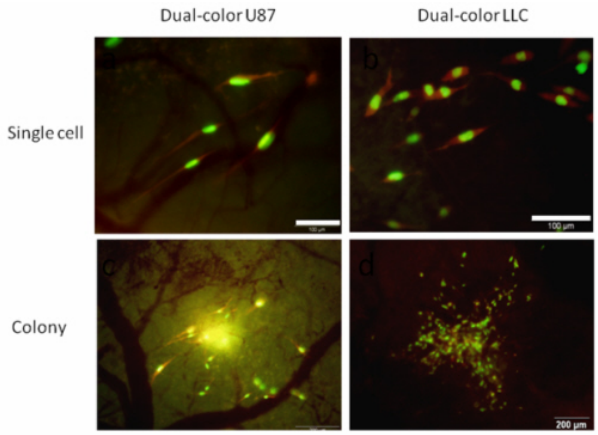

Fig. 2. Dual-color U87 and LLC cells in the brain through the craniotomy open window in live mice. (a, b) Dual-color *87 and LLC cells with GFP-expressing nuclei and RFP-expressing cytoplasm. (c, d) Colonies of dual-color cancer cells in the brain

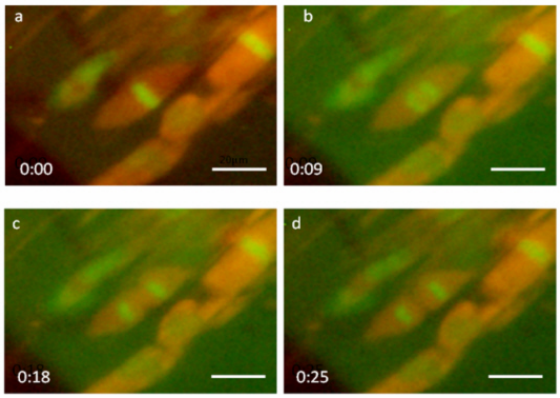

Fig. 3. Real-time imaging of mitosis of dual-color cancer cells in the brain. (a–d) Visualization of time course of mitosis in the brain of live mouse. Images were captured from the same LLC cell at various phases of mitosis:
a, Metaphase; b, Anaphase;
c, Telophase; d. Cytokinesis

Conclusions

We have developed a novel mouse brain imaging model in which cancer cells in the brain could be observed at the subcellular level in live mice. The dual-color cancer cells, craniotomy open window and Olympus OV100 imaging system used in the present study enable longitudinal, real-time, subcellular nuclear-cytoplasmic dynamic imaging of cancer cells in the brain. With this imaging technology, we were able to observe nuclear and cytoplasmic dynamics during mitosis and apoptosis of cancer cells in the brain. This model can be used to evaluate new treatment modalities of brain metastasis or brain cancer at the subcellular level.

References

1. R.M. Hoffman, *Nature Reviews Cancer*, 2005, **5**, 796-806.
2. R.M. Hoffman and M. Yang, *Nature Protocols*, 2006, **1**, 775-782.
3. H. Kimura, et al., *J. Cell. Biochem.*, 2010, **110**, 1439-1446.

Invited

ELECTRONIC STRUCTURE COLOR-TUNING AND REDOX PROPERTIES OF FLUORESCENT InP CORE/SHELL QUANTUM DOTS FOR BIOIMAGING

J.A. Hollingsworth[1,§], **A.M. Dennis**[1], **Y. Ghosh**[1], **A. Piryatinski**[1], **B.D. Mangum**[2], and **H. Htoon**[2]

[1] Materials Physics & Applications: Center for Integrated Nanotechnologies, Los Alamos National Laboratory (LANL), Los Alamos, NM, USA [§]jenn@lanl.gov

[2] Chemistry: Physical Chemistry and Applied Spectroscopy, LANL, Los Alamos, NM, USA

Due to their characteristic bright and stable photoluminescence (PL), semiconductor nanocrystal quantum dots (NQDs) have attracted much interest as efficient fluorophores. Their numerous enabling traits notwithstanding, NQDs are frustratingly sensitive to the chemical environment, "blink", and are susceptible to efficient Auger recombination, a nonradiative decay process. We recently reported a new class of core/shell NQD that we called "giant" NQDs due to their relatively thick inorganic shell. We demonstrated unprecedented non-blinking and non-photobleaching behavior, suppressed Auger recombination, and superior aqueous-phase stability toward applications in single-particle tracking and bioimaging [1–3]. These initial developments were achieved using CdSe-based NQDs. More to date, we have extended the "giant-NQD" structural motif to InP-based core/shell systems in an attempt to realize the useful and novel photophysical and chemical characteristics afforded by this new functional class of NQD fluorophore in a compositionally disparate system. We have explored four InP-based systems: InP/ZnS, InP/ZnSe, InP/CdS, and InP/CdSe. We have shown that by changing shell material we can effect significant color tuning of the emission energy from the green-visible to the near infrared (to 1250 nm), resulting from modifications to the core/shell electronic structure. Given the brevity of this report, we focus our discussions on the InP/CdS system as a representative example of our results in the context of thick-shell InP NQDs. These NQDs were synthesized by modifying a literature preparation for InP cores [4] as well as our procedure for growth of CdSe/CdS giant NQDs [2].

Electronic structure manipulation by NQD core/shell engineering

Core/shell NQDs can be classified as type-I or type-II depending on the relative alignment of conduction- and valence-band energies of the core and shell materials. Type-I electronic structures result when both the conduction and the valence band edges of one of the materials are located within the energy gap of the other material. Excitation of an electron-hole (*e-h*) pair results in localization of both carriers in the smaller gap material, as it affords the lowest energy states for both electrons and holes. In contrast, type-II core/shell systems are characterized by significant spatial separation of the e-h pair, as the lowest energy states for these carriers are in different semiconductors. A third general type of NQD core/shell electronic structure is the so-called quasi-type II relationship, where one carrier is confined to either the core or the shell and the other is delocalized over the entire NQD, resulting in partial spatial separation of the *e-h* pair. The precise electronic structure achieved for any given core/shell system is a function of the bulk material properties, the effects of quantum confinement on the core bandgap and conduction/valence band energy offsets, and the thickness of the shell.

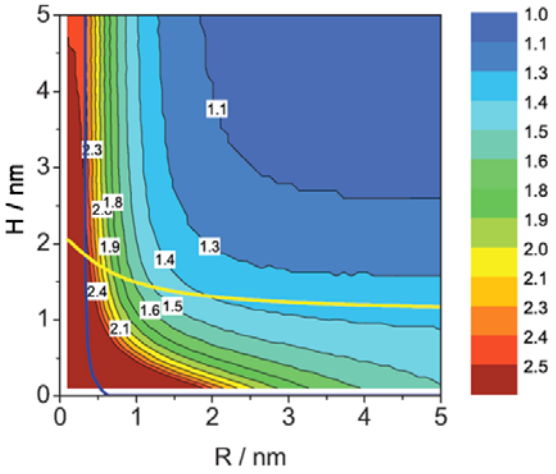

Fig. 1. Contour plots of bandgap energy (eV) calculated for InP/CdS core/shell NQDs as a function of InP core radius (*R*) and CdS shell thickness (*H*). For *R* values greater than ~1 nm, shell thicknesses below the yellow line are predicted to afford quasi-type II behavior (partial *e-h* spatial separation), while thicker shells are predicted to generate type-II structures (complete *e-h* spatial separation)

In the InP-based core/shell series comprising shells of ZnS, ZnSe, CdS, or CdSe, all three electronic structures are theoretically feasible. The Zn-containing shell systems should afford transitions between quasi-type II and type-I, while Cd-containing shell systems should give predominantly quasi-type II and type II structures, as well as type I assuming full tunability of core size and shell thickness. As an example, we show in Figure 1 the theoretically modeled bandgaps for the InP/CdS core/shell NQD system as a

function of core size and shell thickness, calculated according to methods developed previously by members of our team for other core/shell NQD systems [5].

Emission-color and lifetime tuning in InP-based core/shell NQDs

The tendency in the case of the Zn-based shell systems for either no (type I) or less (quasi-type II) charge separation results in our experimental observation that emission energies for these systems are in the visible and fully reflective of emission from a size- or quantum-confined InP core. In contrast, we readily achieve infrared emission from core/shell systems comprising Cd-containing shells that is smaller in energy than the InP core bandgap. This emission is reflective of a charge-separated *e-h* pair, that is, radiative recombination across a "spatially indirect" gap. In this way, compositional and thickness tuning of the shell in the InP-based core/shell systems affords dramatic emission color tunability, and, specifically, in the case of the InP/CdS system, swift transition from green-visible PL to infrared PL is achieved (Fig. 2a). Here, we show absorption and PL spectra for core-only InP NQDs, as well as core/shell systems comprising 1, 4, or 10 monolayers of CdS shell material. We reveal that even relatively thin-shell systems afford a transition from a fully localized electronic structure to one characterized by significant spatial separation of the excited-state e-h pair. This is evident in the shell-thickness-dependent PL spectra as large spectral shifting to lower energies as shells are added. Addition of one CdS monolayer yields PL at 676 nm, which is ~100 nm red of the InP core bandgap. Subsequent shells shift the PL to close to 1000 nm. We also obtained PL lifetimes for the core/shell systems and found them to be long compared to literature values for core-only InP NQDs, indicative of core/shell PL from charge-separated states. Specifically, we found average room-temperature lifetimes for the 1, 4, and 10-shell systems to be 499 ns, 686 ns, and 806 ns, respectively. In contrast, lifetimes for core-only InP NQDs have been reported to be in the range of 28–73 ns at 298 K [6]. Structural characterization by transmission electron microscopy (TEM) confirms the large total NQD size achieved when 10 monolayers of shell are grown onto the starting InP core, reflective of the uniquely thick CdS shell (Fig. 2b).

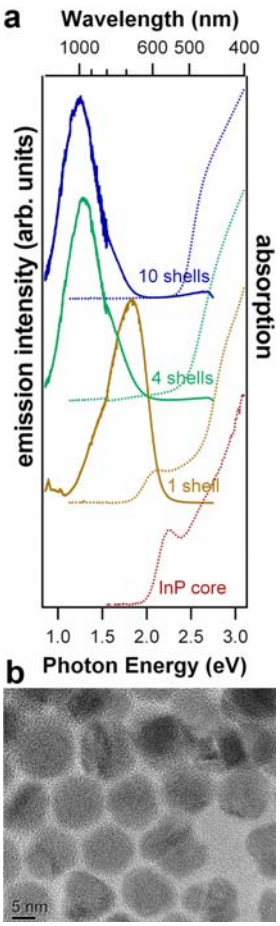

Fig. 2. (a) emission and absorption spectra for InP cores and a core/shell series. (b) TEM image of 10-shell InP/CdS NQDs

Summary

To date, we have shown extreme color tuning as a function of core size and shell thickness/identity, resulting from electronic structure manipulation in the InP-based NQD system. In the case of Cd-containing shell materials, ZnS or ZnSe shells can be added to afford biocompatibility with retention of desirable near-IR emission. Single-NQD blinking properties, as well as redox properties, are under investigation in the context of basic and applied bioscience.

Acknowledgements

This research was supported in part by NIH-NIGMS grant 1R01GM084702–01 and conducted in the US DOE Office of Science User Facility and Nanoscale Science Research Center, CINT.

References

1. Y. Chen, J. Vela, H. Htoon, J.L. Casson, D.J. Werder, D.A. Bussian, V.I. Klimov, and J.A. Hollingsworth, *J. Am. Chem. Soc*., 2008, **130**, 5026.
2. J. Vela, H. Htoon, Y. Chen, Y.-S. Park, Y. Ghosh, P.M. Goodwin, J.H. Werner, N.P. Wells, J.L. Casson, and J.A. Hollingsworth, *J. Biophotonics*, 2010, **3**, 706-717.
3. H. Htoon, A.V. Malko, D. Bussian, J. Vela, Y. Chen, J.A. Hollingsworth, V.I. Klimov, *Nano Lett.*, 2010, **10**, 2401-07.
4. R. Xie, D. Battaglia, and X. Peng *J. Am. Chem. Soc.*, 2007, **129**, 15432-33.
5. S.A. Ivanov, A. Piryatinski, J. Nanda, S. Tretiak, K.R. Zavadil, W.O. Wallace, D. Werder, and V.I. Klimov, *J. Am. Chem. Soc.*, 2007, **129**, 11708-19.
6. H.M. Cheong, H. Fu, A. Zunger, J.R. Sprague, A. Mascarenhas, A.J. Nozik, *J. Phys. Chem. B*, 1997, **101**, 4904-12.

COMPLEX TRANSIENTS IN MULTI-COMPONENT CELL ENSEMBLES

M.V. Ivanchenko and **D.Y. Zorin**

University of Nizhny Novgorod, Russia, ivanchenko@rf.unn.ru

Understanding the mechanisms underlying the regulation of immune cell numbers and diversity is one of the main problems in immunology. Adaptive immune responses to pathogens are triggered by T-cells (a type of white lymphocytes) which exist in many distinct molecular variants (clonotypes). The vast number of clonotypes (T-cell repertoire) is of the order of 10^7–10^8 in humans and this offers protection from all possible infections. It is crucial that T-cell numbers are regulated without compromising this diversity. The number of immune cells of an adult tends to a stationary "homeostatic" distribution followed by a marked decline with ageing. There is experimental evidence that, in the absence of infection, T-cells compete for survival stimuli delivered by professional antigen-presenting cells (APCs) [1]. This competition process clearly regulates both T-cell numbers and diversity. The other factors, chemokine and cytokine signalling are also involved in the homeostatic regulation of lymphocytes. Precise details of signalling are not fully determined yet.

The physical picture of the clonotype selection process is the following. Naive T-cells from each clonotype recognize its own set of antigen-presenting profiles (APPs). Moving in the lymph node T-cells interact with APCs (much at random) and, should recognition occur, get a stimulus for division. Cells also have their characteristic lifetime and die occasionally. The clonotype gets extinct if its proliferation is not rapid enough to replenish losses, be it due to its low APP recognition ability or strong competition with the other clonotypes for access to APCs. The other side of the coin is the possibility of the strongly self-reactive T-cell clonotypes to survive the negative selection in thymus and provoke an autoimmune reaction.

We develop and study a deterministic dynamical model of multi-clonotype T-cell population competing for survival signals from antigen-presenting cells [2, 3]:

$$\dot{n}_i = n_i \left(-\mu + \sum_{q \in Q_i} \frac{\gamma}{n_i + \sum_{j \neq i, q \in Q_j} n_j} \right),$$

where n_i is the size of the i-th of N clonotype populations, μ is the aggregate coefficient for the death/migration to the memory T-cells pool/influx from thumus rate, γ is the birth coefficient, Q_i is the set of APPs recognized by the i-th clonotype, $Q_i = ||Q_i||$, the total number of APPs being Q. We take identical parameters μ, γ for all clonotypes, as the results of numerical simulations with 10% random variations gave qualitatively the same results. We assume that the probability for a given clonotype to recognize a given APP equals p. Thus, the clonotype-APP recognition network is a bipartite random graph described by three parameters N, Q and p, with the intensive parameters $\nu = pN$ and $\rho = pQ$ defining statistical properties.

We find that competition induces an efficacious selection of clonotypes, making the less able and more repetitive get extinct [3]. The distribution of clonotypes sizes turns out to be bimodal with peaks at zero (for the extinct clonotypes) and some non-trivial value (for the persistent ones). The extinction rate $p_0 = p_0(p, N, Q)$, defined as the ratio of extinct clonotypes to their total number N, reaches the minimum as p is increased from zero and N, Q stay fixed near to $p \sim 1/N$. The depth of the minimum depends on Q/N: when APPs are in large excess almost no extinction is observed, but near parity or in shortage the competition becomes strong before the APP recognition gets sufficiently diverse. We have hypothesized that the competition is network-driven and the extinction rate should (approximately) depend on the intensive graph parameters ν and ρ. Plotting the curves for ten times smaller N and Q we observe a strikingly similar behavior and downscaling abscissas by ten we get a very good coincidence indeed. This result paves the way to scale the numerical results for relatively small computationally accessible networks to physiologically relevant sizes.

Based on the available experimental results we estimate for the first time the physiological values of the T-cell receptor – antigen presentation profile recognition probability $p \approx 1.5 \cdot 10^{-7}$ and T-cell clonotypes niche overlap $\nu \approx 15$ [3]. Studying the transient selection processes we demonstrate that they dominate the dynamics over large timescales: years, if not decades, in physiological time.

Moreover, the extinction does not occur in parallel. On the contrary, the weakest clonotypes die first and during that time the stronger ones (also destined to extinction) increase their size. Only after their 'victims' get extinct the stronger ones start effective competition with each other, when the strongest will survive. Therefore, the sequential transient competition leads to the clonotype sizes distribution drastically different from the final stationary state. We argue that what is currently viewed as 'homeostasis' is a complex sequential transient process, while being quasi-stationary in the total number of T-cells only.

Finally, we study the autoimmune tolerance of this complex network competition. We assume that a small number of T-cell clonotypes $N^* << N$ is highly self-reactive with the APP recognition probability $p^* = mp$, $m >> 1$. We measure the asymptotic full numbers of the highly self-reactive clonotypes vs. the ordinary ones and speak about an 'autoimmune' reaction in case of the $O(1)$ ratio. Remarkably, our results indicate that independent on particular numbers of N and N^*, the network competition provides tolerance for moderate m, its break up occurring at $m \sim 8$ only. Remarkably, the long-term persistence of autoimmune clonotypes has been demonstrated in recent experiments [4, 5]. Further experimental advances in high-throughput DNA sequencing that allow for constructing T-cell receptor libraries and quantifying the clonal pool appear extremely promising as the data source and test bed for the future theoretical and numerical analysis.

References

1. A. Freitas and B. Rocha, *Immun. Today*, 1993, **14**, 25.
2. E. Stirk, C. Molina-Paris, and H. van den Berg, *J. Theor. Biol*., 2008, **255**, 237.
3. M.V. Ivanchenko, *JETP Letters*, 2011, **93**, 35.
4. I.Z. Mamedov *et al., Autoimmunity*, 2009, **42**(6), 52.
5. A.V. Chkalina et al., Russian Journal of Bioorganic Chemistry, 2010, **36**, 206.
6. I.V. Zvyagin et al., *Cellular and molecular immunology*, 2010, **7**, 471.

Invited

HIGHLY SENSITIVE DETECTION OF HUMAN CARDIAC MYOGLOBIN USING REVERSE SANDWICH IMMUNOASSAY WITH GOLD NANOPARTICLES-ENHANCED SPR BIOSENSOR BIACORE-3000

A.S. Ivanov, O.V. Gnedenko, Yu.V. Mezentsev, A.A. Molnar, and **A.V. Lisitsa**

Institute of Biomedical Chemistry RAMS, Moscow, Russia, alexei.ivanov@ibmc.msk.ru

Introduction

Myoglobin is an oxygen binding protein that is present in cardiac and skeletal muscle cells. Cardiac myoglobin (Mb) is an early biomarker for diagnosis of acute myocardial infarction (AMI). Due to its low molecular weight, Mb is rapidly released into blood when muscle cells are damaged [1–2]. Unfortunately, all the used immuno-assays for biomarkers have insufficient accuracy. Therefore, more accurate assays are being intensively developed. One such promising approach is a surface plasmon resonance (SPR) biosensor [3] which has higher precision and reproducibility compared with ELISA [4–7].

However, detection limit of SPR analysis of protein biomarkers by direct registration of analyte interaction with immobilized monoclonal antibody is only about 1 nM, while the level of AMI biomarkers in blood serum is at picomolar concentrations. That is why the increase of SPR biosensor sensitivity is extremely important for creation of new diagnostic methods.

Application of gold nanoparticles (AuNP) for SPR signal amplification seems to be the most promising approach, since the biosensor signal is directly proportional to the mass of material which binds to the sensor surface. Usually AuNP conjugated with second antibody is used as an amplification agent that interacts with analyte already bound with the first antibody on the sensor surface (direct sandwich immuno-assay). The purpose of this study was to develop highly sensitive reverse sandwich immuno-assay for human Mb (fig. 1) with using AuNP-enhanced SPR biosensor [8].

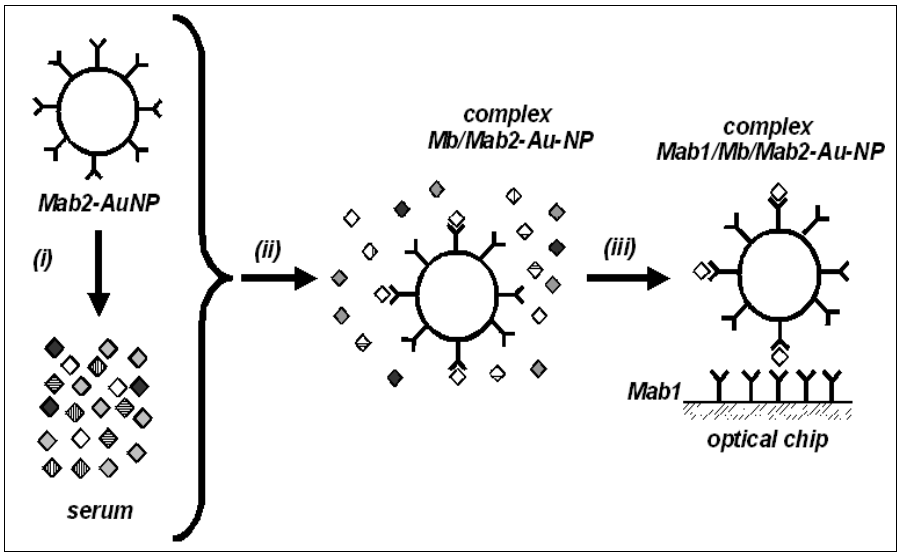

Fig. 1. Three steps of assay:
(i) mixing a serum sample with Mab2-AuNP conjugate;
(ii) sample incubation for Mb/Mab2-AuNP complex formation;
(iii) sample injection over biosensor surface and registration of Mab1/Mb/Mab2-AuNP complex formation

Materials and methods

All SPR experiments were performed on biosensor Biacore 3000 (GE Healthcare) with sensor chips CM3 and HBS as a running buffer. All reagents for Biacore biosensor were obtained from GE Healthcare. Cardiac myoglobin (Mb), matched pair of anti-Mb monoclonal antibodies (Mab1 and Mab2) and human myoglobin free serum were obtained from USBio. Myoglobin from skeletal muscle (sMb) was obtained from Serva. Covalent immobilization of proteins on the chip surface was carried out by a standard amino-coupling Biacore protocol.

The interactions of different analytes with immobilized Mab1 were studied in the range of analytes concentrations 1 pM – 20 nM in HBS. The sensing surface was stable for >30 binding and regeneration cycles enabling to re-use sensor chip.

AuNP were synthesized by reducing $HAuCl_4$ [9]. Mab2-AuNP was prepared by mixing Mab2 solution with AuNP suspension, incubation at room temperature and blocking by BSA [8].

Results and discussion

In comparison with direct binding reaction of Mb with Mab1 on the sensor surface (fig. 2, curve 1) or binding of complex Mb/Mab2 (curve 2), the binding of complex Mb/Mab2-AuNP (curve 3) amplified the biosensor signal about 5 and 30 fold. The limit of detection of Mb in human blood serum was found to be 5 nM for direct assay (fig. 3, curve 1) and 10 pM for AuNP-enhanced reverse sandwich assay (curve 2). In the latter case, the measuring range covered Mb concentrations in human blood serum from 10 pM to 10 nM. The inter-assay coefficient of variation (CV) was less than 3%.

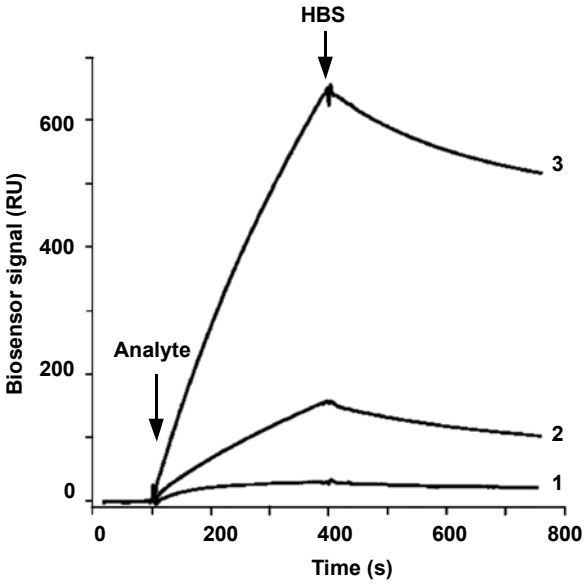

Fig. 2. Typical sensorgrams of interaction of Mb (1), complexes Mb/Mab2 (2) and Mb/Mab2-AuNP (3) with immobilized Mab1 on the chip CM3

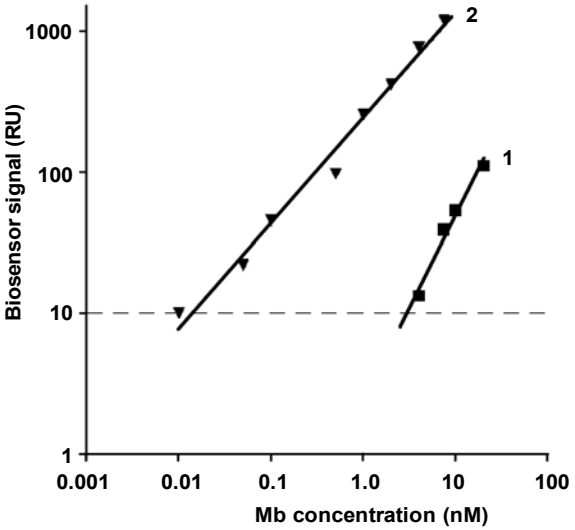

Fig. 3. Dependence of equilibrium biosensor signal on Mb concentration in human blood serum.
1 – direct assay;
2 – AuNP-enhanced reverse sandwich assay

Future research includes optimizing the technique for further signal enhancement and applying this technique to other protein biomarkers. It should be noted that the principle of this analysis allows combining several assays in simultaneous analysis of a single serum sample by mixing with a mixture of immunogold reagents and separate analysis in different channels of SPR biosensor with corresponding immobilized Mabs 1.

Acknowledgements

This work was supported by the Russian Federal Program (State contracts 02.740.11.0306 and 16.740.11.0372). The authors thank the GE Healthcare (Russia) for scientific and technical support.

References

1. M. Kemp, J. Donovan, H. Higham, and J. Hooper, *British J. Anaesthesia,* 2004, **93**, 63-73.
2. R.H. Christenson and H.M. Azzazy, *Clin. Chem.*, 1998, **44**, 1855-1864.
3. J. Homola, H. Vaisocherová, J. Dostálek, and M. Piliarik, *Methods*, 2005, **37**, 26-36.
4. V.I. Avramis, E.V. Avramis, W. Hunter, and M.C. Long, *Anticancer Res.*, 2009, **29**, 299-302.
5. F.D. Lung, H.Y. Chen, and H.T. Lin, *Protein Pept. Lett.*, 2003, **10**, 313-319.
6. H. Vaisocherová, V.M. Faca, and A.D. Taylor, *Biosens. Bioelectron.*, 2009, **24**, 2143-2148.
7. A. Nechansky, *J. Pharm. Biomed. Anal.*, 2010, **51**, 252-254.
8. O.V. Gnedenko, Yu.V. Mezentsev, A.A. Molnar, A.S. Ivanov, and A.I. Archakov, *Molecular medicine,* 2010, **4**, 52-54 (in Russian).
9. M. Wang, L. Wang, G. Wang, X. Ji, Y. Bai, and T. Li, *Biosens. Bioelectron.*, 2004, **19**, 575-582.

FLUORESCENT NANODIAMOND COMPLEXES ON THE BASE OF BARNASE: BARSTAR INTERACTION

E.A. Ivukina[1], **V.K.A. Sreenivasan**[2], **O.A. Stremovskiy**[1], **A.V. Zvyagin**[2], and **S.M. Deyev**[1]

[1] Shemyakin and Ovchinnikov Institute of Bioorganic Chemistry, Russian Academy of Science, Moscow Russia
katya.ivukina@rambler.ru
[2] MQ Photonics Centre, Faculty of Science, Macquarie University, Sydney, Australia

Development of a rapid, accurate, and biotechnological method for detecting the oncomarkers associated with the progressive tumor growth and unfavorable prognosis for a patient is still an urgent task of current molecular immunology. Tumor-targeted vectors with specific antitumor antibodies and other targeting molecules are promising tools for cancer therapy and visualization of tumor cells.

Multivalent complexes of targeting proteins with nanoparticles provide high efficacy and highly selective binding [1]. Fluorescent nanodiamonds (NDs) represent an attractive material for optical diagnostics as well as potential cancer cell-targeting agents. ND is nanocrystallite comprising a stable core hosting colour centers [often, nitrogen vacancy (NV)]. Under a green-laser excitation the NV colour centers emit bright red luminescence, which may prove useful for *in vivo* application. In addition, low cytotoxicity and photostability make it an attractive tool for biolabelling and cell targeted delivery purposes [2].

The surface of ND particles contains a complex array of surface groups, including carboxylic acids, ethers, lactones, amines, etc. that are introduced during purification and modification stages. Therefore, the surface of diamond allows linkage of amino acids, peptides, proteins, carbohydrates, nucleic acids, and drugs [3]. Conjugates with optically bright, surface-functionalised NDs can serve as potential biolables.

We have developed a method of ND bioconjugation with proteins promising future production of immunocomplexes with these nanoparticles and targeting molecules.

Since targeting molecules are often sensitive to extreme conditions of conjugation process the use of a linker between targeting molecules and NDs is more preferable. We used a very high-affinity protein pair barnase:barstar (Bn:Bs), whose terminal groups provide convenient docking terminals and can serve as a perfect linker. Bn, a bacterial ribonuclease, and its inhibitor, Bs bind together strongly and specifically. The resulting Bn:Bs complex is temperature-stable, and extremely robust under alkaline and acidic conditions that allows avoiding loss of protein functionality during conjugation process. Besides, Bn and Bs, when attached to a targeting molecule via a hinge region, can thus serve as building blocks for multivalent mini-antibodies that mimic the rotational and segmental flexibility of the natural antibody binding arms [4, 5].

We have engineered a novel fluorescent complex of ND with green fluorescent protein EGFP [6] based on Bn:Bs module [ND-Bs:Bn-EGFP (Figure 1)].

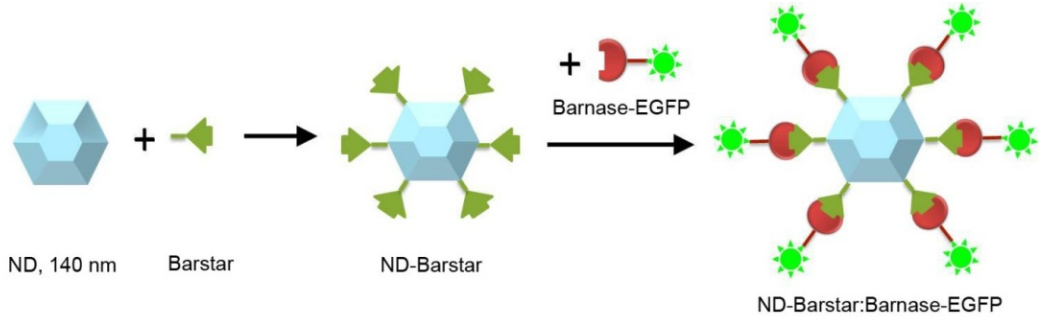

Fig. 1. Assembly of nanodiamond-EGFP complex via barnase: barstar module

Using 140-nm NDs we obtained covalent conjugates with a thousand of Bs molecules per one particle. Bioconjugation took advantage of oxygen-containing functional groups on the surface of high-temperature oxidised NDs. Chemical protocol of conjugation was based on water-soluble derivatives of 1-Ehyl-3-(3-dimethylamiopropyl)-carbodiimide-hydrochloride (EDS) and N-Hydroxy-sulfo succinimide (sulfo-NHS), which relies on the presence of carboxyl groups on the ND surface [7].

Reaction 1: ND aqueous colloid was activated with 1-ethyl-3-(3-dimethyl-aminopropyl) carbodiimide and suflo-N-hydroxy succinimide. The chemical reactivity of the surface made it possible to attach Bs. Activated NDs were added to Bs-solution in phosphate buffer under sonication, which prevented aggregation by promoting Bs-ND reaction pathway, rather than interaction between NDs.

Reaction 2: ND-Bs:Bn-EGFP complex was produced by mixing ND-Bs with an excess of Bn-EGFP. The resulting complex was stable and bright in saline buffers.

The presence in the obtained samples of both NDs and EGFP was confirmed by identification of fluorescence peaks typical for these fluorophores. ND-Bs:Bn-EGFP displayed profound fluorescent spectral signatures of ND and EGFP upon excitation with a 532-nm laser, and 488-nm spectrally-filtered xenon-lamp, respectively. Gradual rising of zeta-potential during the reaction also showed successful binding of the components (Fig. 2).

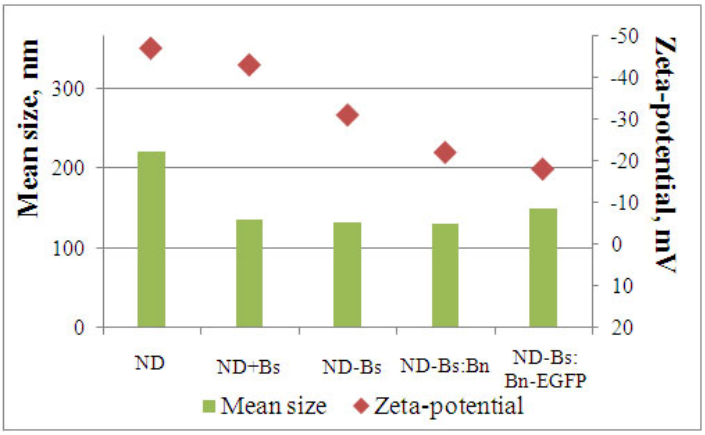

Fig. 2. Measurements of zeta-potential and mean size during conjugation process

In summary, a new, versatile nanodiamond bioconjugation platform based on the high-affinity protein pair, barstar:barnase, has been demonstrated. The reported reaction is simple and delivered covalently bound ND-Bs bioconjugates that were stable in buffer solutions for at least several months. Considerable practical utility of this platform was demonstrated by design, production, and characterization of robust nanodiamond-biomolecule complexes. These data suggest the possibility of designing multivalent constructs of nanodiamonds with antibodies for optical biomedical diagnostic.

Acknowledgements

This work was partially supported by the Russian Academy of Sciences Programs Molecular and Cellular Biology and Nanotechnologies and Nanomaterials, the Russian Foundation for Basic Research Grants # 09-04-01201, the Russian Federal Agency for Science and Innovation; Macquarie University Research Innovation Fund # 1136900.

References

1. M.P. Nikitin, T.A. Zdobnova, S.V. Lukash, O.A. Stremovskiy, and S.M. Deyev, *Proc. Natl Acad. Sci. USA*, 2010, **107**, 5827-5832.
2. A.M. Schrand, S.A.C. Hens, and O.A. Shenderova, *Crit. Rev. Solid State Mater. Sci.*, 2009, **34**, 18-74.
3. A. Kruger, Y.J. Liang, G. Jarre, and J. Stegk, *J. Mater. Chem.*, 2006, **16**, 2322-2328.
4. S.M. Deyev, R. Waibel, E.N. Lebedenko, A.P. Schubiger, A.Pluckthun, *Nat. Biotechnol.*, 2003, **21**, 1486-1492.
5. V.A. Mitkevich, A.A. Schulga, Y.S. Ermolyuk, V.M. Lobachov, V.O. Chekhov, G.I. Yakovlev, R.W. Hartley, C.N. Pace, M.P. Kirpichnikov, and A.A. Makarov, *Biophys. Chem.*, 2003, **105**, 383-390.
6. E.N. Lebedenko, T.G. Balandin, E.F. Edelweiss, O. Georgiev, E.S. Moiseeva, R.V. Petrov, and S.M. Deyev, *Dokl. Biochem. Biophys.*, 2007, **414**, 120-123.
7. Y.R. Chang, H.Y. Lee, K. Chen, C.C. Chang, D.S. Tsai, C.C. Fu, T.S. Lim, Y.K. Tzeng, C.Y. Fang, C.C. Han, H.C. Chang, and W. Fann, *Nat. Nanotechnol.*, 2008, **3**, 284-288.

THE INFLUENCE OF SOLVENT ON THE TOXICITY AND BIODISTRIBUTION OF QUANTUM DOTS IN MICE

N.I. Kazachkina, Y.F. Salykina, V.V. Zherdeva, and **A.P. Savitsky**

A.N. Bach Institute of Biochemistry, Russian Academy of Science, Moscow, Russia, nkazachkina@inbi.ras.ru

At present, quantum dots (QDs) are actively studied as diagnostic and therapeutic agents. The literature describes many different QDs for applications in vivo. It is common practice to inject them into salt solutions. However, it is known that the solution for administration can significantly affect the pharmacological response of drugs.

The current work is devoted to the behavior of QDs in different solvents *in vitro* and *in vivo* studies. The core/double shell – CdSe/CdS/ZnS QDs coated with mercaptopropionic acid were obtained by the methods described in [1, 2] with $\lambda^*_{max} = 615$ nm. The solvents used were water, 5% glucose, 0.9% sodium chloride solution, and PBS (pH 7.4).

Highest stability of the fluorescent properties of nanoparticles was exhibited by salt-free environments, such as water and glucose. In these solvents, there was a slight (approximately 15%) increase in fluorescence intensity for 24 hours, which may be due to their disaggregation. The fluorescence intensity decreased in the presence of salts. So, after 24 h the intensity of fluorescence of the solution of QDs in 0.9% sodium chloride solution and PBS was, respectively, 67% and 8% of the original. No shift of the peak or changes of the fluorescence bandwidth were observed. The highest colloidal stability (as measured by DLS) of QDs was obtained in salt-free environments. Changes of the hydrodynamic radius of nanoparticles were not observed for two hours compared with the initial values when water and glucose were used as solvents. Whereas an increase of hydrodynamic radii was noted in the salt solution after 30 minutes of incubation. QDs were injected intravenously into the lateral tail vein of females C57Bl/6j (Breeding Nursery of Laboratory Animals "Pushchino") in volumes of 0.1 to 0.4 ml with doses of 150 to 600 pmol/mouse. Control animals were administered with solvent.

The introduction of quantum dots led to the death of mice in dose-dependent manner. The death of animals was not observed after introduction of quantum dots in a dose of 150 pmol per mouse. The dose of 300 pmol and 600 pmol per mouse caused deaths of 7 and 10 mice of 26 experimental animals, respectively. 4/8, 6/9 and 3/8 mice died when QDs were injected in water, glucose and water-salt solutions, respectively. Animals died during the first day against the background of the symptoms indicating the presence of alteration of blood flow in the inferior vena cava. This symptom was expressed only in mice treated with QDs dissolved in glucose in a dose of 150 pmol/mouse. Application of other solvents did not result in any noticeable toxic effects.

Distribution of quantum dots in mice was studied by local fluorescence spectroscopy (Cluster, Ltd., Russia). Fluorescent analysis (excitation wavelength – 532 nm) of internal organs (liver, spleen, lungs, kidneys, heart) was performed 24 hours after the injection of QDs. The highest intensity of fluorescence was observed in the liver and lungs. Fluorescence intensity in the liver and lungs was similar when water and glucose were applied as solvents, whereas fluorescence intensity in the liver was nearly 5 times higher than in the lungs when saline solutions were used.

To conclude, nanoparticles in a disaggregated state are detected in the lungs and liver, whereas the aggregates (and, correspondingly, larger particles) are detected to a greater extent in the liver. This correlates with the published data about the biodistribution of nanoparticles depending on size [3]. Thus, it is shown that a solution for injection can affect toxicity and distribution of nanoparticles in animals.

Acknowledgements

This study was supported by grants No. 01.648.11.3003 and No. 01.648.11.3006 from the Federal Agency for Science and Innovation.

References

1. R. Xie, U. Kolb, J. Li, T. Basche, and A. Mews, *J. AM. CHEM. SOC*, 2005, **127**, 7480-7488.
2. B. Pong, B.L. Trout, and J. Lee, *Langmuir*, 2008, **24**, 5270-5276.
3. M.L. Schipper, G. Iyer, A.L. Koh, et al., *Small*, 2009, **5**, 126-134.

Invited

TUNABLE PLASMONIC NANOPARTICLES FOR BIOMEDICAL APPLICATIONS

B.N. Khlebtsov[1], **E.V. Panfilova**[1], **T.E. Pylaev**[1], **V.A. Khanadeev**[1], **G.S. Terentyk**[2], **V.V. Tuchin**[2], **L.A. Dykman**[1], and **N.G. Khlebtsov**[1,2]

[1] Institute of Biochemistry and Physiology of Plants and Microorganisms, Saratov, Russia, bkhl@ibppm.sgu.ru
[2] Saratov State University, Saratov, Russia

The metal (mainly gold) nanoparticles (NPs) have attracted significant interest as a novel platform for nanobiotechnology and biomedicine because of convenient surface bioconjugation with molecular probes and remarkable optical properties related with the localized plasmon resonance (PR) [1]. Here, we give a short review of our recent work on fabrication, optical properties, functionalization, and biomedical applications of plasmon-resonant nanoparticles. Three types of nanostructures are considered: gold or gold/silver nanorods, silica/gold gold nanoshells, and silver/gold nanocages. The plasmonic properties of such nanostructures can be tuned across vis-NIR spectral bands by variation in the particle shape, structure, and composition (Fig. 1).

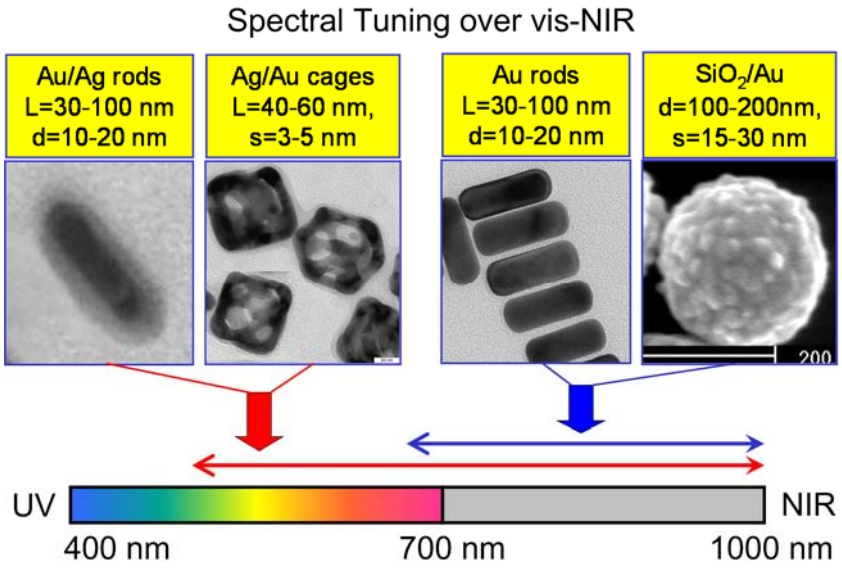

Fig. 1. Spectral tuning of plasmonic properties by variation in the particle shape, structure, and composition

At present, many aspects of the fabrication, bioconjugation, optical characterization, and biomedical application of gold NRs are well documented and extensively reviewed. In particular, photothermal and photoacoustic applications of gold nanorods are especially attractive owing to their highly efficient NIR absorption. Moreover, the strong-intensive longitudinal PR supports several nonlinear phenomena, including two-photon luminescence, which has already been used for cancer cell imaging and for tracking of nanoparticle cellular uptake. In the same line, silica/gold nanoshells with 120-nm silica core and 15–20-nm gold shell can be used as a universal platform for photothermal therapy, label-free immunoassays and genomics, and as contrast agents in optical coherence tomography. The Ag/Au nanocages represent a new class of tunable plasmonic nanostructures with potential attractive biomedical applications. These particles can be fabricated by a two-step technology developed by Xia and coworkers [2]. At the first step, silver nanocubes are prepared by the sulfide-mediated polyol method, in which Ag(I) is reduced to Ag(0) with ethylene glycol in the presence of poly(vinyl pyrrolidone). After fabrication of Ag cubes, they serve as templates for a galvanic replacement reaction between Ag and $HAuCl_4$ and for the formation of a partly hollow Au/Ag alloyed nanostructures called nanocages. This reaction involves the addition of an aqueous $HAuCl_4$ solution to a boiled suspension of Ag nanocubes. The spectral shift of the plasmon resonance from 435 nm to 650-900 nm can be tuned only by controllable addition of $HAuCl_4$, and the reaction can be stopped at any point to fabricate Ag/Au nanocages with a desired particle structure and plasmon resonance wavelength.

A new trend in current nanobiotechnology and theranostics is the fabrication of multifunctional nanoparticles, which combine the therapeutic and diagnostic modalities in a single nanostructure [3].From this point of view, an attractive option is nanostructures combining the unique optical properties of plasmonic nanoparticles with the advantages of mesoporous silica functionalized with appropriate photosensitizer (PS). In this work, we describe a novel type of nanocomposites based on silica-coated Au/Ag nanocages or silica-coated Au nanorods functionalized with the photodynamic sensitizers (hematoporphyrin and Yb-2,4-dimethoxyhematoporphyrin). The fabricated nanoparticles combine several promising theranostic modalities: (i) an easy tunable plasmon resonance across the 650-950 nm spectral band with possible use as plasmonic heating labels; (ii) a mesoporous silica shell that preserves the plasmon resonance from an aggregation shift and provides a convenient possibility of surface or volume functionalization with various molecular probes; (iii) a combination of singlet oxygen generation with an additional 900–1060 nm IR-luminescence band of Yb-HP, which can be used for optically controlled PDT within the tissue transparency window. Figure 2 illustrate a general scheme for fabrication of multifunctional silica-coated nanocages.

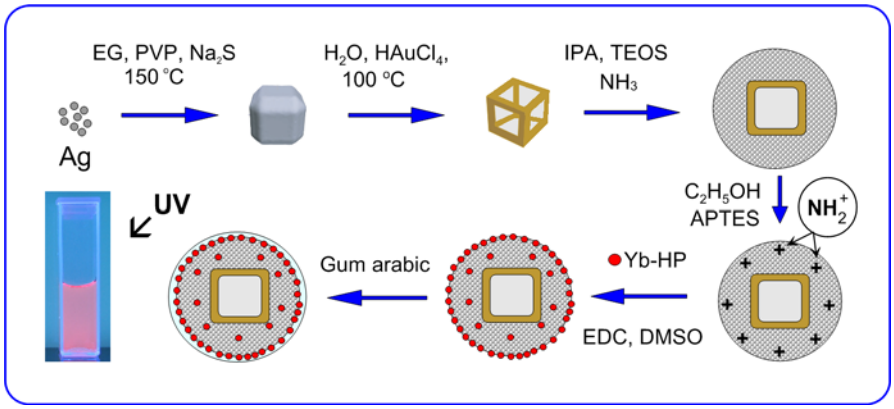

Fig. 2. Schematic illustration summarizing how fluorescent composite nanoparticles can be fabricated starting with Ag nanocubes and ending with silica-coated Au/Ag nanocages functionalized with Yb-HP molecules. The left-bottom photo shows visible fluorescence of a sample under UV excitation. Designations: EG – ethylene glycol, PVP – poly(vinyl pyrrolidone), IPA – isopropyl alcohol, TEOS – tetraethyl orthosilicate, APTES – 3-aminopropyltriethoxysilane, Yb-HP – Yb-2,4-dimethoxyhematoporphyrin, EDC – 1-ethyl-3-(3-dimethylamino-propyl) carbodiimide, DMSO – dimethyl sulfoxide

In addition to the long-wavelength plasmon resonance near 750–800 nm, the composite particles exhibited a 400-nm absorbance peak and two fluorescence peaks, near 580 and 630 nm, corresponding to bound Yb-HP. The fabricated nanocomposites generated singlet oxygen under 630-nm excitation and produced heat under laser irradiation at the plasmon resonance wavelength (750–900 nm). Furthermore, an additional advantage of fabricated conjugates was an IR-luminescence band (900–1060 nm), originating from Yb^{3+} ions of bound Yb-HP and located in the long wavelength part of the tissue transparency window. This modality was used to control the accumulation and biodistribution of composite particles in mice bearing Ehrlich carcinoma tumors in a comparative study with free Yb-HP molecules after intravenous injection. Thus, these multifunctional nanocomposites seem to be an attractive theranostic platform for simultaneous IR-luminescence diagnostic and photodynamic therapy owing to Yb-HP and for plasmonic photothermal therapy owing to Au/Ag nanocages.

Acknowledgements

This research was supported by the Russian Foundation for Basic Research, by grants from the President of the Russian Federation for young scientists MK-1057.2011.2, and by a grant from the Government of the RF designed to support scientific research projects implemented under the supervision of leading scientists at Russian institutions of higher education.

References

1. N.G. Khlebtsov, L.A. Dykman, *J. Quant. Spectr. Radiat. Transfer*., 2010, **111**, 650-658.
2. S.E. Skrabalak, L. Au, X. Li, Y.F. Xia, *Nat. Protoc.*, 2007, **2**, 2182–2190.
3. S.-H. Cheng, C.-H. Lee, M.-C. Chen, J.S. et al., *J. Mater. Chem*., 2010, **20**, 6149-6157.

ADVANTAGES OF DOUBLE POLYMER/SILICA COATED QUANTUM DOTS FOR *IN VIVO* APPLICATION IN THE GASTROINTESTINAL TRACT

Y.F. Loginova (Salykina)[1], V.V. Zherdeva[1], S.V. Dezhurov[2], M.S. Wakstein[2], and **A.P. Savitsky[1]**

[1] A.N.Bach Institute of Biochemistry of RAS, Moscow, Russia, salykina@inbi.ras.ru
[2] Applied Acoustics Research Institute, Center of High Technologies, Dubna, Russia

QDs are 1–10-nm semiconductor nanocrystals with unique optical and photophysical properties, such as size- and composition-tunable emission, high brightness, large absorption cross sections and narrow emission bands [1]. For biomedical applications of QDs their surfaces should be modified so as to make them water-soluble and biocompatible. Generally, the coated QDs are stable under neutral or basic conditions. The development of acid-stable surface coatings is a main goal towards obtaining of QDs that can effectively cross the gastrointestinal tract for various biomedical applications.

The new trend for preparation of ultrastable QDs is to combine the silica and amphiphilic polymer encapsulation techniques [2]. We report here newly synthesized water-soluble CdSe/CdS/ZnS QDs with a previously undescribed combination of polythiol ligands and silica shell (QDs PolyT-APS, d ~ 33 – 36 nm). We have introduced an additional coating on the surface of QDs using silica precursor 3-aminopropyltriethoxysilane (APS) as an amino derivative.

The available studies mainly investigate *in vitro* stability of QDs in chemical conditions, including strong acidic solutions [3]. We demonstrated a maximal colloidal stability of our QDs PolyT-APS not only *in vitro,* but also *in vivo* in the digestive tract of mice after *per os* administration. We also compared our ultrastable QDs with the traditional surface capping method: mercapto compounds (QDs MPA, d ~ 8 – 11 nm) and pendant thiol group (QDs PolyT, d ~ 15 – 16 nm).

At the stage of *in vitro* study we have compared the relative fluorescence intensity, hydrodynamic diameter (HD) and dispersity of QDs solutions after their exposure to an acidic medium (pH 1.0). pH values of QDs solutions were tuned with 0,1M HCl. All samples were characterized by fluorimetry and dynamic light scattering. Measurements of QDs MPA were not conducted due to the almost complete aggregation of these particles at pH 1.0. In the case of QDs PolyT a marked size dispersion increase and a fluorescence intensity significant decrease were observed probably due to the degradation of particles. In contrast, the fluorescence intensity of QDs PolyT-APS and their HD increased at pH 1.0 indicating a slight change in the conformation of particles.

Biodistribution and accumulation of QDs in the digestive tract of mice were monitored *in vivo* by fluorescence whole body imaging and *ex vivo* by the local fluorescence spectroscopy. The colloidal solution of QDs in sterile PBS, pH 7.4 was administered into the stomach of nude or CD-1 mice.

Whole body images were acquired on the imaging system iBox (UVP, USA). Imaging times were adjusted to give maximum dynamic range (over a 24 h period). We observed the strongest fluorescence signal of our QDs PolyT-APS in organs of the digestive system for a long period after administration (up to 4 h) whereas fluorescence of QDs MPA decreased significantly 2 h after administration.

The mice were sacrificed 2 h, 4 h and 24 h after injection of QDs and tissue specimens from the digestive system organs, liver, kidneys and spleen were removed and taken for analysis by the local fluorescence spectroscopy using a laser spectrometer Spectrum-Cluster with excitation wavelength 532 nm. Fluorescence spectra of specimens taken from organs were measured (Table 1).

Table 1. *Ex vivo* fluorescence analysis of the stomach and intestine after animal sacrifice 2-6 h after *per os* administration of QDs according to the data of the local fluorescence spectroscopy

QDs	Stomach after 2 h	Intestine after 2 h	Intestine after 4 h	Intestine after 6 h
MPA	+	–	–	–
PolyT	+	+	±	–
PolyT-APS	+	+	+	+

***** The relative estimation: QDs were not detected (-), low amount of QDs (±), well detectable amount of QDs (+).

The presence of QDs PolyT-APS was clearly seen in spectra of stomach and intestine measured through the interval of 2–6 h since the administration. No traces of any QDs were detected in liver, pancreas and spleen.

Feces and urine probes were collected over a 24 h period after per os administration of QDs and analyzed by the method of local fluorescence spectroscopy to determine elimination routes of QDs. No traces of any QDs were detected in urine probes. The fluorescence of both QDs MPA and QDs PolyT measured in feces probes was very low and was detected only in rare spectra. In contrast, the well detectable fluorescent spectra of eliminated with feces QDs PolyT-APS possessed highest intensity similar to that of the original solution (Fig. 1).

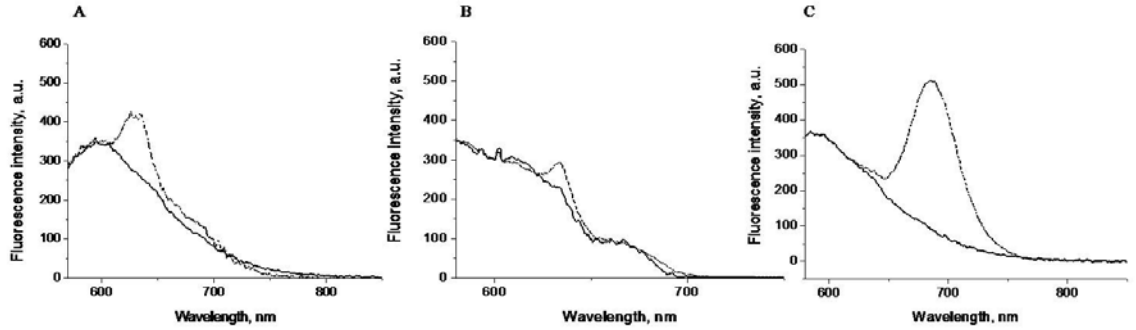

Fig. 1. Fluorescence spectra of feces probes 24 h after per os administration of (A) QDs MPA, (B) QDs PolyT and (C) QDs PolyT-APS: solid curve - feces control, dash curve - feces after administration of QDs

Recently it was shown that a combination of a silica shell with amphiphilic lipid-PEG coating can protect QDs to such a degree that fluorescence remains stable even when treated with acidic solutions pH 1.0 *in vitro* [4]. We demonstrated that our newly synthesized QDs PolyT-APS with a double coating exhibited a maximal colloidal stability not only *in vitro* after their exposure to a strong acidic solution but also *in vivo* in the digestive tract of mice after *per os* administration. We systematically compared the chemical stability of our QDs PolyT-APS with QDs coated by current traditional materials. Nanoparticle coating technologies based on 3-mercaptopropionic acid or pendant thiol groups were not capable of protecting QDs from chemical-induced degradation or surface modification. The presence of silica shell on the surface of QDs PolyT-APS prevents the protonation of functional groups of the organic polymer, their degradation and fluorescence quenching.

Acknowledgements

This study was supported by grants No. 01.648.11.3003 and No. 01.648.11.3006 from the Federal Agency for Science and Innovation. This work was partially supported by grant No. 09-04-12263 from the RFBR.

References

1. I.L. Medintz, H.T. Uyeda, E.R. Goldman, and H. Mattoussi, *Nat Mater.*, 2005, **4**(6), 435-446.
2. M. Darbandi, R. Thomann, and T. Nann, *Chem. Mater.*, 2005, 17, 5720-5725.
3. P.N. Wiecinski, K.M. Metz, A.N. Mangham, K.H. Jacobson, R.J. Hamers, and J.A. Pedersen, *Nanotoxicology*, 2009, **3**(3), 202-214.
4. X. Hu and X. Gao, *ACS Nano*, 2010, **4**(10), 6080-6.

Invited

ON-CHIP LASERS FOR BIOPHOTONIC LAB-ON-A-CHIP APPLICATIONS

T. Mappes[1], **C. Vannahme**[1,2], **T. Großmann**[1,3], **S. Klinkhammer**[2,1], **M. Hauser**[3], **T. Beck**[3], **U. Bog**[1], **T. Wienhold**[1], **M.B. Christiansen**[4], **A. Kristensen**[4], **U. Lemmer**[2], and **H. Kalt**[3]

[1] Institut für Mikrostrukturtechnik, Karlsruhe Institute of Technology (KIT), 76128 Karlsruhe, Germany, timo.mappes@kit.edu; www.biophotonic-systems.com
[2] Lichttechnisches Institut, Karlsruhe Institute of Technology (KIT), 76128 Karlsruhe, Germany
[3] Institut für Angewandte Physik, Karlsruhe Institute of Technology (KIT), 76128 Karlsruhe, Germany
[4] DTU Nanotech, Technical University of Denmark (DTU), DK-2800 Kongens Lyngby, Denmark

Lab-on-a-chip (LOC) systems enable biomedical or chemical testing for point-of-care analysis at the patient's bedside or in the field. Our work is focused on developing optical LOCs based on polymers by integrating microfluidic channels, optical waveguides, and miniaturized lasers on different platforms.

The chips introduced in our work are using optical and fluidic interconnects only. While some photonic structures require features with lateral dimensions in the range of 100 nm, the microfluidic channels are more than one order of magnitude above this regime. In order to allow for mass production, the processes for multiscale replication of the chips are optimized for a minimal number of parallel production steps.

Three different approaches to integrate miniaturized solid state or liquid core lasers are presented within this talk. The respected demonstrators enable choosing the emission wavelength of the lasers within a broad spectral range in the visible:

(1) Chips out of poly(methyl methacrylate) (PMMA) with integrated solid state lasers [1]. Here, the organic semiconductor aluminum tris(8-hydroxyquinoline) (Alq3) doped with the laser dye 4-dicyanomethylene-2-methyl-6-(p-dimethylaminostyryl)-4H-pyran (DCM) is used as gain medium and evaporated on top of predefined distributed feedback (DFB) gratings replicated into PMMA. The emission wavelength of these lasers may be selected within a spectral range of more than 50 nm. The optimized excitation of several fluorescent markers on chip may be realized with these devices [2] (Fig. 1).

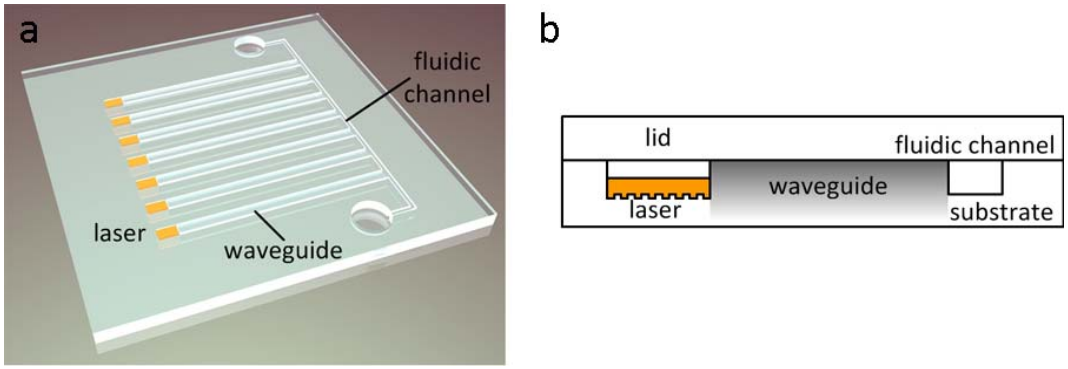

Fig. 1. Scheme of PMMA chip in the size of a microscope cover slip (18 x 18 mm^2) with seven integrated organic semiconductor lasers, microfluidic channel and polymer waveguides. (a) bird's eye view, (b) cross section through the chip [2]

(2) Optofluidic lasers chips, generated in Cyclo-Olefin-Copolymer (COC) foils that may be easily steam sterilized. As liquid gain medium the Pyrromethene 597 dye is dissolved in benzyl alcohol, serving as liquid laser waveguide when inserted in shallow microfluidic channels with DFB gratings structured on the ground. Output pulses of about 1 µJ may be realized with these chips [3] (Fig. 2).

(3) In addition Silicon chips serve as substrates to integrate a novel geometry of micro resonators out of PMMA [4] with quality factors well above 10^6: Micro goblets (Fig. 3a). Micro goblets allow for an optical detection of binding events by measuring shifts of their resonance frequencies. Applying a biofunctionalization to the surface of the goblets enables the selective and label-free detection on chip [5]. Doping the polymer PMMA with Rhodamine 6G allows for applying these resonators as miniaturized lasers on chip [6] (Fig. 3b).

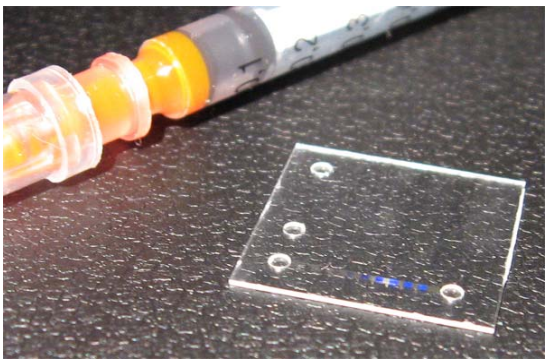

Fig. 2. Photo of a optofluidic laser chip out of COC in the size of a microscope cover slip (18 x 18 mm^2) and a height of 350 µm. The chip integrates different DFB grating periods on the bottom of the channel, serving as a resonator for discrete different lasing wavelengths [3]

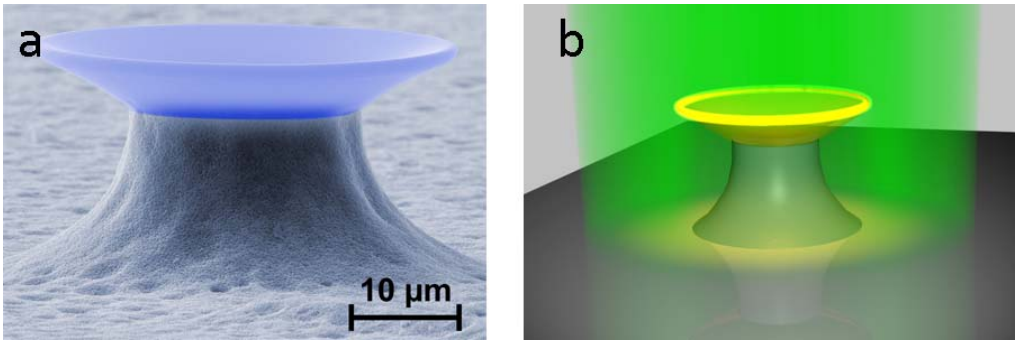

Fig. 3. Microresonators in the form of micro goblets. (a) SEM of a micro goblet, PMMA on a silicon pedestal. (b) CAD image of a micro goblet, to operate the micro goblet as a free space optically pumped integrated laser on a chip, the PMMA is doped with an organic dye [3]

The monolithical integration of optical waveguides into PMMA chips via deep ultra violet lithography may enable for fluorescent excitation of living cells [7]. Combining these waveguides with lipid gratings defined via dip-pen nanolithography will open up for marker free optical detection [8], suited to be combined with the technology platforms mentioned above.

Acknowledgements

This work has been supported by the DFG Research Center for Functional Nanostructures (CFN) Karlsruhe. T.M.'s Young Investigator Group (YIG 08) received financial support from the Concept for the Future of the Karlsruhe Institute of Technology (KIT) within the framework of the German Excellence Initiative. T.G. gratefully acknowledges financial support of the Deutsche Telekom Stiftung. T.G., M.H., U.B., T.W., C.V., and S.K. are pursuing their Ph.D. within the Karlsruhe School of Optics and Photonics (KSOP).

References

1. C. Vannahme, A. Kolew, S. Klinkhammer, P.-J. Jakobs, M. Guttmann, S. Dehm, U. Lemmer, T. Mappes, *Microelectronic Engineering*, 2010, **87**(5-8), 693-695.
2. C. Vannahme, S. Klinkhammer, U. Lemmer, T. Mappes, *Optics Express*, 2011, **19**(9), 8179-8186.
3. C. Vannahme, M.B. Christiansen, T. Mappes, A. Kristensen, *Optics Express*, 2010, **18**(9), 9280-9285.
4. T. Grossmann, M. Hauser, T. Beck, C. Gohn-Kreuz, M. Karl, H. Kalt, C. Vannahme, T. Mappes, *Applied Physics Letters*, 2010, **96** (1), 013303.
5. T. Beck, M. Hauser, T. Grossmann, D. Floess, S. Schleede, J. Fischer, C. Vannahme, T. Mappes, H. Kalt, *Proceedings of the SPIE*, 2011, **7888**, 78880A.
6. T. Grossmann, S. Schleede, M. Hauser, M.B. Christiansen, C. Vannahme, C. Eschenbaum, S. Klinkhammer, T. Beck, J. Fuchs, G.U. Nienhaus, U. Lemmer, A. Kristensen, T. Mappes, H. Kalt, *Applied Physics Letter*s, 2010, **97**(6), 063304.
7. M. Schelb, C. Vannahme, A. Welle, S. Lenhert, B. Ross, T. Mappes, *Journal of Biomedical Optics*, 2010, **15**(4), 041517.
8. S. Lenhert, F. Brinkmann, T. Laue, S. Walheim, C. Vannahme, S. Klinkhammer, M. Xu, S. Sekula, T. Mappes, T. Schimmel, H. Fuchs, *Nature Nanotechnology*, 2010, **5**, 275-279.

QUANTITATIVE ANALYSIS OF NBI IMAGES FOR IMPROVING DIAGNOSIS OF ESOPHAGEAL AND STOMACH PATHOLOGY

N.N. Mitrakova, E.V. Peganova, V.L. Ryzhkov, A.A. Mitrakov, and **A.A. Rozhentsov**

Mari State Hospital, Mari State University, Yoshkar-Ola
Privolzhsky District Medical Center, Nizhny Novgorod
endomitrakova@mail.ru

Introduction

Narrow band imaging (NBI) is an endoscopic technique that enables specialists to localize areas of inflamed and neoplastic processes and sometimes to detect some pathology which is hardly noticeable by standard imaging techniques. There is a connection between the presence of pathology and changes in the color of NBI images. So, the majority of pathological changes give blue and grey NBI images. Healthy mucosa is lilac and pink colored in the NBI mode. According to the IPCL pattern classification there are some grades of inflammation based on the capillary pattern of mucosal surface. According to the Kudo classification, more severe cases correspond to more cut papillary capillary patterns. But there is no digital data which can show the correlation between color and degree of cutting of the capillary pattern in inflamed and healthy tissues, that is why diagnosis, biopsy site, and strategy of treatment may be subjective.

The goal of the study was creation of a method of quantitative analysis of pathological changes in endoscopic NBI images and their digital description, as well as improvement of diagnostic accuracy of NBI endoscopy of precancerous changes (metaplasia and dysplasia) in esophagus and stomach.

Materials and Methods

Endoscopic investigations were performed with the endoscopic system OLYMPUS EXERA II using Narrow Band Imaging, High Definition TV and digital zoom techniques. The system allows assessing vessels and mucosa pattern using some characteristics of light spectrum. Color and geometrical parameters of NBI images were analysed for obtaining objective characteristics.

350 patients with reflux-esophagitis and 720 patients with atrophic gastritis were examined endoscopically. Metaplasia (fundus, cardiac and intestinal types) and dysplasia of epithelium were detected using the NBI mode and 50x digital zoom.

Columnar metaplasia of the distal part of esophagus has a pattern of a round pit structure in the case of cardiac type, an oval pit structure in the case of fundus type, and a regular ridged structure in the case of intestinal metaplasia type. A capillary pattern was well visualized using the NBI mode in each case of metaplasia and was assessed for unidirectionality and uniformity of branching which correspond to good blood supply and absence of epithelial dysplasia.

Detection of disturbed mucosa pattern and different-size spiroid vessels gave grounds to diagnose epithelial dysplasia. Differential diagnosis between low-grade and high-grade dysplasia is based on the degree of irregularity and vessel pattern abnormalities. Low-grade dysplasia was diagnosed in the case of an irregular ridged pattern. High-grade dysplasia or early cancer was diagnosed in the case of a structureless pattern or presence of pathologic vessels. Detection of metaplasia and dysplasia using the NBI mode was followed by targeted biopsy.

Color characterictics of NBI images were analysed using special software created using C# language (Fig. 1). The software allows establishing correspondence between NBI image pixel and definite colors (pink, blue, grey, lilac) and forming the image mapping results of color distribution. The palette may change depending on the type of study. According to results of NBI image statistic analysis standard pallets were made which summarize information about color characteristics of healthy and pathologic tissues. The software permits analysing images and video files which were made in real time or taken from archives.

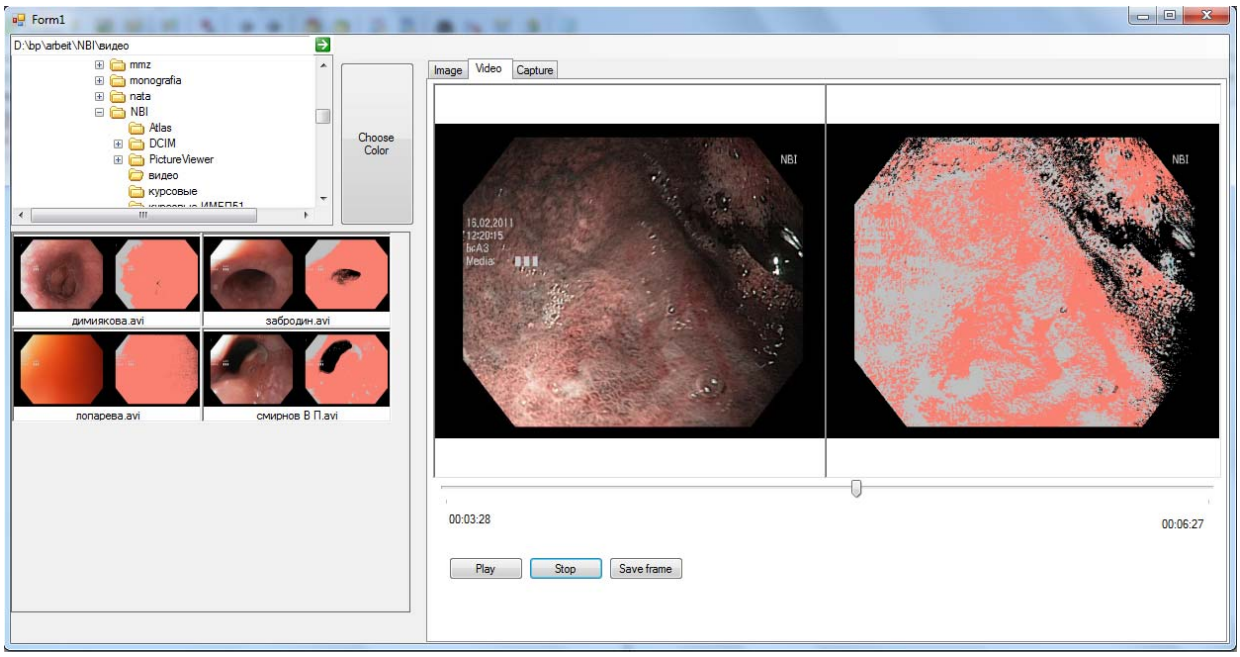

Fig. 1. Software Interface

Results

We have shown that healthy tissues are pink, while tissues with abnormal changes are grey. There were no lilac or blue pixels in the edited pictures. Results of color segmentation of NBI images with different types of abnormalities are presented in Fig. 1.

Clinically, during endoscopic studies using NBI, HDTV and zoom the morphologically confirmed IV-degree reflux esophagi is was detected in 38 (10.8%) cases. In 11 (3.1%) of these cases absence of metaplasia was detected, columnar metaplasia was detected in 27 (7.7%) cases, among them in 9 cases (2.6%) cardiac type metaplasia was detected, in 6 cases (1.7%) fundus type, in 4 cases (1%) intestinal metaplasia, in 4 cases (1%) low-grade epithelium dysplasia, in 2 cases (0.6%) high-grade epithelial dysplasia/incipient neoplasia was diagnosed.

Among patients with atrophy gastritis in 56 (7.7%) cases intestinal metaplasia was detected, in 21 (2.9%) cases low-grade epithelial dysplasia, high-grade epithelial dysplasia/incipient neoplasia was detected in 7 (0.9%) cases.

Invited

ADVANCED LABEL-FREE BIOSENSORS WITH LOW-COST CONSUMABLES FOR NANOBIOTECHNOLOGY RESEARCH AND *IN VITRO* DIAGNOSTICS

A.V. Orlov[1], M.P. Nikitin[1], I.A. Sergachev[2], M.V. Valeiko[3], B.G. Gorshkov[3], and **P.I. Nikitin[3]**

[1]Moscow Institute of Physics and Technology (State University), Dolgoprudniy, Moscow Region, Russia
[2]Lomonosov Moscow State University, Russia
[3]Prokhorov General Physics Institute, Russian Academy of Sciences, Moscow, Russia,
e-mail: nikitin@kapella.gpi.ru

Introduction

Label-free optical methods become very popular for nanobiotechnology research and biosensing. However, the majority of label-free methods employ thin-film structures with metal or dielectric films. The related biochips are rather expensive for medical diagnostics, which requires single-use biochips. Hence, in reality the total cost of label-free assay is usually much higher than that of many label-based assays. Spectral-correlation label-free method and affordable glass slip biochips [1–4] have been optimized for very sensitive and real-time investigation of biomolecular interactions. The combination of the related biosensing instrument named Picoscope® with the functionalized magnetic nanoparticles (MP) significantly improved (3 orders of magnitude) the detection limit of antigens for *in vitro* diagnostics.

Experiments

As an optical label-free biosensor, the Picoscope® [1–4] was used for real time detection of sequential biochemical binding of immunoreagents on the surface by measuring the layer thickness change at a picometer scale (averaged over sensor surface – Fig. 1). The biochip was a conventional microscopic glass slip with a thickness of 100 μm.

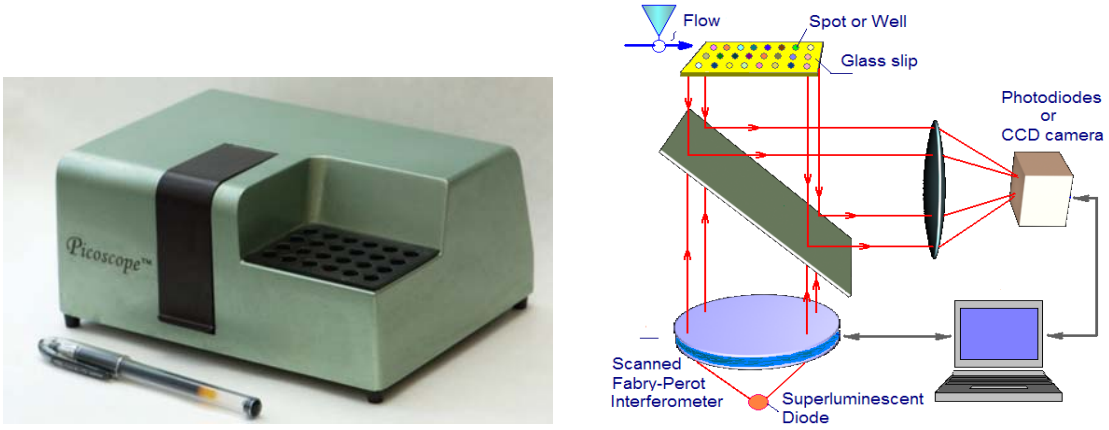

Fig. 1. Photo and optical scheme of the Picoscope®

Applications

In the previous years Picoscope® devices have been successfully employed for screening pharmaceutical substances, lectins, for infection agents and food pathogen detection, for epitope mapping of different monoclonal antibodies, immunotherapy research, monitoring biotechnological processes such as bacteriocin production, etc. [4].

In this paper recent results concerning application of Picoscopes® for investigation of the mechanisms of new medical drugs are discussed. The devices have been successfully employed for studying new cardio drugs, namely, for investigation of a dodecapeptide (peptide X) produced from C-terminal domain of monocyte chemotactic protein -1 (MCP-1). This peptide X possessed an anti-inflammatory activity [5, 6]. The findings allowed us to conclude that the anti-inflammatory effect of the peptide X is related to inhibition of MCP-1 binding to glycosaminoglycans, especially to heparin. The experimental data suggest that chemokine concentration via binding to glycosaminoglycans on the surface of leukocytes and endothelial vessel cells is essential for their migration activity.

Using Picoscope® reversible changes of the height of polymer brushes containing phenylboronic acid were studied. It was found that the polymer brush thickness underwent reversible changes of 0.5–1 nm in response to the changes in the composition of the contacting aqueous phase from deionized water to bicarbonate buffer and vice versa. This is due to the conformational transition of the weak polyelectrolyte to the more extended electrically charged state [7]. Adsorption of mucin glycoprotein to the polymer brush took place due to boronate/sugar interactions between the glycoprotein and the graft copolymer and resulted in a further increase of the brush height by 1.5 nm.

The applications of Picoscope® for *in vitro* diagnostics have been also developed. First of all, using the device various ways for immobilization of biomolecules onto the glass surface have been tested and optimized. Besides, the experiments demonstrated that a combination of Picoscope® with functionalized MP benefits the assay due to possibilities for pre-enrichment of antigen and sample "cleaning" using magnetic separation; increased sensitivity for amplification of optical response; active acceleration of binding of immunoreagents by external magnetic field manipulation; decreased non-specific binding; realization of "magnetic washing" by magnetic field gradients, etc. Detection of the cardiomarker Troponin I (cTnI) was recorded at 0.1 ng/ml concentration level as shown in Figs. 2, 3.

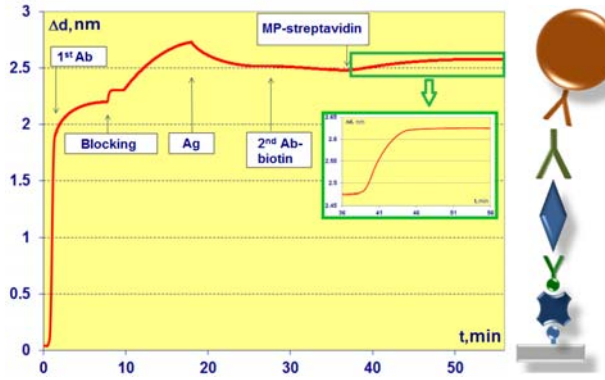

Fig. 2. Sensogram of cTnI detection by MP

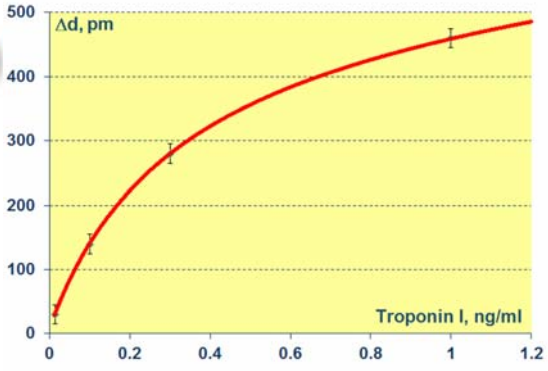

Fig. 3. Optical response to cTnI concentration

The developed assay protocols were transferred to our second format, namely, to Magnetic ImmunoAssays (MIAtek™) technology, which is based on electronic detection of MP by non-linear magnetization [8,9]. For implemented sandwich immunoassays on the 3D filters the detection limit of 15 pg/ml of cTnI was achieved and the assay time did not exceed 25 min.

Experiments have demonstrated that the optical biosensing devices are very efficient for rapid selection of protocols, reagents and buffers for highly sensitive magnetic immunoassays for detection of bacteria and soluble proteins as well as for many other bio- and medical applications.

Acknowledgements. The research was supported in part by the Governmental Contracts No. 16.512.11.2124 and 14.740.11.0450 and by the RFBR grants.

References

1. P.I. Nikitin, B.G. Gorshkov, M.V. Valeiko, and S.I. Rogov, *Quantum Electronics*, 2000, **30**, 1099-1104.
2. P.I. Nikitin, M.V. Valeiko, and B.G. Gorshkov, *Sensors and Actuators B*, 2003, **90**, 46-51.
3. P.I. Nikitin, B.G. Gorshkov, E.P. Nikitin, and T.I. Ksenevich. *Sensors and Actuators B*, 2005, **111-112**, 500-504.
4. P.I. Nikitin. Picoscopes, New Label-Free Biosensors, in: *Handbook of Biosensors and Biochips*, ed. R. Marks et al., 2007. Wiley, ISBN 978-0-470-01905-4.
5. T.L. Krasnikova, P.I. Nikitin, T.I. Ksenevich, B.G. Gorshkov, A.V. Orlov, M.V. Sidorova, A.A. Azmuko, T.I. Arefieva, E.N. Mamochkina, E.E. Efremov, and Zh.D. Bespalova, *Dokl Biol Sci*. 2010, **433**, 289-292.
6. T.L. Krasnikova, P.I. Nikitin, T.I. Ksenevich, S.G. Gorshkov, T. L. Bushueva, T.I. Arefieva, N.Yu. Ruleva, M.V. Sidorova, A.A. Azmuko, Zh. D. Bespalova, *Biologicheskie Membrany*, 2011, **28**, 68-76.
7. A.E. Ivanov, N. Solodukhina, M. Wahlgren, L. Nilsson, A.A. Vikhrov, M.P. Nikitin, A.V. Orlov, P.I. Nikitin, M.V. Kuzimenkova, and V.P. Zubov, *Macromolecular Bioscience*. 2011, **11**, 275-284.
8. P.I. Nikitin, P.M. Vetoshko, and T.I. Ksenevich, *Sensor Letters*, 2007, **5**, 296-299.
9. P.I. Nikitin, P.M. Vetoshko, and T.I. Ksenevich, *J. Magn. Magn. Mater*., 2007, **311**, 445-449.

Invited

MASS SPECTROMETRY OF LARGE BIOMOLECULES (REVIEW)

E.N. Nikolaev

[1] Institute for Energy Problems of Chemical Physics RAS, Moscow, Russia
[2] Institute of BioChemical Physics RAS, Moscow, Russia
e-mail: ennikolaev@rambler.ru

During the last two decades mass spectrometry (MS) evolved from a chemical instrument to mainly a biological one. It can deal with very high molecular weight biological molecules and their complexes [1, 2]. Advances in time-of-flight instruments and ion mobility have underpinned this new role of MS in structural biology [3–5]. Determination of molecular weight, stoichiometry, and assembly patterns of essential biological assemblies as large as MDa hepatitis B virus assemblies has become possible [6].

To identify the constituents of a protein complex, information about the subunits of a complex is needed. Collisionally activated dissociation (CAD) [1], black-body infrared dissociation (BIRD) [7], electron-capture dissociation (ECD) [8], infrared multiphoton dissociation (IRMPD) [9], and surface-induced dissociation (SID) [10] can yield some sequence information for proteins in large assemblies. Collisions at keV laboratory energy demonstrate that native protein complexes can be disassembled into peptide fragments [11]. ECD [12], now an established tool for top-down sequencing and for determining post-translational modifications, can successfully characterize, in part, proteins of MW up to 200 kDa [13].

Fourier transform ion cyclotron resonance (FT ICR) MS became one of the most powerful techniques for this type of research. It can be easily combined with all available dissociation methods. FT ICR MS and ECD combine as an appealing approach for study of protein assemblies because the masses of the complex and of the subunits, as well as some sequence of the constituents can be acquired in a single experiment. Successful ECD-based FT ICR MS top-down approach has been reported that affords composition, stoichiometry, and partial sequence of up to 150 kDa noncovalent protein assembly; namely, the yeast alcohol dehydrogenase (ADH) tetramer.

To deal with such big molecules very high mass resolution and mass accuracy are needed. Recently we have introduced a new type of FT ICR measuring cell [14, 15] based on Penning ion trap with shaped excitation and detection electrodes. This type of cell provides practically pressure limited resolution.

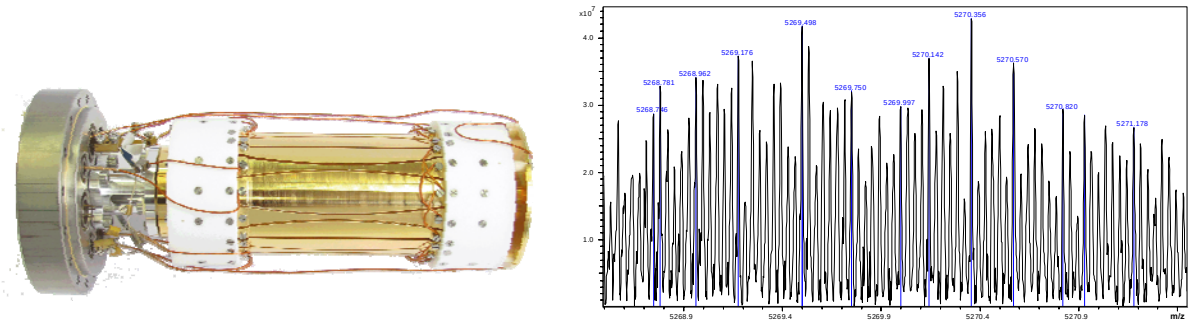

The new type of FT ICR measuring cell with profiled excitation, detection and trapping electrodes for dynamic harmonization of the trapping field to remove the effect of ion cyclotron motion dephasing during signal detection has been experimentally characterized. Its performance has been compared with Bruker "infinity" cell and an open cell with 6 compensation electrodes on the same FT ICR mass spectrometer for peptides and proteins. We have compared mass resolution, mass accuracy and maximum achievable cyclotron radius for these three cells. The last parameter has been determined by measuring odd harmonics in the ICR signal.

The new dynamically harmonized cell is constructed and manufactured (see the figure). In this cell axial quadratic distribution of the electric potential is achieved by shaping cell excitation and detection electrodes and applying trapping potentials to the electrodes, whose width is decreasing in the direction toward the center of the cell and grounding others. In this configuration the averaged (by cell coaxial cyclotron motion) field distribution is hyperbolic in the whole volume. Very high resolution

was routinely achieved for peptides (25 000 000 on reserpine, 600 Da) and proteins (1 500 000 on BSA, 65 Da, 500 000 on IgG and ADH 150 000 Da, see the spectrum) on moderate field magnet (7Tesla). Resolution values are pressure limited. The cell permits working with cyclotron radius of up to 80% of cell radius. Experimental comparison with Bruker "infinity" cell and an open cell with 6 compensation electrodes [16] have shown the advantage of the new cell over both of them in resolution, mass accuracy and sensitivity. The resolution achieved on peptides permits visualizing and analyzing the fine structure of isotopic clusters mass spectra and clearly demonstrates the possibility to resolve isotopic clusters of proteins with masses higher than 150 kDa and determine their masses and masses of modifications even on medium magnetic field intensity magnets. The new cell gives the record resolution on the small peptides as well. 25 million resolution was obtained for Reserpine. Such resolution permits seeing the fine structure of mass spec peaks and determining elemental composition of the peptide directly from a single mass spectrum.

Acknowledgements

This work was supported by the Russian Foundation for Basic Research through grants Nos. 09-03-92500-ИК_а, 09-04-00725-а 10-04-13306-РТ_оми, and the Russian Ministry of Education and Science contracts 14.740.11.0755, 16.740.11.0369.

References

1. J.L. Benesch, B.T. Ruotolo, D.A. Simmons, C.V. Robinson, *Chem. Rev.,* 2007, **107**(8), 3544-67.
2. C.V. Robinson, A. Sali, W. Baumeister, *Nature*, 2007, **450**, 973-82.
3. J.L. Benesch, *J. Am. Soc. Mass Spectrom.*, 2009, **20**, 341-8.
4. M. Sharon, *J. Am. Soc. Mass Spectrom.*, 2010, **21**, 487-500.
5. E. van Duijn, *J. Am. Soc. Mass Spectrom.*, 2010, **21**, 971-8.
6. C.W. Uetrecht, N.R. Versluis, W.H. Roos, G.J.L. Wuite, P.T. Wingfield, A.C. Steven, A.J.R. Heck, *Proc. Natl. Acad. Sci. U.S.A.*, 2008, **105**, 9216-9220.
7. N. Felitsyn, E.N. Kitova, J.S. Klassen, *Anal. Chem.*, 2001, **73**, 4647-61.
8. R.B. Geels, S.M. van der Vies, A.J. Heck, R.M. Heeren, *Anal. Chem.*, 2006, **78**, 7191-6.
9. A. El-Faramawy, Y. Guo, U. Verkerk, B.A. Thomson, M. Siu, "Evaluation of IR Multiphoton Dissociation as a Method for High Mass Protein Clean Up", *56th ASMS Conference on Mass Spectrometry*, Denver, Colorado 2008.
10. C.M. Jones, R.L. Beardsley, A.S. Galhena, S. Dagan, G. Cheng, V.H. Wysocki, *J. Am. Chem. Soc.*, 2006, **128**, 15044-5.
11. J.L. Benesch, B.T. Ruotolo, F. Sobott, J. Wildgoose, A. Gilbert, R. Bateman, C.V. Robinson, *Anal. Chem.*, 2009, **81**, 1270-4.
12. R.A. Zubarev, N.L. Kelleher, F.W. McLafferty, *J. Am. Chem. Soc.*, 1998, **120**, 3265-6.
13. X. Han, M. Jin, K. Breuker, F.W. McLafferty, *Science*, 2006, **314**, 109-12.
14. I.A. Boldin, E.N. Nikolaev, *RCMS*, 2011, **25**, 1-5.
15. E.N. Nikolaev, I.A. Boldin, R. Jertz, and G. Baykut, *JASMS*, 2010-4720R1.
16. Tolmachev et al., *JASMS*, 2008, **19**, 586-597.

Invited

ASPECTS OF MODELLING ANTIBODY AFFINITY MATURATION: WHAT DATA ARE WE STILL MISSING?

M. Or-Guil[1], **N. Wittenbrink**[1], and **J. Faro**[2]

[1] Humboldt University Berlin and Research Center ImmunoSciences, Charité, Berlin, Germany
m.orguil@biologie.hu-berlin.de
[2] Department of Biochemistry, Genetics and Immunology, University of Vigo, Vigo Spain and Instituto Gulbenkian de Ciência, Oeiras, Portugal, jfaro@uvigo.es

Central to the humoral immune response is the micro-evolutionary process of B cell affinity maturation that leads to a substantial increase of antibody affinity. Affinity maturation takes place in dynamic microstructures called germinal centres that form during T cell dependent immune responses. There, B cells undergo rapid proliferation, somatic hypermutation, and selection of cells bearing higher affinity B cell receptors. However, the mechanisms linking these processes are poorly understood. To assemble this puzzle, several key pieces of information are needed. Among them are the numbers of participating B cells and the numbers of participating B cell clones during the kinetics of an acute immune response. Since long, mathematical models have been used as a tool to interpret experimental observations, but it is arguable that presently available experimental observations on germinal centers are sufficient to infer mechanisms even using mathematical models. Clonal diversity cannot be observed directly, and because of that, earlier studies resorted to interpreting two types of available experimental data: immunohistology of germinal centers containing two phenotypically distinct B cell populations, and antibody gene sequences of small B cell samples from germinal centers. Based on a simple model, investigators concluded that a typical germinal center was seeded by 2–8 B cells, endorsing the current notion that germinal centers are oligoclonal from the onset [1]. Faro and Or-Guil, however, showed that the underlying model is not statistically consistent with the original data, concluding that germinal centers most likely contain broadly varying numbers of different B cell clones, averaging 5 to 10-fold more clones than previously estimated [2].

Likewise, also the kinetics of B cell populations in individual germinal centers cannot be observed directly. Germinal centers are formed at the onset of an immune response and diminish in size as the immune response recedes, and there have been many attempts to uncover mechanisms of B cell proliferation, death, and selection from the kinetics of numbers of B cells within single germinal centers. These kinetics were mostly determined from the average size of germinal center cross-sections taken from large numbers of germinal centers in lymphatic tissues. However, as illustrated in Figure 1, simulations of germinal center B cell population size kinetics show that very different individual kinetics can lead to the same cross-section size distribution and that this measure is hence not sufficient to draw any conclusions on individual germinal center kinetics, as was shown in [3]. Moreover, also analysis of the actual volume distribution kinetics leads ambiguous results [4].

With that, we find that some of the crucial measures that could help unveil mechanisms of germinal center reactions are assessed experimentally in a way that will not lead to conclusive results on that measures. We argue that some of the challenges posed on germinal center modelling and generation of experimental data are being left undiscussed, a deficit that needs to be overcome to unveil the protein evolution aspects of affinity maturation.

Particularly:

- Experimental data to quantify clonal size distributions would need to comprise a large number of antibody gene sequences from a large number of individual germinal centers, as well as a much more refined immunohistological or live imaging data on numbers and fate of phenotypically distinct populations.
- Experimental data to quantify B cell population size kinetics would need to comprise observations of germinal center sizes for a large number of individual germinal centers during a time scale of days.

Only the combination of both type of imaging experiments – germinal center size kinetics in the time scale of days and measurement of the fractions of phenotypically distinct B cell populations – will allow assessing possible correlations between germinal center sizes and clonal diversity. This measure might be crucial for understanding micro-evolutionary processes with the help of

mathematical models, since stringency of selection (and hence the number of clones) most probably has an impact on B cell population size, as has already been postulated [5].

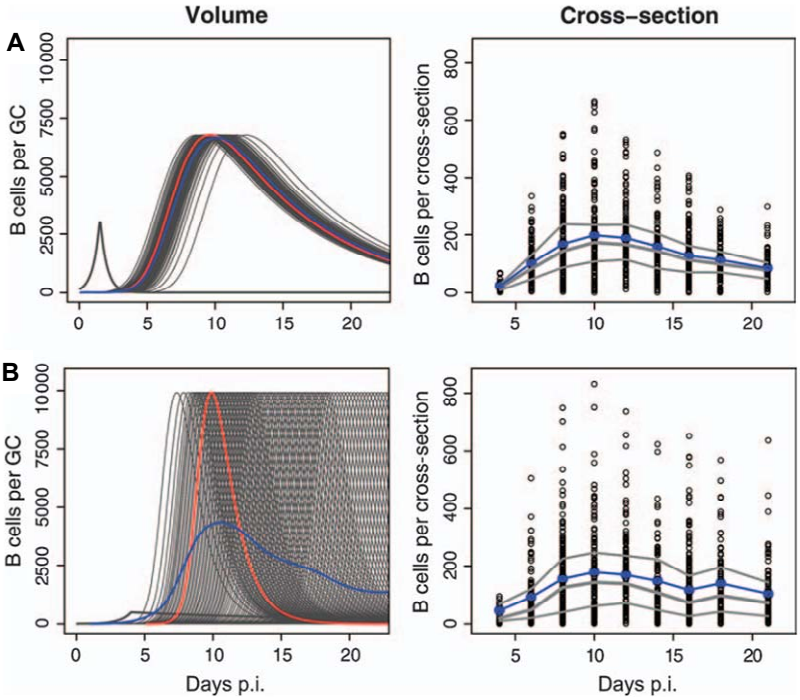

Fig. 1. Simulated random sectioning of germinal center ensemble kinetics

Left: Kinetics of ensembles of many individual germinal centers (gray curves), depicted in numbers of B cells representing germinal center volumes. The seeding densities follow a cusp-like shape (dark gray curve, arbitrary units). Only every 10th individual germinal center is shown, and one of the individual kinetics is highlighted (red curve). The average number of B cells is shown by a blue curve.
Right: Simulated cross-sectional areas of the respective ensembles, assuming that germinal centers are distributed randomly in the spleen, have the shape of ellipsoids (diameter ratios 4:1:1) and are sectioned by a plane cut. The ellipsoids are sectioned according to their individual probability of being cut at all, which depends on their size.
Blue circles and curves: mean size of cross-sectional germinal centers, expressed in numbers of B cells. Gray curves: median lower and upper quartiles of the simulated cross-sectional germinal center size distributions (open circles).
Rows A and B each display combinations of different individual germinal center kinetics and densities of germinal center seeding events. (A) Long-lived germinal centers and nearly synchronous ensemble kinetics. The maximum seeding rate is reached within 1.5 days and decays rapidly within half a day. (B) Short-lived germinal center kinetics: the seeding rate increases for 4 days and decays only slowly afterward, implementing an ongoing series of germinal center seeding events (figure adapted from [3]).

Acknowledgements

This research was supported by grant 0315005B (Bundesministerium für Bildung und Forschung, Germany) (MOG, NW) and by grants SAF2007-63152 (MICINN, Spain) and PIRSES-GA-2008-230665 (7th FP, EC) (JF).

References

1. M.H. Hermans et al., *J. Exp. Med.*, 1992, **175**, 1255-1269.
2. J. Faro and M. Or-Guil, *Mathematical Models in Immune Cell Biology,* G. Lythe, and C. Molina-París (Eds.), Springer Press, 2011, 424.
3. M. Or-Guil, N. Wittenbrink, A.A. Weiser, and J. Schuchhardt, *Immunol Rev.*, 2007, **216**, 130-141.
4. N. Wittenbrink, T.S. Weber, A. Klein, A.A. Weiser, W. Zuschratter, M. Sibila, J. Schuchhardt, and M. Or-Guil, *J Immunol.*, 2010, **184**(3), 1339-1347.
5. S.H. Kleinstein and J.P. Singh, *J. Theor. Biol.*, 2001, **211**, 253-275.

SILICON NANOCRYSTALS AS PHOTO- AND SONOSENSITIZERS FOR BIOMEDICAL APPLICATIONS

L.A. Osminkina[1], **M.B. Gongalsky**[1], **R.A. Galkin**[1], **S.N. Shevchenko**[1], **R.S. Fadeev**[2], **A.A. Kudryavtsev**[2], and **V.Yu. Timoshenko**[1]

[1]Moscow State M.V. Lomonosov University, Physics Department, Russia, osminkina@vega.phys.msu.ru
[2] Institute of Theoretical and Experimental Biophysics, Russian Academy of Science, Pushino Moscow region, Russia

Silicon (Si) has a dominant role in electronics industry, but in fact it can also play important roles in biomedicine. For example, the biocompatibility and biodegradability of Si nanocrystals (nc-Si) and porous nanoparticles were demonstrated [1-3]. In particular, biodegradable nanoparticles of luminescent porous Si were proposed for the medical diagnostics [1]. Also *in vivo* experiments showed the biocompatibility of thermally oxidized porous Si films with the eye tissues, that can be used to improve existing therapies in patients with dysfunction of the corneal epithelial cells and ocular surface diseases [2]. Note that the total content of Si in the body of a healthy 70 kg adult is ~1 g, making Si the most important trace mineral in human body [3]. Recently it was demonstrated that nc-Si assemblies act as an efficient photosensitizer of singlet oxygen (SO) [4], which can be used for the photodynamic therapy (PDT) of cancer [5]. Another efficient method of the cancer therapy is based on application of high-intensity focused ultrasound irradiation (USI) (see for example Ref. [6]). The ultrasound therapy efficiency is limited by low selectivity of USI, which is required to achieve the therapeutic effect. In the present work we have examined nc-Si-based samples for applications as photo- and sonosensitizers in cancer cell destruction *in vitro*.

Samples of nc-Si were fabricated by dry or wet high-energy milling of crystalline Si wafers (nc-cSi) or porous silicon (nc-mesoPSi, nc-microPSi) films. Porous silicon films were formed by the standard method of electrochemical bulk silicon (c-Si) etching of c-Si wafers with specific resistivity of 25 mΩ•cm (for nc-mesoPSi) and 10 Ω•cm (for nc-microPSi).

According to the TEM data, the obtained samples consisted of grains with average sizes from 50 to 200 nm. The nc-mesoPSi and nc-microPSi samples are probably composed of agglomerates of smaller nc-Si with size near 2÷20 nm (Fig. 1 a, b, c).

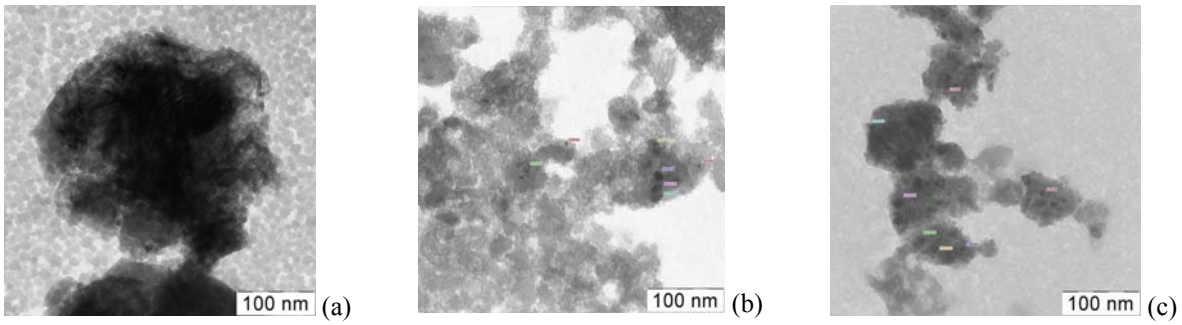

Fig. 1. TEM images of the investigated samples of silicon nanocrystals: nc-cSi (a), nc-mesoPSi (b), and nc-microPSi (c)

Typical PL spectra of prepared samples are shown in Fig. 2. Note that the nc-cSi did not demonstrate remarkable PL intensity (Fig. 2, curve 1), because it is composed by rather large c-Si grains. The PL spectra of nc-mesoPSi (curve 2) and nc-microPSi (curve 3) are represented by broad bands centered near 1.3 eV and 1.7 eV, respectively. These PL spectra can be interpreted as the radiative recombination of excitons confined in nc-Si with sizes distributed from 3 to 6 nm [7]. The PL peak position depends on the nc-Si size. The PL intensity of nc-mesoPSi is smaller than that of nc-microPSi because of larger sizes of nc-Si and more efficient non-radiative recombination processes.

It was found that after saturation of nc-microPSi suspensions with oxygen the PL quenching occurred and its degree increased monotonically with the concentration of O_2. After the removal of dissolved gas, the PL intensity nearly returned to the initial level. It was shown that the maximum suppression of the PL of nc-Si occurs near 1.6 eV, which is close to the energy of the $^3\Sigma \rightarrow {}^1\Sigma$ transition in O_2. This fact indicates that the quenching of PL of nc-Si occurs due to the SO photosensitisation.

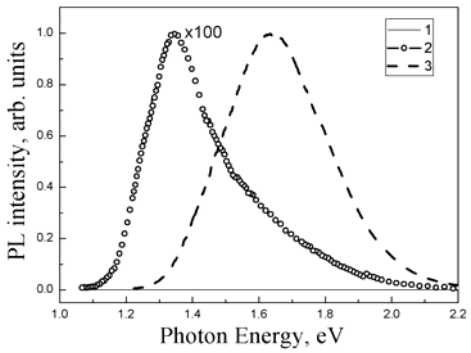

Fig. 2. Photoluminescence spectra of nc-cSi (a), nc-mesoPSi (b), and nc-microPSi (c)

In-vitro experiments demonstrated that the SO photosensitized by nc-Si dispersed in aqueous solution could suppress the proliferation of cancer cells (mouse fibroblasts 3T3 NIH). It was shown that the number of living cells after irradiation in the growth medium with added nc-Si (~0.5 g/l) decreased strongly as compared to the reference group. The DNA analysis of the cancer cells affected by nc-Si provided evidences of the apoptosis mechanism of their death. We found that photoluminescent nc-Si could penetrate into cancer cells and so they were used for bioimaging experiments.

It was found that simultaneous action of nc-Si (~1 g/l) and USI (~5 W/cm^2) could result in almost complete destruction of cancer cells (3T3 NIH and Hep 2). At the same time in the reference group (without nc-Si) the number of cells remained practically unchanged after the same USI (Fig. 3).

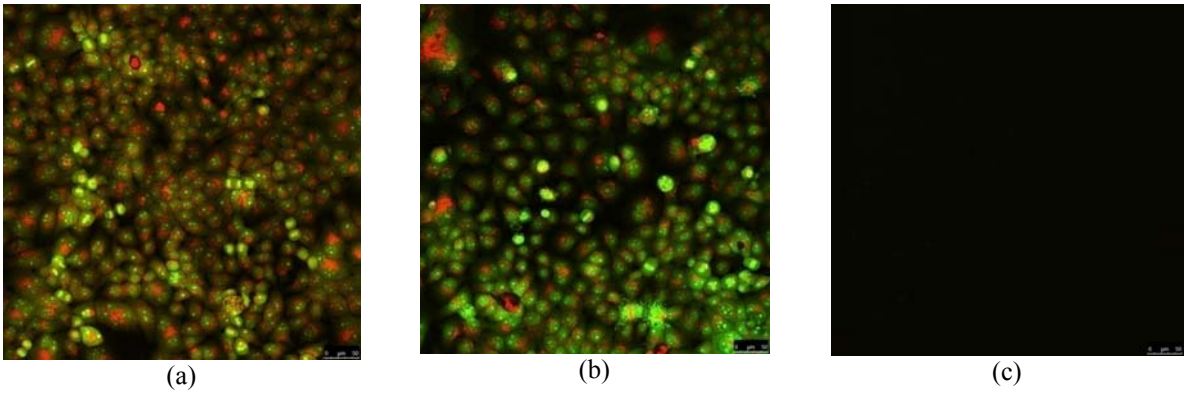

(a) (b) (c)

Fig. 3. Confocal microscopy images of the reference cancer cells (a), cancer cells culture after USI (5 W/cm^2), and that after simultaneous action of nc-mesoPSi (~1 g/l) and USI (~5 W/cm^2)

According to the confocal microscopic measurements no living cells were found on the surface of culture cup and in the culture medium after the USI-treatment with 5 W/cm^2 intensity in the presence of nc-mesoPSi (see Fig.3 c). This effect was stronger for nc-mesoPSi than for nc-cSi. It can be explained by larger surface area of nc-mesoPSi, which promotes the USI-induced heating and cavitations. The USI-treatment with the low intensity 0.5 W/cm^2 did not destroy the cells instantly, but they lost their proliferation properties and died within 20-80 h after USI. This observation demonstrates perspectives of nc-Si as sonosensitizers for improving efficiency of the ultrasound therapy of cancer.

Acknowledgement

We acknowledge S.S. Abramchuk for the TEM measurements. The samples of nc-Si were fabricated using the equipment of the Center of User Facilities of M.V. Lomonosov Moscow State University.

References

1. J. Park, L. Gu, G.V. Maltzahn, E. Ruoslahti, S.N. Bhatia, and M. Sailor, *Nature Materials*, 2009, **8**, 331.
2. S.P. Low, N.H. Voelcker, L.T. Canham, and KA. Williams, *Biomaterials*, 2009, **30**, 2873.
3. L.T. Canham, *Nanotechnology*, 2007, **18**, 185704.
4. D. Kovalev, E. Gross, N. Künzner, F. Koch, V.Yu. Timoshenko, M. Fujii, *Phys. Rev. Lett.*, 2002, **89**, 137401.
5. V.Yu. Timoshenko, A.A. Kudryavtsev, L.A. Osminkina, A.S. Vorontsov, Yu.V. Ryabchikov, I.A. Belogorokhov, D. Kovalev and P.K. Kashkarov, *JETP Lett.*, 2006, **83**(9), 423.
6. E.J. Halpern, *Radiology*, 2005, **235**, 345.
7. D. Kovalev, H. Heckler, G. Polisski, F. Koch, *Phys. Stat. Sol.*, 1999, (b) **215**, 871.

FEATURES OF INTERACTION OF NANODIAMOND-BIOMOLECULE CONJUGATES WITH TARGET SYSTEMS

E. Perevedentseva[1,2], **A. Karmenyan**[3], **C.Y. Lee**[1], **T.H. Su**[1], **Y.C. Lin**[2], and **C.L. Cheng**[1]

[1] Physics Dept., National Dong Hwa University, Hualien, Taiwan
elena@mail.ndhu.edu.tw; clcheng@mail.ndhu.edu.tw
[2] P.N.Lebedev Physics Institute of Rus. Acad. Sci., Moscow, Russia
[3] Institute of Biophotonics Engineering, National Yang-Ming University, Taipei, Taiwan, artashes@ym.edu.tw

Nanodiamond particles (ND) are recently considered as promising nanostructures for biotechnological and biomedical applications, like bio-imaging, bio-sensing, drug delivery, etc [1]. For these applications, ND surface is functionalized with bio-molecules providing the interaction with target bio-object or for therapeutic effects. The interaction of ND-biomolecule conjugate with cells or tissues is determined by the properties both of nanoparticles and the biomolecule, which can be modified at the conjugation.

To analyze the ability of ND to serve the base for attachment of biomolecule of interest the interaction of ND-medicine complex with the bacteria and cells is compared with that of pure medicine and ND separately were studied. The interaction of bacteria E. coli with enzyme lysozyme and ND-lysozyme complex has been observed in [2]. It has been shown [2, 3], that lysozyme adsorbed on ND with average particles size 100 nm kept its antibacterial activity. ND-lysozyme complex destroys the bacteria cell wall and the number of bacteria in culture treated with ND-lysozyme decreases significantly in the comparison with control. The effect of ND of different sizes on structural properties of the lysozyme and on its activity is discussed in [3].

In [4] the interaction of membrane growth hormone receptor (GHR) of A549 human lung epithelial cells with growth hormone (GH) was observed using nanodiamond's spectroscopic signal via confocal Raman mapping. The GH (rEaGH) molecules were covalently conjugated carboxylated ND with average size 100 nm, which have been recognized specifically by the GHR of A549 cell. The Raman spectroscopic signal of ND (1332 cm^{-1}) provides direct observation of interaction between GH and GHR in physiological condition in a single cell level. In [5] the preserved anticancer activity of covalently conjugated with detonation ND (with size 3-5 nm) anticancer drug paclitaxel is demonstrated via the conjugate interaction with cancer A549 cell and the induction of mitotic blockage, apoptosis and anti-tumorigenesis.

Thus, conjugated molecules can keep their functionality that allows development of novel methods of bio-probing and drug delivery using ND. Owned so the understanding of the processes of ND-biomolecule conjugate interaction with target cell or tissue is necessary for using all ND advantages in the bioapplications. In this work penetration of drug-ND complex inside the cells in comparison with penetration of pure drug and with nanodiamond penetration was analyzed using plant alkaloid berberine. Berberine has demonstrated significant antimicrobial activity against a variety of bacterial and parasite infections. On the other hand, due to its spectroscopic properties berberine can be used like natural fluorescence dye. It has allowed the comparison of distribution of berberine and nanodiamond signals at interaction of berberine-nanodiamond complex with cells.

To study the properties of berberine-ND conjugate, berberine was diluted in bi-distilled water in concentration 2 mg/ml and adsorbed on the 100 carboxylated ND (cND) (added to the berberine solution in concentration 20 mg/ml). The adsorption was estimated via UV-visible spectra of berberine solution before and after it's interaction with cND, and confirmed via photoluminescence (Figure 1) and Raman spectra of berberine-cND complex.

Interaction of berberine-cND complex (in concentration 20 μg/ml) with Baby Hamster Kidney cancer cell (BHK) was studied using Leica confocal laser-scanning microscope (TCS SP5, Mannheim, Germany) and compared with the berberine solved in the cell medium (in concentration 20 μM). The localization of berberine-ND complex on the BHK cell membrane (Figure 2) against to penetration of the berberine molecules into the cell cytoplasm is observed at short times of joint incubation (within 2 hrs). The berberine-cND complex penetration inside the BHK cell and localization in cytoplasm was observed at 4-24 hrs of joint incubation, like for cND, while molecular berberine is observed localized in the cell nuclei after 8-24 hrs of joint incubation.

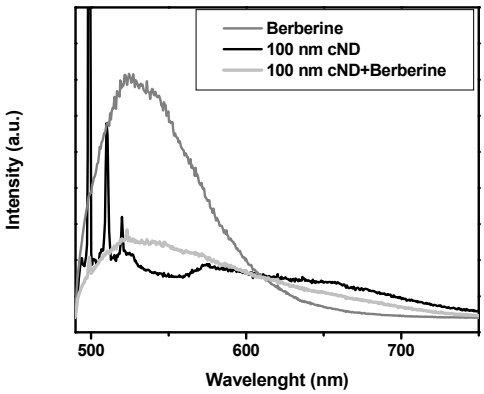

Fig. 1. Fluorescence spectra of berberine, 100 nm cND and cND-berberine at excitation 488 nm measured with Witec α-SNOM spectrometer, Germany

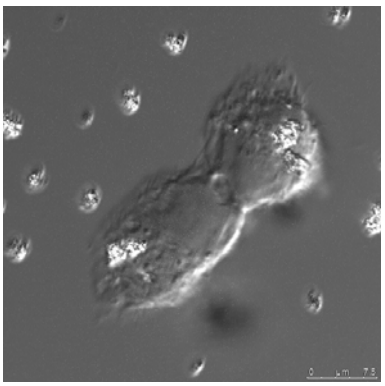

Fig. 2. The image of BHK cells after 2 hrs incubation with 100 cND-berberine conjugate. The berberine fluorescence was excited with 405 nm and signal was collected in range 470-591 nm; ND fluorescence was excited with 633 nm and signal was collected in range 644-713 nm; measured with Leica confocal laser-scanning microscope (TCS SP5, Mannheim, Germany)

The knowledge of the characteristics of the penetration of material in different form (molecular, connected to nanoparticle, etc.) into target cells and tissues and opens new possibilities for controlled drug delivery, bio-labeling and bio-sensing, however requires the understanding the mechanisms of interaction between the material and ND, as well as between the material with target object and between ND-conjugate with target object.

Acknowledgements

The authors appreciate the National Science Council of Taiwan for financially supporting this project under Grant No. NSC-98-2120-M-259-001, and a joint Taiwan-Spain Research Cooperation project (Grant No. NSC99-2923-E-010-001-MY3).

References

1. J.-I. Chao, E. Perevedentseva, P.-H. Chung, K.-K. Liu, C.-Y. Cheng, C.-C. Chang, and C.-L. Cheng, *Biophys. J.*, 2007, **93**, 2199–2208.
2. E. Perevedentseva, C.-Y. Cheng, P.-H. Chung, J.-S. Tu, Y.-H. Hsieh, and C.-L. Cheng, *Nanotecnology*, 2007, **18**, 315102.
3. E. Perevedentseva, P.-J. Cai, Y.-C. Chiu, and C.-L. Cheng, *Langmuir*, 2011, **27**, 1085.
4. C.-Y. Cheng, E. Perevedentseva, J.-S. Tu, P.-H. Chung, C.-L. Cheng, K.-K. Liu, J.-I Chao, P.-H. Chen, and C.-C. Chang, *Appl. Phys. Lett.*, 2007, **90**, 163903.
5. K.-K. Liu, W.-W. Zheng, C.-C.Wang, Y.-C. Chiu, C.-L. Cheng, Y.-S. Lo, C. Chen, and J.-I. Chao, *Nanotechnology*, 2010, **21**, 315106.

Invited

LASER-ACTIVATED HYBRID MATERIALS LOADED WITH PLASMONIC NANOPARTICLES FOR TISSUE REPAIR

R. Pini[1], P. Matteini[1], F. Ratto[1], F. Rossi[1], S. Centi[2], and **L. Dei[3]**

[1] Institute of Applied Physics, Florence, Italy, r.pini@ifac.cnr.it
[2] Dept. of Clinical Physiopathology, University of Florence, Italy
[3] Dept. of Department of Chemistry and CSGI Consortium, University of Florence, Italy

Introduction

Laser welding of biological tissues is emerging as a valid alternative to conventional suturing techniques in applications where portions of tissues have to be sealed together [1]. It exploits the interaction of light from a laser source with an optical absorber, such as the body water, to convert the laser light into heat. Heating of tissue induces thermal modifications in the main tissue components such as the fibrillar collagen of the extracellular matrix, which results in the formation of new bonds between apposed flaps. Advantages of laser welding over conventional surgical procedures include immediate watertight closure of the wound, reduced operation times, minimal inflammatory response and scar formation, faster healing times, increased ability to induced regeneration of the original tissue architecture and an improved cosmetic appearance.

A main challenge frequently encountered in laser welding operations is the control over the heat dosimetry, which is crucial to trigger a suitable welding effect without detrimental overheating effects to the surrounding tissue. In this context, improved results were achieved by using photoenhancing dyes, acting as exogenous optical absorbers, which enable the fusion of wounds at lower irradiation fluencies, thus reducing the risk of collateral thermal damage. In fact the use of a chromophore was found to induce a controllable temperature rise only in the area where it had been applied, resulting in a selective thermal effect. These concepts have been developed over the last ten years at the Institute of Applied Physics and finally allowed to promote the laser welding technique to the clinical practice for the closure of corneal wounds in corneal transplant surgery. Here, the surgical technique is based on the combination of a near infrared laser radiation produced by a near-infrared diode laser (810 nm), which penetrates deep into the body, with an exogenous chromophore such as Indocyanine Green (ICG) topically applied at the site to be repaired. Laser light can be delivered continuously or in pulses, in accordance with the treatment to be performed, including penetrating, lamellar and endothelial corneal transplants. Moreover, similar procedures are now offering the possibility to perform different kinds of operations, which are typically challenging with traditional methods. These include the anastomosis of small vessels and the implantation of a neurosurgical bypass, which need for a rapid and minimally invasive surgical procedure in order to limit the risk of thrombosis and occlusion at the anastomotic site. A preclinical validation of laser-assisted vascular welding has been performed during the last decade by our group in different animal models.

Gold nanochromophores

Despite the experimental and clinical achievements obtained in the last years, some critical aspects still limit a larger diffusion of the laser welding technique. The main limitations have to be ascribed to the use of organic chromophores, such as their poor photochemical stability, excessive diffusiveness in the biological matrices and inadequate stability when stored in an aqueous solution or dispersed in a physiological environment. Recent proposals to optimize laser tissue bonding involve the development of new nanochromophores, such as ICG molecules loaded into silica nanoparticles [2], as well as metal nanoscale transducers. Regarding the latter technology, gold nanoparticles exhibit strong plasmonic resonances, which may provide high efficiency and localization of heat release. In particular gold nanorods (GNRs) appear as an ideal candidate to replace the exogenous chromophores in use due to their extreme optical absorbance, excellent biochemical versatility and stability under physiological conditions as well as high laser irradiance [3, 4]. GNRs feature a cylindrical shape and localized plasmon resonances at frequencies in the NIR window, which can be tuned by modulation of their size and shape. Upon excitation with radiation from a NIR laser, these plasmon resonances undergo excitation and relaxation through radiative and non radiative channels. These dynamics give rise to a wealth of functionalities such as e.g. a very strong photothermal and photoacoustic

transduction, scattering, luminescence and enhancement of the near field. Therefore these gold nanoparticles may become valuable contrast agents in a variety of diagnostic and therapeutic applications (e.g. optical and photoacoustic imaging, flow cytometry, welding, hyperthermia, photoporation, photoacoustic microsurgery, etc.).

Laser welding with gold nanochromophores

Recently our research group demonstrated the successful application of an aqueous suspension of GNRs for the direct welding of explanted lens capsular tissues [5]. Later substantial advancements have been obtained upon inclusion of gold nanorods into polysaccharide scaffolds. In these systems the sugar chains enwrap the nanoparticles, thus creating a protective barrier against the physiological environment and enhancing their stability, durability, effectiveness and biocompatibility. Preliminary investigations consisted of in vivo laser closuring of full thickness incisions performed in the carotid artery wall by means of a NIR radiation in conjunction with the topical application of a composite gel of hyaluronan and gold nanorods. Irradiation of the wounds with a continuous intensity of 40 W/cm^2 provided successful closure of their edges with sufficient strength to sustain blood pressure and ideal healing within a 30 days follow-up.

A further optimization of tissue repair procedures with gold nanochromophores consisted of the use of flexible materials with enhanced handiness and stability. In this regard, our group has recently developed a smart hybrid material consisting of biocompatible chitosan films doped with GNRs, which can be activated by diode laser radiation at 810 nm and precisely bind biological matter, like a light-activated plaster for tissue repair and wound dressing [6]. Effective and reproducible adhesion of these films onto explanted carotid artery samples was achieved by means of contiguous spots of laser irradiation realized by gently bringing an optical fiber tip into contact with the films and delivering 810 nm diode laser pulses of 100 ms duration and 100 mJ energy, corresponding to 140 J cm^{-2} fluence at the outermost film surface. Here the gold nanoparticles enable selective and localized conversion of light into heat. In turn, temperature induces the activation of the polar chitosan strands, which become available to bind adjacent biological matter, ultimately resulting in a functional adhesion effect. The chitosan matrix imparts excellent stabilization and distribution of the particles, which translates into a dependable optical response and photothermal conversion. These films are resistant, pliable and stable under physiological conditions and dissolve in the body within several weeks. In addition, chitosan is a natural biopolymer that stimulates tissue regeneration, exerts antimicrobial activity and may be used to host and release drugs.

The present results are encouraging toward the development of a novel technology based on the introduction of bio-inspired nanoplasmonic materials into photothermal applications including laser-induced tissue repair and temperature-controlled drug release.

Acknowledgements

This work has been partially supported by the Projects of the Health Board of the Tuscany Region "NANO TREAT" and "NANO-CHROM" and by the Network of Excellence "Photonics 4 Life".

References

1. R. Pini, F. Rossi, P. Matteini, F. Ratto, *Biophotonics. Series: Biological and Medical Physics, Biomedical Engineering*, Springer, Berlin, 2008, p. 275.
2. D.S. Schoni, S. Bogni, A. Bregy, A. Wirth, A. Raabe, I. Vajtai, U. Pieles, M. Reinert, M. Frenz, 2011 submitted.
3. X. Huang, S. Neretina, and M.A. El-Sayed, *Adv. Mater.*, 2009, **42**, 4880-4910.
4. P.K. Jain, X. Huang, I.H. El-Sayed, and M.A. El-Sayed, *Acc. Chem. Res.*, 2008, **41**, 1578-1586.
5. F. Ratto, P. Matteini, S. Centi, F. Rossi, R. Pini, *J. Biophotonics,* 2010, **4,** 64-73.
6. P. Matteini, F. Ratto, F. Rossi, S. Centi, L. Dei, and R. Pini, *Adv. Mater.*, 2010, **22**, 4313-4316.

Invited

COMPLEX LASER-OPTIC STUDY OF THE INTERACTIONS OF NANODIAMOND PARTICLES WITH BLOOD COMPONENTS AT *IN VITRO* MEASUREMENTS

A.V. Priezzhev[1], A.E. Lugovtsov[1], V.G. Ionova[2], Yu.S. Samsonova[1], C.L. Cheng[3], and **E. Perevedentseva[3]**

[1] Physics Department and International Laser Center, M.V. Lomonosov Moscow State University Moscow, Russia; avp2@mail.ru
[2] Research Institute of Neurology of RAMN, Moscow, Russia
[3] Physics Department, National Dong Hwa University, Hualien, Taiwan

The role of laser-optical methods in investigating biological objects at various levels of organization is constantly increasing [1]. With the rapid development of nanotechnologies these methods are widely used for solving the problems of nanobiophotonics, particularly, for studying the interaction of biologically important molecules and cells with various nanoparticles that can get into the living (human) organism accidentally or intentionally.

Nanodiamond particles (NDs) are perspective fluorescent markers that can potentially be used for biomedical diagnostics. Although they seem to be not toxic and not to destroy vitally important organs, tissues and cells as was shown in a number of biological experiments both *in vitro* and *in vivo*, their implementation into clinical experiments is highly debated nowadays. There are fears about small ND particle penetration and accumulation into other cells than those tested. In general, the issues of biocompatibility of nanoparticles, nanotoxicity and nanosafety are gaining more and more attention nowadays.

The aim of our work was to explore the interactions of NDs with blood components and to study the effect of NDs on blood microrheology, in particular, on the ability of red blood cells (RBCs) to deform in shear flow and to spontaneously aggregate. This was motivated by the fact that the administration of NDs and other nanoparticles into a live organism is usually performed intravenously, i.e. via blood vessels. However the effect of nanoparticles on blood and on its ability to normally flow though the vessels of different radii is but rarely accounted for. The only information available at this time concerning the interaction of nanoparticles with RBC is that the administration of carbon nanoparticles into blood leads to the lysis of RBCs [2], aggregation of platelets and that small NDs (around 5 μm-sized) penetrate though the membranes of RBCs and interact with the hemoglobin (Hb) molecules. The latter fact can potentially lead to the reduction of RBC deformability, which may further lead to the impairments of the blood flow through smaller vessels. Another possible way for the NDs to affect blood rheology is to associate with the blood plasma proteins.

Here we present our findings about the *in vitro* interaction of nanodiamonds (5 and 100 nm) with human RBCs and with blood plasma proteins albumin and γ-globulin that play a significant role in intercellular interactions. Measurements have been facilitated using Raman and absorption spectroscopies, laser scanning fluorescence spectroscopy, dynamic light scattering, static diffuse scattering and laser diffractometry (also known as ektacytometery).

In order to demonstrate the interactions of NDs with RBCs we obtained fluorescence and bright field optical images of NDs and RBCs incubated with NDs with sizes 5 and 100 nm at their interaction with RBCs. The ND fluorescence was excited with 488 nm and collected in the 491–539 nm range (in green). We also obtained Z-scans of 100 nm NDs interacting with RBC. The images correspond to different positions along Z-axis with step 1 μm. The ND fluorescence was excited with 543 nm and collected in range 562–659 nm (shown in green). The obtained images clearly indicate that NDs attach to the cell membrane of the RBC.

In order to study the effect of NDs on RBCs we have conducted *in vitro* measurements of the deformability index and several parameters of aggregation kinetics using the optical measurement techniques based on the detection of diffraction patterns from dilute suspensions of RBCs and diffuse reflection from a layer of whole blood. In our experiments, we used suspensions of NDs with sizes from 5 to 100 μm in bidistilled water of different concentrations, added to samples of freshly drawn human blood. The ND particles had either bare or corboxilated (cND) surfaces, the latter case resulting in improved biocompatibility of the particles.

We have shown the there is a certain negative effect of NDs and cNDs on both deformability and aggregation kinetics of RBCs in the in vitro experiments. The effect is concentration dependent. In

particular, smaller NDs and cNDs (around 5 μm characteristic size) in smaller concentrations (around 33 μg/ml) seem to decrease the time of formation of both linear and 3D RBC aggregates and enhance the amplitude of spontaneous RBC aggregation in whole blood, which are overall negative physiologic effects. Larger NDs and cNDs (around 100 and 200 μm characteristic size) as well as smaller ones in higher concentrations (around 330 μg/ml) lead to smaller negative effects which can be speculated as a result of small particles aggregation in concentrated suspensions and nonpenetration of relatively large ND particles and their aggregates into the RBCs through their membranes. Carboxilation of ND particle surface makes the negative effect of small cNDs less pronounced but does not totally abolish it.

The effect of ND particles on shear deformability of RBCs is negative as well: the RBC deformability index is reduced all through the range of shear stresses (from 3 to 60 Pa). However the reduction of the deformability index becomes evident at higher concentrations (around 100 μg/ml).

We studied the effect of mixing the ND and cND water suspensions with albumin and γ-globulin aqueous solutions and demonstrated the adsorption of the molecules on the ND and cND surfaces [3], which resulted in an increase of the particle hydrodynamic radii. The effect is concentration and pH dependent. Preliminary coating of ND particles with albumin molecules reduces but not totally abolishes the effect.

These results are indicative of the importance of thorough studies of the effect of nanoparticles on blood rheologic properties, given the particles are to be delivered to the targets via the blood flow.

Acknowledgements

The authors thank Russian Foundation for Basic Research and National Science Council of Taiwan for providing financial support for the joint research.

References

1. V.V. Tuchin, *Lasers and Fiber Optics in Biomedical Studies*, Fizmatlit, Moscow, 2010.
2. A.P. Puzyr, A.V. Baron, K.V. Purtov, E.V. Bortnikov, N.N Skobelev, O.A. Mogilnaya, and V.S. Bondar, *Diamond Relat. Mater.*, 2007, **16,** 2124.
3. E.V. Perevedentseva, F.Y. Su, T.H. Su, Y.C. Lin, C.L. Cheng, A.V. Karmenyan, A.V. Priezzhev, and A.E. Lugovtsov, *Quantum Electronics*, 2010, **40**(12), 1089-1093.

SUPER-RESOLUTION BY STRUCTURED ILLUMINATION MICROSCOPY, PRINCIPLE AND SET-UP WITH A NANO HOLE ARRAY

R. Riesenberg, P. Petruck and **R. Heintzmann**

Institute of Photonic Technology, Jena, Germany, rainer.riesenberg@ipht-jena.de

The principle of sub-diffraction optical microscopy is introduced. The image information is generated by a set of spatial sample spots or sample lines with a known nano-scale size and in dimensions below the diffraction limit of the detection lens. The images of such spots or lines are convoluted by the airy disc of the used lens and they are diffraction limited. But their positions can be reconstructed in nano-scale. The sample spots can be generated by the help of nano particles, by nano marker, by excitation of nano areas (excitation and nonlinear depletion for STED microscopy) or by interference spots. An idea for future investigations is to use photonic crystals and meta materials for illumination. In case of structured illumination microscopy (SIM) interference stripes or interference spots for illumination are used. An additionally scan is needed to get a complete microscopic image. Some other super-resolution techniques use a switching of the spots (PALM, STORM).

The set-up for using an illumination by stripes in structured illumination microscopy (SIM) is shown in fig. 1 (left).

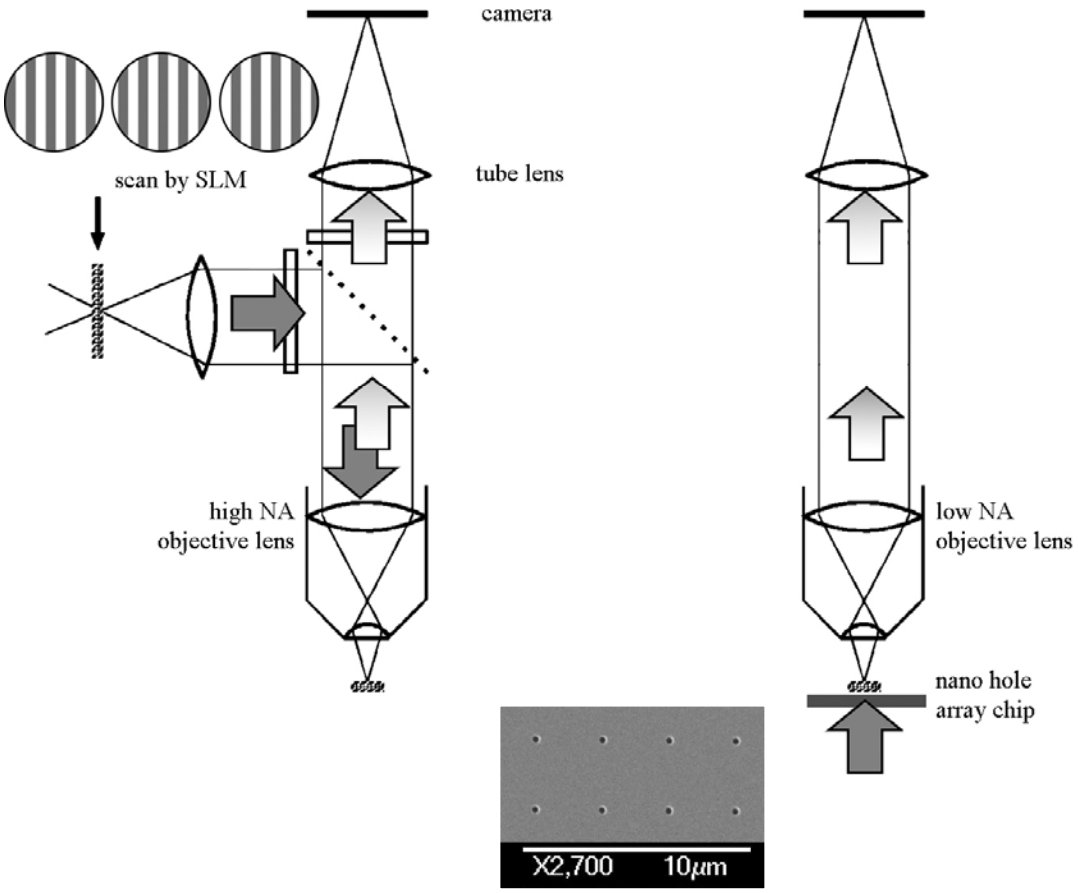

Fig. 1. *Left:* Known structured illumination microscope arrangement in reflection mode, typically an immersion lens (100 x, NA = 1.4) is used with a very limited field of view (diameter about 100 µm) and the illumination period is about 250 nm.
Right: The new version of SIM in transmission mode with a lens free high aperture structured illumination by a nano hole array (illumination spot size for example < 280 nm) and a separated imaging with a low resolution lens (10x / 0.2). Such low cost lenses usually have a large field of view (diameter 1000 … 2500 µm)

A new version of structured illumination microscopy is presented using illumination with interference spots generated by a periodic nano hole array. A sub-diffraction spatial resolution is achieved by a small interference spot size and a scan. The optical microscope set-up is completed by a common low resolution lens without any immersion which has a large field of view.

In our example, for illumination ($\lambda = 532$ nm) a planar nano hole array with hole diameters of 530 nm is used and a 30×30 scan was performed with 300 nm steps. The used low cost lens (10x / 0.2) has a spatial resolution (or ABBE limit) of 2.7 µm with plane wave illumination and 1.3 µm with Koehler illumination, respectively. Its field of view has a diameter of 2.3 mm. A reconstructed image example is given in fig. 2, right. The lateral resolution is about 800 nm. This is below the diffraction limit of the lens.

The combination of super-resolution and large field of view is possible by separating the illumination and the detection. A planar chip-based structured illumination acts as an illumination lens. The illumination contrast is very high, because it is generated by multi-beam interferences.

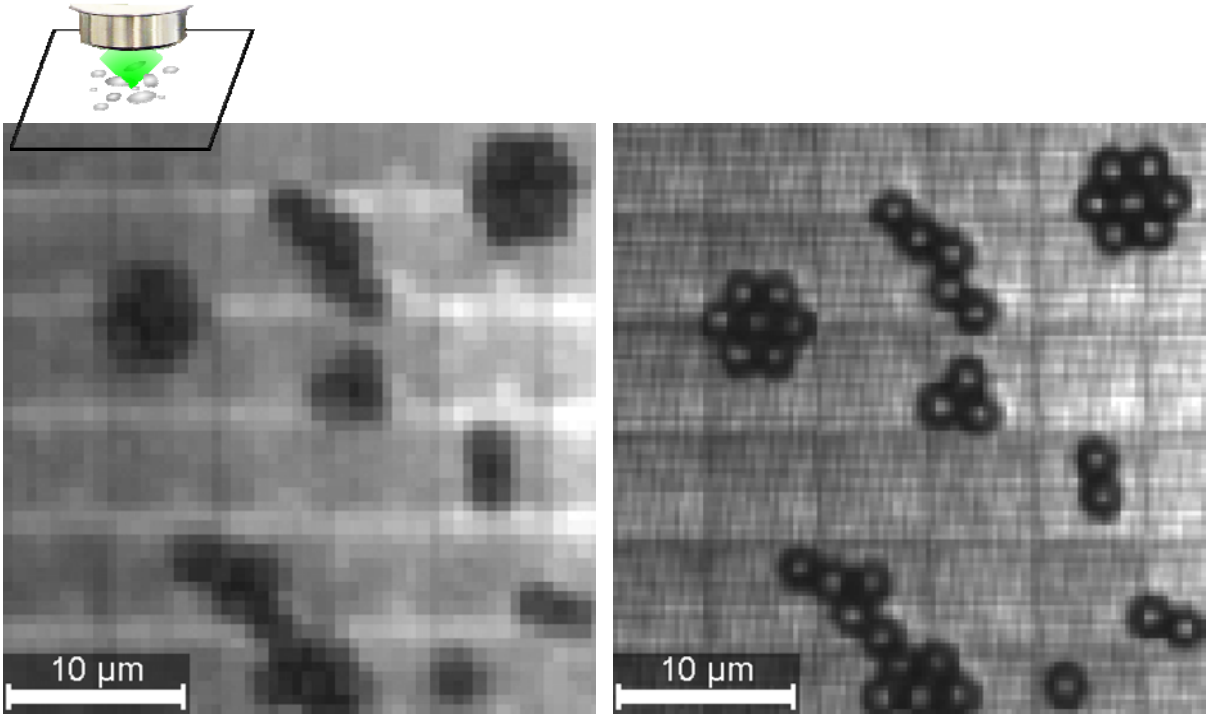

Fig. 2. Details of a microscopic image of 2 µm PMMA beads taken by an optical microscope with a common lens (10x / NA = 0.2). The same object is imaged twice by the same lens, common plane wave illumination (left) and illumination by a nano hole array and a scan (right). The resolution is more than three times better. The field of view still equals that of the 10x / 0.2 lens

Acknowledgements

We thank Mr. U. Hübner for preparing nano hole arrays, M. Kanka as well as J. Kreuzer, U Halifax, Ca, for helpful discussions and J. Popp for the support of the work.

References

1. R. Heintzmann, G. Mats, and L. Gustafsson, Nature Photonics, 2009, **3**, 362–364.
2. R. Riesenberg, P. Petruck, M. Kanka, and J. Bergmann, *Program and Abstract Book*, FOM 2010.
3. R. Riesenberg, P. Petruck, *Program and Abstract Book*, FOM 2011.
4. M. Kanka, A. Wuttig, C. Graulig, and R. Riesenberg, *Optics Letters*, 2010, **35**, 217–219.

CONFORMATIONAL EQUILIBRIUM IN pH-INDUCED FLUORESCENCE OF THE KINDLING FLUORESCENT PROTEIN

A.L. Rusanov[1], **V.A. Mironov**[2], **B.L. Grigorenko**[2], **A.V. Nemukhin**[2], and **A.P. Savitsky**[1]

[1] A.N. Bach Institute of Biochemistry, Russian Academy of Sciences, Moscow, Russian Federation
E-mail: alex_rusanov@inbi.ras.ru
[2] Department of Chemistry, M.V. Lomonosov Moscow State University, Russian Federation

Chromoproteins such as CP from the sea anemony Anemonia sulcata are characterized by peculiar spectral properties [1–3]. At low light intensities, the wild-type protein is weakly fluorescent with a very low quantum yield of $\varphi_{Fl} < 0.001$, which depends on the specific arrangement of amino acid residues in the chromophore environment. However, high intensity irradiation with green light leads to a nonlinear dependence of the fluorescence intensity on excitation energy [3] and a drastic increase of φ_{Fl}. This phenomenon, termed fluorescence "kindling", is reversible since upon blue light illumination or in the dark, the protein returns to its initial non-fluorescent state. The kindling properties of asCP can be optimized by the inclusion of the mutation Ala143Gly to produce the variant called KFP (kindling FP) [2].

The detailed mechanism of kindling still deserves characterization in spite of recent progress in studying reversible photoswitching of fluorescent proteins [2, 4–8]. The primary working hypothesis relates this phenomenon to the cis-trans isomerization of the chromophore inside the protein matrix [2, 5]. However, more evidence is needed to fully confirm this.

Analysis of pH dependence of the absorption and fluorescence spectra of KFP in aqueous solutions prompted us to assume that a shift in conformational equilibrium is responsible for substantial enhancement of red fluorescence in KFP at alkaline pH. Variations in pH also resulted in noticeable shifts in band maxima for absorption, fluorescence excitation and fluorescence emission. These observations can be interpreted as an appearance of pH-induced fluorescent conformational states of the protein.

Based on the available high-resolution crystal structures of KFP [6, 9] and other mutants of asCP [5] as well as on the results of molecular modeling we suggest that the population of protein conformations with modified protonation of the chromophore due to proton transfers from the nearby amino acid residues is affected by pH, and specify explicitly the chromophore sites that may be involved in these events. Possibly, appearance of these pH-induced fluorescent states is due to changes in the hydrogen bond network around the chromophore moiety, especially those associated with the side chains of Cys62 and Ser158. We hypothesize that conformational partitioning and fluctuations in protein ionization at alkali pH play an essential role in the appearance of KFP fluorescence.

Therefore, fluorescent conformations of the protein are formed at alkaline pH in the absence of intense green light illumination which is beyond the classical (photo-induced) mechanism of kindling. However, at alkaline pH the protein is already fluorescent without high-power green light illumination, and blue light does not eliminate all populations of fluorescent species.

These experimental findings prompt us to assume that pH conditions regulate conformational changes of the protein and its switching between non-fluorescent and several different fluorescent states. Interaction of the excited chromophore with surrounding amino acid residues results in the appearance of transient conformers similar to those observed at alkali pH.

Due to the complicated mixture of conformations in aqueous solution, it is hard to expect a simple mechanistic explanation of the observed pH dependences by analyzing hydrogen bond networks near the chromophore on the base of a single 3D structure of the protein as given by crystal X-ray data and molecular modeling. Apparently, we have to assume the existence of several distinct protein conformations fluctuating near the equilibrium state in solution, and this may be reflected by the well known fluctuation in protein ionization [10].

Acknowledgements

This work is supported by the Federal Agency of Science and Innovations of the Russian Federation state contract No. 02.740.11.0291 in the frame of the Program "Scientific, Academic and Teaching Staff of Innovative Russia, duration 2009-2013" and the Program of the Russian Academy of Sciences "Molecular and Cellular Biology".

References

1. K.A. Lukyanov, A.F. Fradkov, N.G. Gurskaya, M.V. Matz, Y.A. Labas, A.P. Savitsky, M.L. Markelov, A.G. Zaraisky, X. Zhao, Y. Fang, W. Tan, S.A. Lukyanov, *J. Biol. Chem*., 2000, **275**, 25879.
2. D.M. Chudakov, A.V. Feofanov, N.N. Mudrik, S.A. Lukyanov, K.A. Lukyanov, *J. Biol. Chem*., 2003, **278**, 7215.
3. T.A. Schüttrigkeit, T. von Feilitzsch, C. Kompa, K.A. Lukyanov, A.P. Savitsky, A.A. Voityuk, M.E. Michel-Beyerle, *Chem. Phys*., 2006, **323**, 149.
4. K.A. Lukyanov, D.M. Chudakov, S.A. Lukyanov, V.V. Verkhusha, *Nat. Rev. Mol. Cell. Biol*., 2005, **6**, 885.
5. M. Andresen, M.C. Wahl, A.C. Stiel, F. Gräter, L.V. Schäfer, S. Trowitzsch, G. Weber, C. Eggeling, H. Grubmüller, S.W. Hell, S. Jakobs, *Proc. Natl. Acad. Sci. U.S.A.*, 2005, **102**, 13070.
6. M.L. Quillin, D.M. Anstrom, X. Shu, S. O'Leary, K. Kallio, D.M. Chudakov, S.J. Remington, *Biochemistry*, 2005, **44**, 5774.
7. J.N. Henderson, H.-W. Ai, R.E. Campbell, S.J. Remington, *Proc. Natl. Acad. Sci. U.S.A.*, 2007, **104**, 6672.
8. K.M. Solntsev, O. Poizat, J. Dong, J. Rehault, Y. Lou, C. Burda, L.M. Tolbert, *J. Phys. Chem. B*, 2008, **112**, 2700.
9. P.G. Wilmann, J. Petersen, R.J. Devenish, M. Prescott, J. Rossjohn, *J. Biol. Chem*., 2005, **280**, 2401.
10. C. Tanford, *Phys. Chem. of Macromol.,* 1961, New York: John Wiley & Sons. p. 573.

Invited

PHOTOACTIVE GFP-TYPE FLUORESCENT PROTEINS IN REEF CORALS: BIOLOGICAL ROLES AND BIOIMAGING APPLICATIONS

A. Salih

Confocal Bio-Imaging Facility, School Natural Sciences, University of Western Sydney, Sydney, Australia
a.salih@uws.edu.au

Abstract

Fluorescent proteins (FPs) from the green fluorescent protein (GFP) family are indispensable *in vivo* bioimaging tools. In the last decade, a variety of multicolored FPs were discovered in marine organisms and they are particularly abundant and diverse in reef corals. Many FPs possess photoactive properties and their fluorescent color or intensity can change spontaneously after irradiation by specific wavelengths. These photoactivatable FPs (PAFPs) have become innovative tools for direct imaging and analysis of time dependent molecular events in live cells and organisms. Here, I describe biological studies of several PAFPs from Australian reef corals. They include the green to red photoconverters, as well as a novel type of PAFP that converts from red to yellow. Interestingly, a number of PAFPs localize in neuronal or photosensory cells. This discovery provides strong evidence for photofunctional significance of PAFPs. This research shows that by understanding the cellular localization patterns, we are able to elucidate the biological roles of PAFPs. By learning from nature, we will expand the arsenal of the applications of these proteins in advanced photonic applications.

Introduction

The world's coral reefs have spectacular natural colors and although it was once thought that GFP-type proteins are found only in bioluminescent jellyfish, it is now well known that non-bioluminescent corals possess the highest diversity [1]. Since the discovery of DsRed [2] over a 100 GFP-type proteins have been cloned from corals and related anthozoans. An important development for biophotonic sciences was the discovery of PAFPs, such as kindling, photoconverting and photoswitching proteins [3]. By converting a subset of PAFPs linked to target proteins, precise studies of biological processes can be done. Especially useful, is the use of PAFPs in the powerful technique of super-resolution imaging that relies on their property of reversible switching or photoconversion [4].

Despite the immense research focus on GFPs, their biological functions remain poorly understood. In corals, colors evolved under positive selection and must have important roles. Photoprotective function is now relatively well understood [5]. However, research of other proposed functions - electron transport, photosensing, as antioxidants, is only beginning. A surprising discovery was of a trans-protein proton pathway in wt-type GFP and a consequent proposal that GFPs may act as soluble light-driven proton pumps [6]. Together with the ground-breaking discovery that a variety of GFPs can act as light-induced electron donors [7], evidence is mounting that GFPs can function as light controlled modulators of cellular and organismal activity. There is now a real possibility for the development of a new generation of GFP-based optogenetic tools.

Methods

Corals from Great Barrier Reef and Lord Howe Island (LHI), Australia, were transported to aquarium at University Western Sydney. FP localization and optical properties were examined in excised tissues by confocal imaging and micro-spectral (λxy-scan) detection (Leica TCS SP5, Leica Microsystems) as previously [5, 8]. Photoactivity of FPs in coral cells was examined by FRAP TCS SP5 Leica Wizard Software at different laser excitations – 405, 458, 488, 514, 561, 633 nm. Photoswitching and photoconversion analyses were done on coral cells, purified FPs or FPs expressed in *E.coli* and in mammalian cells (L6) by confocal imaging. FP localization in neuronal cells and processes was also investigated by DiI staining (Molec. Probes # D-3899) and serotonin staining (Chee & Byrne, 1999). Cloning of PAFPs was of dissected coral samples. Total RNA was isolated using RNAqueous kit (Ambion); amplified cDNA prepared by SMART protocol; cDNA coding sequences obtained by Step-Out RACE protocol, products cloned into pGEM-T vector (Promega), sequenced, re-amplified, cloned into vector as described [1]. To test the expression of PAFPs in mammalian cells, their cDNA sequences were subcloned into pEGFP-N1 (Clontech, USA) vector using standard molecular methods.

Results and Discussion

Our studies found a surprising diversity of PAFPs. Confocal imaging and photoconversion / photoswitching tests on coral tissues identified that PAFPs were present in 17 of 25 corals examined. At some sites, PAFPs were especially common – at one LHI site, out of 6 GFP-type proteins cloned from corals, 3 were green-to-red photoconverters, homologous to Kaede [9] and EosFP [10] and one was homologous to Dronpa [11]. Kaede/EosFP proteins are widely used in cell biology, embryology and in super-resolution imaging. They convert irreversibly from green to red fluorescence under UVA / violet light [9, 10]. Dronpa [11] is a well-known photochromic FP that switches between a green fluorescent state and a dark form. Our studies identified a novel PAFP – a bright red FP that converts to a yellow at green light irradiation (CoralFlame). It was well expressed in mammalian cells and showed that it had tremendous applications as a targeted protein tracker (Fig. 1 f, g).

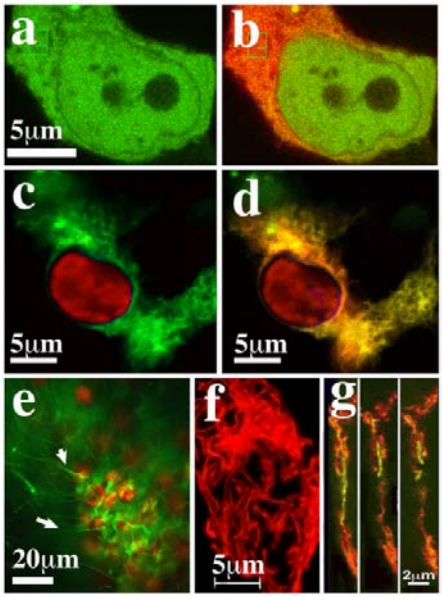

Fig. 1. PAFPs in coral and mammalian cells. (a-b) Green to red conversion of EosFP in L6 cells; (c-d) similar conversion of PAFP in coral cell enclosing algal symbiont (red); (e) green PAFP in neuronal processes of coral cells enclosing symbiont cluster (red); (f) CoralFlame fused to mitochondrial protein expressed in L6 cell; (g) t-series showing its red-to-yellow conversion and tracking of mitochondrial cysternae

The discovery that PAFPs are widespread points to their significant function. Investigation of their cellular localization patterns found CoralFlame-type, Kaede-type and Dronpa-type PAFPs in almost every type of coral cell. They are often localized in cells harboring symbiotic microalgae (Fig. 1 c,d). Corals are highly dependent on intracellular symbionts that convert light energy and provide ~80% of coral's metabolic requirements. However, symbionts' photosynthesis can be deleterious to corals due to generated reactive oxygen species (ROS). Cellular PAFPs may have multiple functions of photoprotection, photomodulation, sensing and ROS deactivation. Interestingly, PAFPs were found prominent in neuronal and variously ciliated sensory cells (Fig. 1e), implying a potential photosensory role. It can be hypothesized that PAFPs may interacts with membrane proteins and their proton pumping mode is feasible in photoswitchers such as Dronpa, which occurs in the protonated state.

It is now timely to reconsider that GFPs are not passive light absorbers and emitters, but are functional light-activatable proteins, crucial to the biology of marine organisms. Evidence is also mounting that by learning their biology, we can better develop powerful cellular biosensors and optogenetic tools that provide precise control of specific events in living cells and organisms.

Acknowledgements

This work was supported by the ARC Discovery grant to A. Salih. Thanks to Y. Ma (MSc studentship) and to M. Matz for advice in this project. EosFP plasmids provided by J. Wiedenmann.

References

1. N.O. Alieva et al., *PLoS ONE,* 2008, **3**, e2680.
2. M.V. Matz, et al., *Nat Biotechnol.*, 1999, **17**, 969-973.
3. K.A. Lukyanov et al., *Nat. Rev. Mol. Cell Biol.*, 2005, **6**, 885-891.
4. M. Fernández-Suárez, and A.Y. Ting, *Nature Reviews*, 2008, **9**, 929-931.
5. A. Salih et al., *Nature*, 2000, **408**, 850-853.
6. N. Agmon, *Biophys. J.*, 2005, **88**, 2452-2461.
7. A.M. Bogdanov et al., *Nat. Chem. Biol.*, 2009, **5**, 459-461.
8. A. Salih et al., *Proc, SPIE* San Jose, *U. S. A.*, 2004, **5329**, 61-72.
9. R. Ando et al., *Proc. Natl. Acad. Sci. U. S. A*, 2002, **99**,12651-12656.
10. J. Wiedenmann et al., *Proc. Natl. Acad. Sci. U. S. A.*, 2004, **9** (101), 45, 15905-15910.
11. S. Habuchi et al., *Proc. Natl. Acad. Sci. U. S. A.*, 2005, **102**, 9511-9516.

Invited

NONLINEAR OPTICAL IMAGING FOR BIOMEDICAL DIAGNOSIS

M. Schmitt[1], **B. Dietzek**[1,2], **D. Akimov**[2], **T. Meyer**[2], **N. Vogler**[1,2], **G. Bergner**[2], **C. Krafft**[2], **N. Bergner**[2], **C. Matthäus**[2], **P.Rösch**[1], **C. Krafft**[1,2], and **J. Popp**[1,2]

[1] Institute of Physical Chemistry and Abbe Center of Photonics, Friedrich-Schiller University, Jena, Germany, m.schmitt@uni-jena.de

[2] Institute of Photonic Technology, Jena, Germany

The impact of molecular/chemical microspectroscopy (imaging) on modern biomedical research has been significantly increased within the last decade since microspectroscopic techniques like e.g. fluorescence or vibrational spectroscopy (IR-absorption, Raman scattering) allow gaining new valuable molecular information on complex biological specimen that cannot be acquired by conventional microscopy. Conventional light microscopes utilize predominantly differences in absorption, transmission and reflection of white light in biological specimen to highlight the morphology of the biological specimen under investigation. However, these conventional microscopic techniques can be extended by employing several other light matter interaction phenomena based on molecular spectroscopy to generate molecular/chemical microscopic images. In other words spectroscopic methods like e.g. fluorescence or vibrational spectroscopy (IR and Raman) are of particular relevance for modern biomedical imaging since they provide beside morphological information direct molecular contrast.

In particular fluorescence microscopy techniques are extremely capable methods of resolving a broad variety of questions in life sciences and medicine. Besides fluorescence microscopy Raman based technologies have shown its great impact on biomedical research. Raman yields information on inherent molecular vibrations that provide a highly specific molecular fingerprint of the chemical structure and biochemical composition of e.g. biological cells, tissues etc. [1]. The visualization of these unique molecular vibrations by means of Raman spectroscopy takes place without the need of external markers. Thus Raman based techniques are labelfree. As cancer and other pathologic anomalies are accompanied by changes in the biochemical composition and structure of biomolecules in cells and tissue, the Raman spectrum provides a sensitive and specific fingerprint of the type and state of the specimen. Therefore biomedical imaging by means of Raman microspectroscopy offers novel approaches towards disease diagnosis based on the chemical composition of tissue and cells.

While the advantages of Raman spectroscopy are its unprecedented high molecular specificity and its versatility it suffers from its poor sensitivity. In other words the disadvantage of Raman spectroscopy is the low Raman scattering cross section, why the detection of molecules being present in very low concentrations is limited. This disadvantage can be overcome by utilizing non-linear Raman phenomena like CARS = coherent anti-Stokes Raman scattering which belong to the most promising Raman techniques since they combine signal enhancement due to the coherent nature of the process with further advantages such as directional emission or no disturbing interference with autofluorescence .Thus, for clinical Raman applications the transformation of linear Raman spectroscopy into the more sensitive non-linear Raman method CARS is extremely promising. The implementation of CARS in laser scanning microscopes enables to collect images at video time rates. Therefore, CARS is a promising candidate for real-time Raman imaging studies of cells and tissues.

In this contribution it will be shown that the CARS images recorded from various tissue sections (colon, skin, brain etc.) correlate well with the corresponding Raman images [2–4]. However, Raman images were obtained from univariate and multivariate (k-means clustering) methods, whereas all CARS images represent univariate results. Variances within tissue sections could be visualized in chemical maps of CARS and Raman images. However, the identification of tissue types and the characterization of variances between different tissue sections were only possible by analysis of the k-means cluster mean spectra [2]. Based on these comparative Raman / CARS studies we suggest a complementary application of Raman and CARS imaging where Raman imaging defines spectral regions and spectral markers that are essential for tissue classification and CARS imaging at different Stokes shifts probes these spectral descriptors at video-rate speed. In order to further improve the diagnostic result the CARS microscope can be easily extended by the two other non-linear contrast phenomena second harmonic generation (SHG) and two-photon fluorescence (TPF). SHG and TPF highlight morphological / structural features by displaying collagen structures (SHG) and the spatial

distribution of autofluorophores like e.g. NAD(P)H, flavines, elastine etc. Overall the application of such a Raman/CARS/SHG/TPF multimodal imaging approach provides detailed insight into the tissue morphochemistry with significant histopathological information (see Fig. 1) [3, 4].

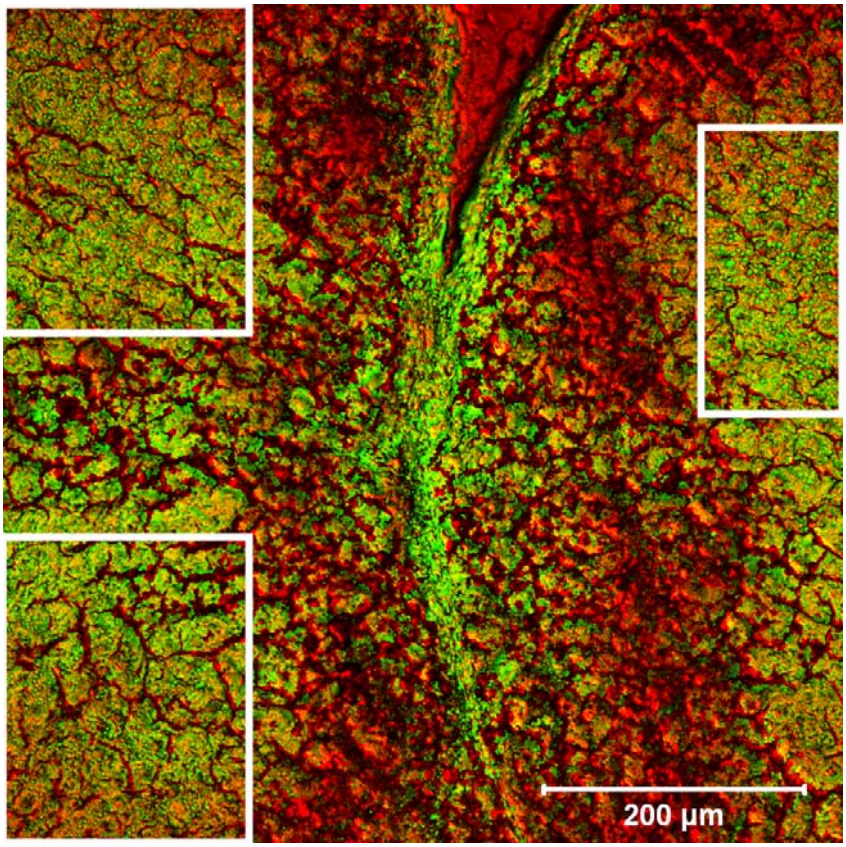

Fig. 1. CARS/SHG/TPF multimodal image of a fibrotic rat liver

Acknowledgements

Financial support of the EU via the "Thüringer Kultusministerium (TKM)" (Projects: B714-07037, B578-06001, 14.90 HWP; PE113-1), the "Thüringer Aufbaubank (TAB)" (Projects: 2008FE9112, 2008FE9152) the Federal Ministryof Education and Research, Germany (BMBF) (Projects: 13N8369, 03IP513, 0312032B, 13N9364, 13N9549, 13N9205) the German Science Foundation (Po563/7-1, GK 1257, JSMC) and the Fonds der Chemischen Industrie are greatly acknowledged.

References

1. C. Krafft, B. Dietzek, and J. Popp, *Analyst.*, 2009, **134**, 1046–1057.
2. C. Krafft, A. Ramoji, C. Bielecki, N. Vogler, T. Meyer, D. Akimov, P. Rösch, M. Schmitt, B. Dietzek, I. Petersen, and J. Popp, *J. Biophoton.*, 2009, **5**, 303–312.
3. T. Meyer, N. Bergner, C. Bielecki, C. Krafft, D. Akimov, B. Romeike, R. Reichart, R. Kalff, B. Dietzek, and J. Popp, *J.B.O.*, 2011, **16**, 021113.
4. N. Vogler, T. Meyer, D. Akimov, I. Latka, C. Krafft, N. Bendsoe, K. Svanberg, B. Dietzek, and J. Popp, *J. Biophoton.*, 2010, **3**, 728–736.

NEAR-INFRARED FLUORESCENT PROTEINS FOR WHOLE-BODY IMAGING

D. Shcherbo[1], **I.I. Shemyakina**[1], **A.G. Zaraisky**[1], **M.W. Davidson**[2], **G.D. Luker**[3], and **D.M. Chudakov**[1]

[1] Shemyakin-Ovchinnikov Institute of Bioorganic Chemistry RAS, Moscow, Russia, dshcherbo@gmail.com
[2] Florida State University, Tallahassee, USA
[3] Center for Molecular Imaging, University of Michigan Medical School, Ann Arbor, Michigan, USA

Introduction

Nowadays GFP-like fluorescent proteins (FPs) are widely used as fluorescent markers. Low toxicity, high stability and autocatalytic host-independent chromophore formation made them indispensable tools for *in vivo* imaging studies. Depending on the used method and intention different objects varying from single molecules to whole animals can be labeled. In the last decades the fluorescent proteins developers have obtained remarkable achievements, including the development of photoactivatable variants, a number of fluorescent biosensors and other specifically-tailored instruments, and a broad palette of proteins for multicolor imaging.

However, low brightness has remained a problem in the far-red variants. This hampers multicolour labeling and whole-body imaging techniques because mammalian tissues are much more transparent in the so-called "optical window" (650–1100 nm). On the other hand, a wide variety of GFP-like fluorescent proteins applications strictly require their monomeric state, but at the same time most of naturally occurring FPs are oligomers. Many fusion constructs, as well as most biosensors are very sensitive to reporter oligomerization, and of course to further possible aggregation. Thus, it is crucial to develop monomeric FP variants. Unfortunately, artificial red monomers are still not able to perform in fusions as good as the natural green ones.

Combining different mutagenesis strategies we have developed two novel near-infrared fluorescent proteins eqFP650 and eqFP670 for whole body imaging as well as "supermonomeric" red fluorescent protein FusionRed optimized for fusions.

eqFP650 and eqFP670 for whole-body imaging

One of our goals while developing near-infrared FPs was to reduce possible cytotoxic effects as this would greatly simplify long-term whole-body animal imaging. First, we selected in a bacterial expression system the most low-toxic variant of far-red fluorescent protein Katushka. Next, based on the crystal structure of the related far-red fluorescent protein mKate (PDB ID: 3BXB), we selected amino acid positions in proximity to the chromophore (including Met14, Leu16, Met44, Thr62, Tyr121, Ser148, Ser165, Met167, Arg203 and Leu205) for targeted mutagenesis (numbering in accordance with *Aequorea victoria* GFP). We manually screened bacterial libraries containing these mutants using a fluorescence stereomicroscope equipped with a 650LP emission filter and a built-in spectrofluorimeter. We screened more than a million individual colonies and selected two red-shifted variants, named eqFP650 and eqFP670 that had substitutions N24G, M44A and M14T, N24G, M44C, S148N, S165N, respectively. eqFP650 generally retained the high brightness of Katushka and was characterized by a strong bathochromic shift, with excitation and emission peaks at 592 nm and 650 nm, respectively.

To date, eqFP650 is the brightest fluorescent protein with emission maxima above 635 nm and should be an optimal genetically encoded marker for *in vivo* imaging. eqFP670 is characterized by lower brightness but stronger bathochromic shift, with excitation and emission peaks at 605 nm and 670 nm. eqFP670 is to our knowledge the first GFP-like fluorescent protein with such long-wavelength emission, approximately half of which falls in the infrared part of the spectrum. Compared to Katushka, eqFP670 had fourfold greater infrared brightness. Furthermore, eqFP670 had high pH stability and extremely high photostability and should allow for accumulation of the fluorescent signal over long exposure times. The combination of Asn148 and Asn165 in eqFP670 is unique and has not been encountered in other fluorescent proteins. This implies tight packing around the chromophore, which probably forms the basis of the high photostability and pH resistance.

Although we demonstrate that eqFP650 now may be the preferable near-infrared fluorescent protein for *in vivo* cell-labeling experiments, we believe that development of longer-wavelength

fluorescent proteins such as eqFP670 with high brightness and of true monomeric variants for protein fusions will increase the sensitivity and capabilities of deep-tissue imaging techniques.

FusionRed, a red fluorescent protein optimized for fusions

Red fluorescent protein FusionRed is a "supermonomeric" (i.e. purely monomeric at high concentrations at HPLC) derivative of popular far-red monomeric fluorescent protein mKate2. mKate2 appeared to be the best variant to start with due to its bright and stable far-red fluorescence. Moreover, mKate2 performs well in lots of fusion constructs tested. It is also important that mKate2 demonstrates low toxicity in *Xenopus* embryos and does not demonstrate any tendency to form visible aggregates or non-specific localization in mammalian cells at high expression levels.

Our monomerization strategy implied analyzing recently obtained crystallographic data on mKate structure and choosing a set of amino-acid positions which should affect oligomerization with further site-directed mutagenesis of selected points. While HPLC shows partial dimerization of mKate2 and dimeric nature of the far-red fluorescent protein mNeptune, both developed from mKate, FusionRed behaves as pure monomer at concentrations at least up to 10 mg/ml, as well as mEGFP that served as a "gold standard". To test FusionRed performance in fusions we have generated chimeric constructs with more than 40 proteins of interest. FusionRed shows low cytotoxicity compared to popular red monomers and performs in fusions similar to the best green fluorescent proteins. We believe that FusionRed will serve as an effective reporter in fusions for protein localization, multicolor imaging, FRET-based methods and as a core for the novel red biosensors.

References

1. D.M. Chudakov, S. Lukyanov, and K.A. Lukyanov, *Trends Biotechnol.*, 2005, **23**(12), 605-13.
2. K. Konig, *J. Microsc.*, 2000, **200**(Pt 2), 83-104.
3. R.M. Hoffman, *Nat. Rev. Cancer*, 2005, **5**(10), 796-806.
4. M.Z. Lin, M.R. McKeown, H.L. Ng, T.A. Aguilera, N.C. Shaner, R.E. Campbell, S.R. Adams, L.A. Gross, W. Ma, T. Alber, and R.Y. Tsien, *Chem. Biol.*, 2009, **16**(11), 1169-79.
5. S. Pletnev, D.Shcherbo, D.M. Chudakov, N. Pletneva, E.M. Merzlyak, A. Wlodawer, Z. Dauter, V. Pletnev, *J. Biol. Chem.*, 2008, **283**(43), 28980-7.

CORRELATION SPECTROSCOPY BASED ON THIRD-HARMONIC GENERATION MICROSCOPY

V. Shcheslavskiy[1,2], **D. Ivanov**[1,3], **M. Geissbühler**[1], **T. Lasser**[1], **W. Becker**[2], and **V. Yakovlev**[4]

[1] Laboratoire d'Optique Biomedicale, Ecole Polytechnique Federale de Lausanne
CH-1015, Lausanne, Switzerland
[2] Becker&Hickl GmbH, Nahmitzer Damm 30, 12277 Berlin, Germany
vis@becker-hickl.de
[3] Photochemistry Centre of Russian Academy of Sciences
Ul. Novatorov 7a, 117421 Moscow, Russia
[4] Department of Physics, University of Wisconsin-Milwaukee
1900 E. Kenwood Blvd., WI 53211, USA

Introduction

Fluorescence correlation spectroscopy (FCS) is a powerful optical technique which is based on registration and analysis of signal's intensity fluctuations originating from fluorescent species [1]. During the last decade, FCS combined with different microscopy techniques has become invaluable tool for single-molecule studies [2]. Although there was a great progress in FCS, it has several disadvantages. First, it requires labeling of the systems with fluorophores which often leads to modifications in the properties of these systems. Another problem which restricts the application of fluorophores is their bleaching.

For these reasons, there has long been a need for methods which lack these restrictions. Recently, coherent anti-Stokes Raman scattering (CARS) signals were correlated to monitor the dynamics of the small particles [3]. It has been shown that CARS correlation spectroscopy is sensitive enough for the detection of the particles with the sizes well below the wavelength of light. Although this elegant technique has no single molecule sensitivity, it offers interesting possibilities for investigation of microviscosities.

In this report we address an application of correlation technique for third-harmonic generation (THG) from nanospheres. Compared to FCS it has several distinct advantages. First, there is no problem with photobleaching of the nanoparticles. Second, THG is a coherent process with directional emission (mainly forward) which means better collection efficiency, and, consequently, stronger signal. Finally, the separation between the excitation and emission wavelengths is easier which results in better signal to noise ratio.

Materials and Methods

The experimental setup (Fig. 1) consists of a home-built mode-locked Cr:forsterite laser generating 40 fs pulses at 25MHz repetition rate. With the average power of about 350 mW, this results in about 15 nJ per pulse, which is more than enough to initiate THG. The laser beam is focused with an aspheric lens into a quartz flow cell, containing an aqueous solution of polystyrene beads. Aqueous suspensions of polystyrene beads with diameters of 109, 200, 356, 770, and 990 nm (Polysciences Inc.) were used to characterize Third- harmonic correlation spectroscopy. The signal was collected with a single-photon counting module (SPCM) and processed with a hardware digital correlator attached to a standard PC.

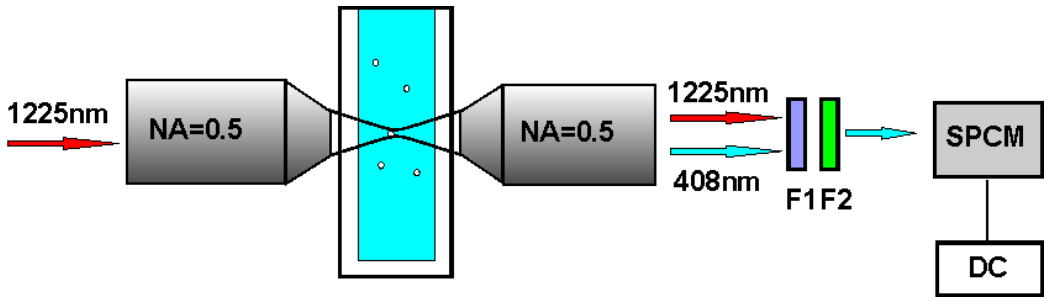

Fig. 1. Experimental setup for third-harmonic correlation spectroscopy

Results and Conclusions

Due to the much tighter focus in the lateral direction as compared to the axial direction the two-dimensional diffusion model is a good approximation [2]. In this case, the autocorrelation function can be expressed as:

$$G(\tau) = 1 + \frac{1}{\langle N \rangle}\left(1 + \frac{\tau}{\tau_d}\right)^{-1}, \quad (1)$$

where the diffusion time equals:

$$\tau_D = \frac{w_0^2}{12D}, \quad (2)$$

w_0 is the focus diameter in lateral plane, D is the diffusion coefficient. Autocorrelation functions measured for five different sizes of polystyrene particles are presented in Fig. 2a. To fit the experimental curves, we used Eq. (1). The diffusion times for different spheres were experimentally determined from these fits and are depicted in Fig. 2b.

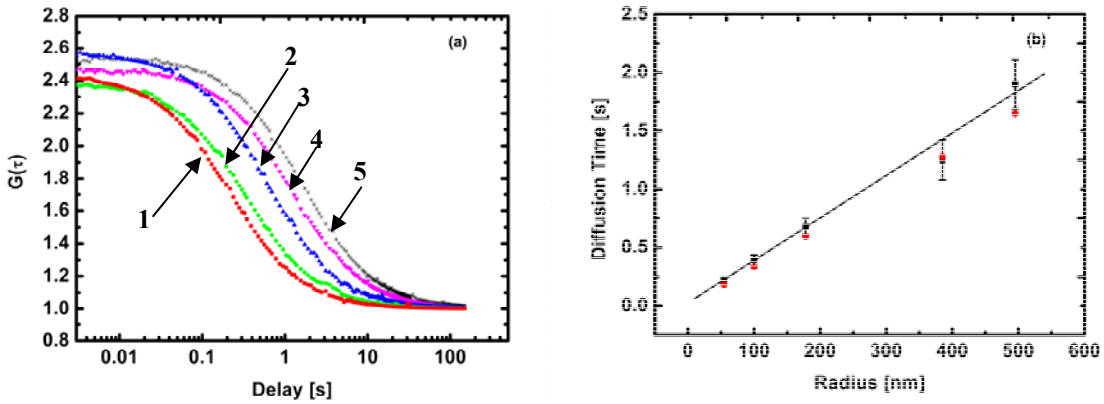

Fig. 2. a) The autocorrelation curves for different sizes of the polystyrene beads: 1 – (□): 109 nm; 2 – (●): 200 nm; 3 – (▲): 356 nm; 4 – (▼): 770 nm; 5 – (*): 990 nm. b) Diffusion times of the beads. Circles represent calculated values

The diffusion coefficient is related to the size of the sphere via Stokes-Einstein relation:

$$D = \frac{kT}{6\pi\eta r}, \quad (3)$$

where η is the dynamic viscosity of the solution, r is the radius of the sphere, k is Boltzmann constant, and T is the temperature of the solution. From Eq. (2) and Eq. (3) the average size of the waist of the beam can be determined:

$$w_0 = \left(2\frac{\tau_D}{r}\frac{kT}{\pi\eta}\right)^{1/2}, \quad (4)$$

From the slope of the diffusion time vs size of the sphere (Fig. 2b), we calculated the size of the waist to be 3.1±0.25 μm. This value agrees well with the focal spot diameter obtained by the axial scan of the surface of the flow cell through the focus of the incident beam (2.9±0.15 μm).

To conclude, we have demonstrated third-harmonic correlation spectroscopy (THCS) for probing diffusion processes. THCS is a new type of optical fluctuation spectroscopy based on third-order nonlinear optical process. Compared to fluorescence correlation spectroscopy, THCS offers an opportunity to perform experiments without fluorophores, i.e. there is no problem with photobleaching. This implies that THCS can be effectively used to study slow relaxation processes.

References

1. D. Magde, W.W. Webb, and E. Elson, *Phys. Rev. Lett.*, 1972, **29**, 705-708.
2. R. Rigler, U. Mets, J. Widengren, and P. Kask, *European Biophysics Journl.*, 1993, **22**, 169-175.
3. J. Cheng, E. Potma, and S. Xie, *J. Phys. Chem. A*, 2002, **106**, 8561-8568.

IN VIVO STUDY OF BIODISTRIBUTION AND PHARMACOKINETICS OF NEW PHOTOSENSITIZERS

M.V. Shirmanova[1,2], I.V. Balalaeva[2], L.G. Klapshina[3], I.V. Turchin[4], M.V. Sirotkina[1,2], and **E.V. Zagaynova[1]**

[1] Nizhny Novgorod State Medical Academy, Russia, Shirmanovam@mail.ru
[2] N.I. Lobachevsky State University of Nizhny Novgorod, Russia
[3] G.A. Razuvaev Institute of Organometallic Chemistry RAS, Nizhny Novgorod, Russia
[4] Institute of Applied Physics RAS, Nizhny Novgorod, Russia

Recently, numerous photosensitizers for fluorescence diagnostics and photodynamic therapy (PDT) have been developed. Among them are phthalocyanines, naphthalocyanines, porphyrins, benzoporphyrins, chlorins, bacteriochlorins, purpurines, texaphyrins, and porphycenes [1, 2]. Fluorescent proteins are considered to be genetically encoded photosensitizers [3]. However, no ideal photosensitizer has been found so far.

Development of new drugs becomes quite complicated because of the methods used in pre-clinical studies. In particular, tissue chemical extraction is widely employed for an accurate concentration assessment of a potential photosensitizer [4]. This approach is known to be tedious and routine and requires a lot of animals. To investigate tumor selectivity of a photosensitizer and its distribution in tissues fluorescence confocal microscopy, fluorescence or absorption spectroscopy *in situ*, and high-resolution fluorescence microendoscopy are in use [5, 6]. These methods are based on point measurements, and essential data spread is often observed, so multiple measurements are needed to decrease error. Therefore, noninvasive whole-body imaging technologies such as diffuse fluorescence tomography and non-tomographic imaging have been taking on increasing significance. But because of complicated implementation tomographic utility *in vivo* is still limited. While non-tomographic modalities, reflectance and transillumination, are technically easy to realize, they are attractive tools for fluorescence detecting in small animals *in vivo*.

The purpose of this work is to develop the method of transillumination fluorescence imaging for pharmacokinetic study of photosensitizers and to investigate biodistribution and dynamics of tumor-uptake of porfirazine metal-complexes.

The experiments have been performed on female CBA mice with subcutaneously transplanted mouse cervical carcinoma. Tumors have been obtained by s.c. injection of the ground tissue from solid tumor suspended in a nutrient medium 199. Experiments have started when the largest diameter of the lesions was 7-8 mm (10-12 days following transplantation).

To develop new fluorescence imaging method photosens, protoporphyrin IX and fotoditazin photosensitizers have been used because they are clinically approved, and their pharmacokinetic properties have already been completely described. Photosens is sulfo-substituted aluminium phthalocyanine (Niopic, Russia). The mice have been injected with photosens 1 mg/kg i.v. Alasens (Niopic, Russia) is a preparation on the basis of 5-aminolaevulinic acid (ALA) which induces accumulation in tumor of endogenous protoporphyrin IX (Pp IX). Alasens has been administered per os in a dose of 400 mg/kg. Fotoditazin is N-methyl glucosamine chlorin e6 salt (Veta-Grand, Russia). The mice have received 10 mg/kg of fotoditazin i.v.

As a new potential photosensitizer ytterbium cyanoporphyrazine complex has been examined. Aqueous suspensions of the complex have been prepared by solubilization in polyethyleneglycol (PEG 7000) and by incorporation in nanoparticles consisting of PEG core and fluorinated hybrid silica shell doped with the complex. The complex has been injected i.v. in a dose of 12 mg/kg.

Fluorescence imaging *in vivo* has been performed using an original setup where synchronous scanning of an animal is provided by a single source-detector pair in the transilluminative configuration. Images have been obtained before the chemicals administration, 15 min, 1, 2, 3, 4, 6 h afterwards, and then once a day during 9 days. For quantification of photosensitizer in tumors signal calibration has been made on model medium of lipofundin and Indian ink. For verification of the photosensitizers in healthy organs and tumors fluorescence has been also analyzed by fluorescence confocal microscopy and fluorescence spectroscopy *ex vivo*.

It has been shown that after chemicals administration a fluorescence signal rise is observed in the strained region of skin, in tumor and abdominal cavity of mice on the transilluminative fluorescence

images *in vivo*. In abdomen several organs of greatest photosensitizer accumulation can be identified. They are small intestine, kidneys and urinary bladder. 281 images of mice acquired from 1 to 6 hours after the drug administration have been analyzed. In case of photosens number of kidneys on images is 10%, intestines 30%, bladder 43%. For fotoditazin it accounts for 3, 43 and 30% of total number, correspondingly. And for 5-ALA-induced PpIX the number is 13, 31 and 1%. Based on this data *in vivo* one can make an assumption about the main routes of the photosensitizers elimination. However, about one-third of the group of animals organs are hardly distinguished in the images because the whole abdomen area looks bright, which may be related to both anatomical features of mice and metabolic properties of photosensitizers.

Pharmacokinetics of the photosensitizers in mouse tumors has been studied *in vivo* [7]. A fluorescence signal in the tumors has been measured at different times after intravenous injection. The concentrations of photosensitizers in the tumors have been assessed by means of calibration curves. It has been established that the period of maximum uptake of fotoditazin in the tumor is from 1 to 8 h post-injection. At this time fotoditazin concentration in the tumor tissue is about 2 μg/g. Half-life of the drug in the tumor is 21 h, and the time of clearance from the tumor is 9 days. Accumulation of photosens is maximal from 3 h to 24 h after injection, and its concentration in the tumor is about 0.27 μg/g. This photosensitizer is still detectable in the tumor on the 9th day. After oral administration of alasens, a smooth signal growth is detected in tumor area up to 6 h. The 5-ALA-induced Pp IX concentration at this time is about 6 μg/g. By the 2nd day nearly all the photosensitizer is eliminated from the tumor. The results obtained *in vivo* correspond to the standard methods (confocal fluorescence microscopy and point spectroscopic measurements) *ex vivo*. Hence, the proposed method shows the effectiveness for pharmacokinetics study of the photosensitizers.

Using the new method of fluorescence transillumination imaging, data about ytterbium cyanoporphyrazine complex accumulation in tumor and elimination have been received [8]. It has been found *in vivo* that the period of maximum uptake of the complex solubilized in PEG in mouse cervical carcinoma is from 3 to 6 h after i.v. injection, half-life in the tumor is 24 h, time of clearance from the body is about 48 h. An accumulation of the fluorescent nanoparticles reaches its maximum in 1 h post-injection. Then, the fluorescence intensity in the tumors remains at the same level for 3 days. However, the tumor selectivity of the complex is not high enough. The area of the strongest fluorescence in the abdominal cavity in the *in vivo* images is anatomically recognized as intestine. This indicates that the new compounds undergo a hepatic clearance mainly. The conventional *ex vivo* methods (confocal microscopy and point spectroscopic measurements) have detected the largest content of the complex in intestine, liver, skin and tumor tissue.

In this study we have demonstrated the possibility of *in vivo* investigation of photosensitizers biodistribution and pharmacokinetics by means of fluorescence transillumination imaging. Serial imaging in the same animals shows that this technique is capable of detecting photosensitizer accumulation in the mouse organs and tumor and washout over time in individual animals. As a result, new principles of study of photosensitizers in animals have been suggested and used for examination of new photosensitive dyes.

Acknowledgements

This research has been supported by the Ministry of Education and Science (projects Nos. 11.G 34. 31.0017, 2011-1.3.1-201-007/38).

References

1. A.E. O'Connor, W.M. Gallagher, and A.T. Byrne, *Photochem. Photobiol.*, 2009, **85**, 1053-1074.
2. K. Berg, P.K. Selbo, A. Weyergang, et al., *J. Microscopy,* 2005, **218**, Pt 2, 133-147.
3. E.O. Serebrovskaia, O.A. Stremovskiĭ, D.M. Chudakov, et al., *Bioorg Khim*., 2011, **37**(1), 137-44 (in Russian).
4. C. Perotti, A. Casas, H. Fukuda, et al., *Br. J. Cancer*, 2002, **87**, 790-795.
5. C. Klinteberg, A. Pifferi, and S. Andersson-Engels, *Appl. Opt.*, 2005, **44**(11), 2213-2220.
6. W. Zhong, J.P. Celli, I. Rizvi, et al., *Br. J. Cancer,* 2009, **101**, 2015-2022.
7. M. Shirmanova, E. Zagaynova, M. Sirotkina, et al., *J. Biomed. Opt*., 2010, **15**, 048004.
8. L.G. Klapshina, W.E. Douglas, I.S. Grigoryev, et al., *Chem. Commun.*, 2010, **46**, 8398-8400.

LOCAL HYPERTHERMIA OF A CERVICAL CARCINOMA BASED ON GOLD NANOPARTICLES

M.A. Sirotkina[1,2], **V.V. Elagin**[1,2] **M.V. Shirmanova**[1], **V.A. Nadtochenko**[3], and **E.V. Zagaynova**[1]

[1] Nizhny Novgorod State Medical Academy, Russia, Sirotkina_m@mail.ru
[2] N.I. Lobachevsky State University of Nizhny Novgorod, Russia
[3] N.N. Semenov Institute of Chemical Physics RAS, Moscow, Russia

Introduction

To attain success in hyperthermia in combination with nanoparticles it is necessary to treat in time maximal concentration of nanoparticles in the tumor node. The second point is measurement of temperature outside and inside the tumor.

The goal of the research was to design a method of local laser hyperthermia of tumor with gold plasmon-resonant nanoparticles under noninvasive examination of the time of nanoparticles accumulation in tumor.

Materials and Methods

Nanoparticles. An aqueous colloid of plasmon resonant gold nanobranches (10^9 particles/ml) stabilized with biocompatible coating PEG was used. The nanoparticles were 200–250 nm in size. The extinction maximum of the gold nanobranches was at the wavelength of 850 nm which is optimal for the OCT imaging and laser hyperthermia

Animals. The study was performed on female mice of CBA line bearing cervical carcinoma. The tumor was transplanted subcutaneously. The hair from the ***skin*** surface ***over the tumor*** had been removed. Animals were divided into three groups of 10 mice – one untreated and two treated: nanoparticles-labeled tumors and nanoparticles-free tumors

Optical approach .A noninvasive control of nanoparticle accumulation in the tumor was carried out *in vivo* by the OCT device designed at the Institute of Applied Physics of the Russian Academy of Sciences (IAP RAS). The OCT device has the following characteristics: a probing radiation wavelength of 900 nm, power 2 mW, spatial resolution 15-20 μm, an imaging depth up to 1.5 mm. The OCT images were obtained immediately before injection of nanoparticles and afterwards every 30 min for 5 hours. The nanoparticles uptake in tumor was estimated by an increase of the signal intensity in the OCT images.

Laser hyperthermia in combination with gold nanoparticles. A preliminary comparative study of the efficiency of laser heating of the nanoparticles-labeled tumors and nanoparticles-free tumors was undertaken. An appropriate laser regime for mild hyperthermia was selected from work [1]. The laser treatment was performed 5 hours after the nanoparticle injection. The tumors were exposed for 20 min to light from an 810 nm diode laser. A power density was approximately 1.2–1.5 W/cm^2. It depended on the tumor node size. The superficial tumor temperature was controlled to be between 44–45°C by means of a standard IR-thermograph. The passive acoustic method was applied to control the temperature inside tumors. The device was developed at the IAP RAS.

Post-treatment tumor size measurements were taken daily. A tumor growth inhibition (*TGI*) was calculated by the equation presented in the work [2].

Results

OCT control of nanoparticles accumulation in tumor nodes

The OCT images of tumors before nanoparticles administration feature an average OCT signal level and small penetration depth of the signal. Accumulation of nanoparticles into tumors gave the following effects: enhanced brightness of the images relative to the control image and an increase of the signal penetration depth. The time of maximum nanoparticles accumulation in tumor was found to be 4–5-hour after nanoparticles application.

Laser hyperthermia of the tumor

When the laser was switched on the temperature rose steeply in case of the nanoparticles-labeled tumors and reached the peak at 44°C in 3 and a half minutes. To sustain the temperature at the same

level for 20 minutes it was necessary to decrease the laser power from 1.2 W to 0.9 W. After the laser was switched off the temperature went down very rapidly. In case of the nanoparticles-free tumors the temperature changed five times slower and it was not necessary to decrease the laser power. The study using the IR thermography demonstrated that the nanoparticles-labeled tumors were heated locally.
By means of the passive acoustic method the nanoparticles-labeled tumors were found to be heated from the inside.

Tumor growth inhibition

Tumor volume variation after laser hyperthermia is illustrated in fig. 1. It was found that the laser hyperthermia in combination with gold nanoparticles provided the antitumor effect. Tumor growth inhibition (TGI) was around 65% in the group of nanoparticles-labeled tumors and −7.5% in the case of nanoparticles-free tumors.

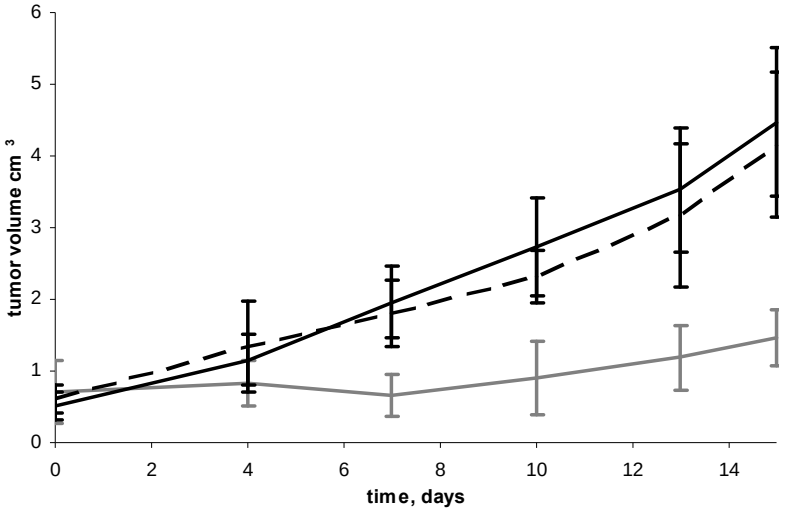

Fig. 1. The influence of laser hyperthermia in combination with gold nanoparticles on the growth of cervical carcinoma model of tumor. The dashed line is untreated tumors, the grey line is nanoparticles-labeled tumors, the black line is nanoparticles-free tumors. Each point represents mean tumor volume (cm^3) ± SD (n = 10 mice per group)

Conclusions

In the present study the OCT was demonstrated to be an objective method for in vivo control of gold nanoparticles accumulation in tumor. An optimal time for laser treatment was found to be 4-5 hours after nanoparticles administration by means of the OCT. The applied nanoparticles were effective for a local laser hyperthermia: the tumors were heated five times faster, the output laser power was less, heating occurred inside the tumors and very locally. The tumor growth inhibition was around 65% in the group of nanoparticles-labeled tumors.

Acknowledgements

This work was supported in part by the Ministry of Education and Science (projects Nos. 02.740.11.0713, 11.G 34. 31.0017) and the Russian Foundation for Basic Research (project No. 09-02-00539).

References

1. M.H. Falk and R.D. Issels, "Hyperthermia in oncology", *Int. J. Hyperthermia*, 2001, **17** (1), 1-18.
2. T. Friess, W. Scheuer, and M. Hasmann, "Combination Treatment with Erlotinib and Pertuzumab against Human Tumor Xenografts Is Superior to Monotherapy", *Clin. Cancer Res.*, 2005, **11**(14), 5030-5039.

Invited

PLASMONIC NANOSENSORS FOR MOLECULAR AND FUNCTIONAL CELLULAR IMAGING *IN VIVO*

J. Aaron[1], S. Mallidi[1], G. Luke[1], A. Papagiannaros[1], S. Emelianov[1,2], and **K. Sokolov[1,2]**

[1] Department of Biomedical Engineering, University of Texas at Austin, Austin, TX 78712
[2]Department of Imaging Physics, MD Anderson Cancer Center, Houston, TX 77030
kostia@mail.utexas.edu

Introduction

One of the major problems in selective detection, monitoring and treatment of cancer is the fact that cancer biomarkers are not unique to cancer cells. Identical molecules are present in normal cells as well; however, their expression is often elevated in cancer [1]. Therefore, selectivity toward cancerous cells can be achieved through development of molecular probes that dramatically change properties in the presence of an over-expressed biomarker.

Closely-spaced plasmonic nanoparticles exhibit strong color change, quadratic increase in cross-section per particle, and modified polarization of the scattered light [2, 3]. We explore non-linear phenomena which are exhibited by plasmonic nanoparticles when they form closely spaced assemblies in the presence of a target molecule such as overexpressed cancer biomarker, e.g. EGFR. The assembly formation by nanoparticles is mediated by targeting molecules such as antibodies that interact with the biomarker of interest. Our experiments with living cells showed that EGFR mediated assembly and plasmon coupling of gold bioconjugates results in a dramatic spectral shift of more than 100 nm in plasmon resonance frequency of the nanoparticles giving a very bright red signal. In addition, coherent scattering effects result in a quadratic increase in the total scattering cross-section of closely spaced nanoparticles. These effects allow optimization of excitation wavelength for highly sensitive detection of labeled cells, even in the presence of single unbound gold bioconjugates. Here, we first study the underlying mechanism of plasmon resonance coupling in molecular specific imaging of live cancer cells. Then we apply this approach to *in vivo* cancer imaging using a combined 3D ultrasound and molecular specific photoacoustic (PA) imaging.

Results

Optical Imaging in cell cultures

We imaged cancer cells with a darkfield microscope equipped with a hyperspectral imaging system and color CCD camera. The unlabeled cells appear blue due to the intrinsic scattering. The labeled cells have dim green regions and bright easily visible regions which appear different shades of orange. The orange color corresponds to the closely spaced assemblies of anti-EGFR gold conjugates which interact with EGF receptors. Hyperspectral imaging revealed more than a 100 nm red shift in light scattering associated with the orange colored assemblies of the particles in highly proliferating cells.

Mechanism of Optical Contrast in Molecular Imaging of Cancer Cells

Dynamic imaging of live cells labeled with anti-EGFR nanoparticles resulted in a progressive color change from green to yellow, and, finally, to orange-red. The color changes are well-correlated in time with trafficking dynamic of EGFR [4]. This effect was disrupted by a potent EGFR inhibitor, AG1478, which interferes with EGFR internalization [5].

In order to establish a relationship between the scattering behavior of EGFR-bound plasmonic nanoparticles and the dynamics of EGFR regulation in live cells we carried out labeling at 4°C, 25°C, and 37°C. Temperature control allows the activation and trafficking mechanisms of EGFR to be arrested at critical points: EGFR internalization is inhibited in cells at 4°C; early endosomes form at 25°C; and EGFR regulation proceeds to formation of multivesicular bodies (MVB) and late endosomes within an hour at 37°C [4].

The corresponding transmission electron microscopy (TEM) images of labeled cells showed the temperature-dependent changes in the nanometer-scale organization of EGFR. The combination of optical imaging and electrodynamic simulations allowed us to conclude that the effect of inter-particle coupling produces a red-shift and broadening in scattering of EGFR bound AuNPs [3, 6]. In addition, volume-like aggregates, such as those in endosomes exhibit significantly more spectral shift than 2D aggregates.

In vivo Molecular Photoacoustic (PA) Imaging

First, we characterized three epithelial 3-D tissue phantoms consisting of EGFR(+)human epithelial carcinoma cells (A431 keratinocyte): (1) the control tissue sample with no AuNPs; (2) the targeted tissue sample labeled with EGFR targeted AuNPs; and (3) the non-targeted sample with nanoparticles coated with PEG-SH layer which has no molecular specificity [7]. Then, we carried out animal studies in 3 group of animals: (1) EGFR(+) tumor with IV injection of anti-EGFR AuNPs; (2) EGFR(-) tumor with IV injection of anti-EGFR AuNPs; and (3) EGFR(+) tumor with IV injection of non-specific PEGylated AuNPs. The multi-wavelength PA images were analyzed to obtain the regions of oxygenated/deoxygenated blood and AuNPs interacting with cancerous cells using intraclass correlation analysis [8]. The optical properties of cancer cells labeled with nanoparticles were obtained from tissue phantom measurements.

Silver stain was used to identify areas of nanoparticle accumulation. Histology showed viable and necrotic tumor regions. Four hours after the injection, nanoparticles were primarily located in viable areas of the tumor with limited delivery to the necrotic core. Although nanoparticle accumulation was observed in all cases only specific interactions of anti-EGFR nanoparticles with EGFR(+) tumor model produced strong PA signal in the NIR region.

Conclusions

We demonstrated that plasmon coupling can be used for imaging of EGFR activation in cancer cells as formation of EGFR dimers and further intracellular uptake in early and late endosomes is associated with progressive color changes from green to red/near-infrared of EGFR bound AuNPs. Therefore, antibody targeted AuNPs undergo dramatic optical changes only upon binding to activated EGFR receptors providing a sensitive way of detection of highly proliferative tumor cells. We demonstrated this concept in multi-wavelength PA imaging for detection of 3D distribution of viable EGFR expressing cancer cells *in-vivo*. EGF receptor mediated aggregation of anti-EGFR AuNPs results in an increase of nanoparticle absorption in the NIR region and hence in an increase of the PA signal.

Acknowledgement

This research was support by National Science Foundation grants EB008101 and CA103830.

References

1. D. Hanahan and R.A. Weinberg, *Cell* (Cambridge, Massachusetts), 2000, **100**, 57-70.
2. K. Sokolov, M. Follen, J. Aaron, I. Pavlova, A. Malpica, R. Lotan, and R. Richards-Kortum, *Cancer Research*, 2003, **9**, 1999-2004.
3. J. Aaron, N. Nitin, K. Travis, S. Kumar, T. Collier, S.Y. Park, M. Jose-Yacaman, L. Coghlan, M. Follen, R. Richards-Kortum, and K. Sokolov, *Journal of Biomedical Optics*, 2007, **12**.
4. A. Sorkin and M. von Zastrow, *Nat. Rev. Mol. Cell Biol.*, 2002, **3,** 600-614.
5. J.-X. Zhu, S. Goldoni, G. Bix, R.T. Owens, D.J. McQuillan, C.C. Reed, and R.V. Iozzo, *Journal of Biological Chemistry*, 2005, **280**, 32468-32479.
6. J. Aaron, K. Travis, N. Harrison, and K. Sokolov, *Nano Letters*, 2009, **9**, 3612-3618.
7. S. Mallidi, T. Larson, J. Aaron, K. Sokolov, and S. Emelianov, *Optics Express*, 2007, **15**, 6583-6588.
8. S. Mallidi, T. Larson, J. Tam, P.P. Joshi, A. Karpiouk, K. Sokolov, and S. Emelianov, *Nano Letters*, 2009, **9**, 2825-2831.

Invited

BIOPHOTONIC APPLICATIONS OF QUANTUM DOT STRUCTURES

V.Yu. Timoshenko

Moscow State M. V. Lomonosov University, Physics Department, 119991 Moscow, Russia
E-mail: timoshen@phys.msu.ru

Over the past two decades quantum dots (QDs) have attracted considerable interest due to their remarkable luminescent properties. Recent research efforts were particularly oriented toward biomedical applications of QDs of semiconductor materials of II-VI and VI groups as fluorescent probes [1, 2], therapeutic agents, for example in the destruction of cancer cells [2, 3] as well as for drug delivery [4]. Also QDs of metal oxides as ZnO are promising for bioimaging applications [5]. Fluorescence microscopy has allowed the functional study of various species that have been identified in living cells. The capabilities of this technique have generated a huge interest in developing new probes for tagging molecules and observing changes in their cellular concentrations and activities. Compared to organic dyes and fluorescent proteins, the semiconductor QDs exhibit some advantages such as size- and composition-induced tunable emission, high quantum yield, and low photo-bleaching. However, the widely used II-VI QDs were found to be cytotoxic through the release of cationic ion, i.e. Cd [1]. Therefore, a protective shell (ZnS or a polymer, for example) must be systematically added. In this respect, natural biocompatible surface coatings such as peptides or sugars can be less dangerous for living cells than any other artificial shell. However, no protective shell can guarantee an efficient chemical isolation of the extremely toxic luminescent core of QDs based on II-VI or III-V from the living cell environment. Today, it becomes clear that the cytotoxicity strongly influencing biological cell functioning is one of the major limiting factors for the application of the metal-containing QDs in living cell imaging. In order to avoid this problem, one has to use QDs based on biocompatible materials as silicon (Si) or silicon carbide (SiC). In our work we have examined properties of light-emitting QDs of Si and SiC for biomedical applications as fluorescent probes and therapeutic chemicals.

Samples consisting of QDs of Si and SiC with mean sizes varied from 2 to 10 nm are usually prepared by using electrochemical etching of bulk c-Si and 3C-SiC in HF-based solution [1, 3]. The obtained highly porous layers are transformed into powders by mechanical grinding (milling). The aqueous suspensions of QDs are prepared and characterized by using dynamic light scattering and optical spectroscopy techniques. The photoluminescence (PL) spectra of Si QDs with sizes of 2–4 nm are characterized by maximum varied from 1.2 to 1.8 eV depending on the QD size. The PL spectra of the 3*C*-SiC QDs suspended in aqueous solutions represent broad bands with maxima in the range from 2.2 to 2.5 eV depending on the size and excitation energies. When the excitation energy decreases from 4 down to 2.5 eV the narrowing and red shift of the PL spectrum was observed. The observed behavior can be well explained by the quantum confinement model. According to this approach the PL properties of QDs are interpreted as a result of the radiative recombination of photoexcited electron-hole pairs (excitons) confined in QDs. In oxygen ambient the PL intensity of Si QDs is found to decrease strongly in comparison with that in vacuum (or in oxygen-free water). The PL quenching in oxygen ambient is maximal at 1.63 eV due to the photosensitization of singlet oxygen generation [6].

According to *in vitro* experiments the singlet oxygen photosensitized by Si QDs suppresses the proliferation of cancer cells of mouse fibroblasts. The DNA analysis of the cancer cells after the interaction with photoexcited Si QDs provides evidences of the apoptosis mechanism of their death [3]. These results demonstrate that Si QDs can be considered as the singlet oxygen photosensitizer in photodynamic therapy (PDT) of cancer and other tumors. It was revealed that the aqueous suspensions of Si QDs with concentration up to 2 g/l were non-toxic for mouse fibroblasts [7] and human cells in darkness. These data demonstrate a rather low level of the cytotoxicity of Si QDs without photoexcitation.

Low cytotoxicity and negligible mutagenicity of Si-based QDs were confirmed *in vivo*. The genotoxic effect of Si QDs assembled in 1-5 μm granules in aqueous media was examined by introducing them intraperitoneally to mice (F_1 CBA x C57BL/6) or white not-pedigree rats at 5, 25 and 50 mg/kg doses [8]. It was found that Si QDs did not show any cytogenetic activity in mice bone marrow cells after 24-hour, 7- and 14-day exposure after a single introduction, but loss of part on the animals was caused by a 50 mg/kg administration. The 5 mg/kg injections of Si QDs at 24-hour

exposure after a single administration caused considerable increase of DNA damage in bone marrow cells and at a 50 mg/kg dose in bone marrow and brain cells. Si QDs did not demonstrate any genotoxic properties in case of 3-hour and 7-day terms of exposure. The experiments on rats did not reveal any teratogenic effects, but their negative influence on body weight gain of pregnant rats and newborns at certain stages of the experiment was determined [7]. It should be noted that the size of Si QDs is usually rather small to trigger the immune response of the body. In contrast to soluble drugs the Si-QDs based suspension can not go far away from targeted tissue or organs after their injection. Furthermore, both the passive (size-depended) and active (functionalized by antibody and etc.) targeting can be utilized for solid nanoparticles. In general, Si-based drugs exhibit strong and long-term therapeutic effects. Note, the introduced Si QDs are biodegradable and the dissolution time in the body depends on their size and pH level of solution [4, 8].

In vitro fluorescent bioimaging was carried out with aqueous suspensions of QDs introduced to cultures cancer cell. After the incubation period and before the observation, the cells are rinsed to eliminate the QDs from their external environment. The fluorescence of the cell cultures marked by QDs is observed by means of fluorescence microscope. The incorporation of QDs inside the living cells was monitored over several hours. Under the optical excitation, the cells marked by QDs are rather bright in order to be distinguished from the fluorescence background of cells. A comparison between the fluorescence micrographs and the microscope photos obtained under white light shows that the QDs are localized inside the cells. Finally, the obtained results demonstrate that Si QDs-based materials are promising for biomedical applications as diagnostics, drug delivery and PDT. The highly luminescent, stable, and biocompatible QDs of Si and SiC with no protective shells can be applied for fluorescence imaging of living cells. Marking of the living cells with QDs highlights the penetration, accumulation, and heterogeneous distribution of the QDs inside the intracellular space.

Aqueous suspensions of Si QDs formed by mechanical grinding porous Si was found to exhibit properties of sonosensitizer, i.e. a material for the activation of ultrasound-induced heating of water and biological systems. A destruction of cancer cells under ultrasound irradiation in the presence of Si QDs has been observed in vitro [9]. This effect can be explained as follows: (1) the cancer cells die because of their local heating induced by oscillating motion of nanoparticles, i.e. because of local hyperthermia; (2) nanoparticles act as "nano-scalpels", which can destroy mechanically the cells; (3) nanoparticles can play a role of cavitation centers, which initiate thermal and mechanical damages in cancer cells. Further experiments are required to clarify the mechanisms of the observed effects.

Acknowledgements

VYT would like to acknowledge Dr. A. A. Kudryavtzev and Prof. A.D. Durnev for their contributions in the biomedical part of the research. Colleagues from the Physics Department of M.V. Lomonosov Moscow State University are acknowledged for the assistance in the sample preparations and investigations. The work was supported by the Russian Foundation for Basic Research and by the Ministry of Education and Science of the Russian Federation.

References

1. F. Pinaud, X. Michalet, L.A. Bentolila et al., *Biomaterials,* 2006, **27**, 1679.
2. J. Botsoa, V. Lysenko, A. Geloen et al., *Apll. Phys. Lett*., 2008, **92**, 173902.
3. V.Yu. Timoshenko, A.A. Kudryavtzev, L.A. Osminkina et al., *JETP Lett.,* 2006, **83**, 423.
4. J. Park, L. Gu, G. von Maltzahn, E. Ruoslahti et al., *Nat. Mater.,* 2009, **8**, 331.
5. R. S. Ajimsha, G. Anoop, A. Aravind, M. K. Jayaraj, *Electrochem. & Solid State Lett.,* 2008, **11** (2), K14.
6. D. Kovalev, E. Gross, N. Kunzner, F. Koch et al., *Phys. Rev. Lett.,* 2002, **89**, 137401.
7. A.D. Durnev, A.S. Solomina, et al., *Bull. Exp. Biol. & Med.,* 2010, **149**, 445.
8. L.T. Canham, *Nanotechnology,* 2007, **18**, 185704.
9. L.A. Osminkina, M.B. Gongalsky, A.V. Motuzuk et al., *Appl. Phys. B.,* 2011, to be published.

ANNIHILATION UPCONVERSION OF NIR PHOTONS IN WATER PHASE: SYNTHESIS, PROPERTIES AND PERSPECTIVES IN BIO APPLICATIONS OF UPCONVERTING NANOCAPSULES

Ch. Wohnhaas[1], A. Turshatov[1], V. Mailänder[1], K. Landfester[1], T. Miteva[3] and S. Baluschev[1,2]

[1] Max-Planck-Institute for Polymer Research, Ackermannweg 10, 55128 Mainz, Germany
[2] Optics and Spectroscopy Department, Faculty of Physics
turshat@mpip-mainz.mpg.de
Sofia University "St. Kliment Ochridski", 5 James Bourchier, 1164 Sofia, Bulgaria
[3] Sony Deutschland GmbH, Materials Science Laboratory, Hedelfingerstr. 61, 70327 Stuttgart, Germany

The process of upconversion (UC) delivers short-wavelengths photons, using a longer wavelength excitation source like near infrared (NIR) or infrared (IR) photons. The fundamental advantages of energetically-conjoined triplet-triplet annihilation supported upconversion [1] (TTA – UC) are the extremely low excitation intensity of light (~50 $mWcm^{-2}$) and low spectral power density (down to 125 μWnm^{-1}) needed. Another important feature of the TTA−UC is the approximately linear dependence of the UC-emission on the excitation intensity. This behavior of the UC-emission might help to predict precisely the necessary radiation dose and to avoid unwanted optical stress of the bio-samples. The mentioned requirement serves TTA-UC as very attractive tool for different applications in the life-sciences field.

With these purposes, the dyes showing effective TTA-UC, a metallated porphyrin (sensitizer) and a fluorophore (emitter) were embedded into the liquid core of polymeric nanocapsules dispersed in water phase. The nanocontainers (Fig. 1A) with an average size of 170 nm were prepared using the process of direct miniemulsion polymerization or solvent evaporation technique. Effect of oxygen quenching TTA-UC is successfully eliminated by protecting polymer shell (10-20 nm thickness). As a result, nanocapsules show upconversion performance even in oxygen containing environment.

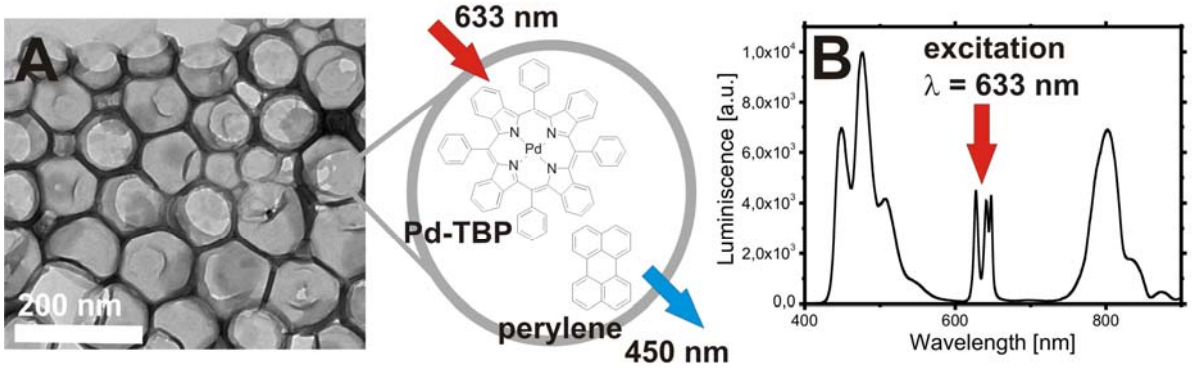

Fig. 1. A – Transmission electron microscopy (TEM) image of the nanocapsules and sketch of chemical structures of upconverting dyes. B – Strong fluorescence of perylene and phosphorescence Pd-TBP are observed, when nanocapsules are excited with λ = 633 nm

Synthesized nanocapsules emit light with wavelength λ = 450-550 nm when NIR excitation is used. Selectivity of excitation and emission wavelengths is simply reached by using combination of different dyes. Thus, TTA-UC nanocapsules could be considered as a local or *in situ* optical excitation source of blue-shifted photons for subsequent light-triggered processes: bioimaging, sensing or photodynamic therapy of cancer.

Acknowledgements

Andrey Turshatov acknowledges the EU-founded FP-7 project EphoCell (N 227127) for the financial support.

References

1. S. Baluschev, T. Miteva, V. Yakutkin, G. Nelles, A. Yasuda, and G. Wegner, *Phys. Rev. Lett.*, 2006, **97**, 143903.

IS THERE A TYPICAL GERMINAL CENTER?

N. Wittenbrink[1] and **M. Or-Guil**[1]

[1] Systems Immunology Lab, Department of Biology, Institute for Theoretical Biology, Humboldt University Berlin and Research Center ImmunoSciences, Charité – Universitätsmedizin Berlin, Germany
nicole.wittenbrink@freenet.de

Immunization with a T cell-dependent antigen leads to the formation of several hundreds of germinal centers (GCs) within secondary lymphoid organs, a key process in the maturation of the immune response [1]. Within the unique multi-cell type environment of GCs, B cells undergo clonal expansion, somatic hypermutation, antigenic selection, class switch recombination and affinity maturation. In addition, both plasma cell commitment and memory B cell formation are linked to the locale of GCs [1].

Since the GC response spans a period of about three weeks, the growth of GCs cannot be followed by real-time imaging and research has to resort to acquisition of time-resolved cross-sectional data. A drawback to the latter is that it allows for determining the average kinetics of the overall GC ensemble, but not necessarily the growth kinetics of individual GCs. Most importantly, as we have shown previously with the aid of mathematical simulations, the empirically observed cross-sectional profile of GC growth is compatible with very different GC ensemble kinetics [2]. A scenario where all GCs emerge almost simultaneously and then grow synchronized, for instance, can result in the same cross-sectional profile than a scenario that allows for asynchronous GC development. Whereas in the first scenario one GC is like the other in terms of size at a given time point, there is no such thing like a typical GC in the second scenario. Which is it then? And what about the cellular composition of GCs – typical or not? These questions are crucial, for mathematical models of affinity maturation often rely on fitting of GC population kinetics to assess the efficiency of presumed selection mechanisms.

By means of computer-aided three-dimensional reconstructions of GCs from histological sections we could show that GC growth is indeed nonsynchronized and that there is no typical GC in terms of size. Acquisition of large-scale confocal data on the cellular composition of GCs in a second study let us further reveal that established GCs have a typical cellular composition, independent of their size and age. The approaches of and results of both studies are summarized in the following.

Broad volume distributions indicate non-synchronized growth and suggest sudden collapses of germinal center B cell populations

While traditional conceptions of affinity maturation tacitly presume simultaneous emergence, growth and decay of GCs, our previous mathematical simulations led us to hypothesize that their growth might be non-synchronized [2]. To investigate this, we performed computer-aided 3-D reconstructions of GCs to measure volume distributions of murine splenic GCs at consecutive time points following immunization of BALB/c mice with a conjugate of 2-phenyloxazolone and chicken serum albumin. For 3-D reconstruction of GCs, whole spleen sections were quadruple stained for proliferating cells (mAb Ki-67), FDC networks (mAb FDC-M2), T cells (mAb CD3) and macrophages (mAb CD68). Digital images of consecutive whole spleen sections were subsequently captured by performing meander scans using a Leica TCS SP2 confocal microscope. Following manual segmentation of GCs as defined by Ki-67 staining and a binarization of the segmented outline, GCs were aligned slice-wise according to their center of mass, using the 3-D reconstruction software Amira (Mercury Computer Systems).

Our analysis revealed broad volume distribution of GCs at all sampled time points (Figure 1), indicating that individual GCs certainly do not obey the average time course of GC volumes and that their growth is non-synchronized [3]. To address the cause and implications of this behavior, we additionally compared our empirical data to simulations of a stochastic mathematical model that allows for frequent and sudden collapses of GCs. Strikingly, this model not only succeeds in reproducing the empirical average kinetics of GC volumes, but also the underlying broad size distributions [3].

Established GCs have a typical cellular composition that is independent of their size and age

While B cells make up for their major cell population, GCs also comprise T cells, macrophages, apoptotic nuclei and stromal follicular dendritic cells (FDC) [1]. The fine processes of FDCs form a

network which histologically divides the GC into two compartments referred to as the dark zone (DZ) and the light zone (LZ). In view of the fact that there is no such thing as typical size [3] nor typical clonal diversity [4] of a GC at a given time point, the question arose whether GCs at least share a typical cellular composition. To address this matter, we acquired large-scale confocal data on GCs during progression of the primary immune response in BALB/c mice. Our database includes three datasets of GC image series derived from different triple immunofluorescence stainings; 1: Ki-67, FDC-M2 and CD3 (Σ=1,130); 2: Ki-67, FDC-M2 and CD68 (Σ=1,289); 3: PNA, TUNEL and CD68 (Σ=1,038). Digital images of GCs, as identified by anatomical location and either Ki-67 or PNA reactivity, were acquired using a Leica DM Ire2 confocal laser-scanning microscope. Recorded GCs and their DZ and LZ compartments were subsequently evaluated as to cross-sectional size and counts of proliferating cells, T cells, macrophages and apoptotic nuclei. An online version of the database (GCImagePresenter) including all images and their appendant data evaluation sheets is available under http://sysimmtools.eu/GCImagePresenter.

The semi-automated image analyses of 3,457 GC sections revealed that established GCs indeed have a typical cellular composition that is independent of their size and age. Given the heterogeneity in size, and likely age, such stable cellular composition of GCs is remarkable. The observed maintenance of quantitative relations between the cellular players during the lifespan of GCs calls for the existence of a tightly regulated network of cellular interactions and communication. It will be particularly interesting to explore how this network achieves its robustness in the highly dynamic environment of a GC.

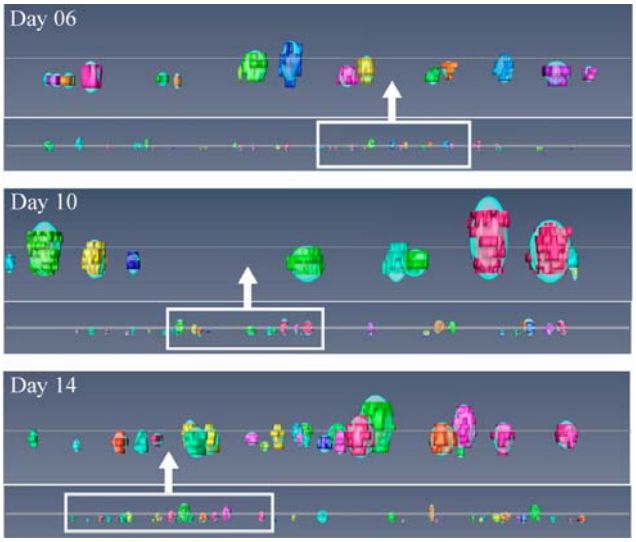

Fig. 1. 3-D reconstructions of GCs were performed using meander scans of immunofluorescence stained serial longitudinal spleen sections. Briefly, GC outlines were segmented and GCs were aligned slice-wise according to their center of mass. After alignment, ellipsoid fitting was performed on GCs (turquoise). Images are representative of spleens obtained at days 6, 10 and 14 after immunization

Acknowledgements

This work was supported by the Volkswagen Foundation and the BMBF (0315005B). The authors especially thank the German Rheumatism Research Center (DRFZ) in Berlin for providing lab space, equipment, generous support and advice during the projects. The authors are further indebted to the Electron and Laser Scanning Microscopy Facility of the Leibniz Institute for Neurobiology in Magdeburg for excellent technical help.

References

1. C.D. Allen, T. Okada, and C.G. Cyster, *Immunity*, 2007, **27**(2), 190-202.
2. M. Or-Guil, N. Wittenbrink, A.A. Weiser, and J. Schuchhardt, *Immunol. Rev.*, 2007, **216**(1), 130-141.
3. N. Wittenbrink, T.S. Weber, A. Klein, A.A. Weiser, W. Zuschratter, M. Sibila, J. Schuchhardt, and M. Or-Guil, *J. Immunol.*, 2010, **184**(3), 1339-1347.
4. J. Faro, and M. Or-Guil, *Mathematical Models in Immune Cell Biology*, Springer, New York, 2011, p.424.

Invited

NEW FUNCTIONS OF THE PROTEASOME AND ITS ROLE IN IMMUNOLOGY

A. Zaikin[1] and **M. Ivanchenko**[2]

[1] University College London, London, UK, e-mail: alexey.zaikin@ucl.ac.uk
[2] University of Nizhny Novgorod, Russia

Proteasome is a complicated molecular machine intended to completely destroy proteins tagged with ubiquitin. Typical *in vitro* experiment proteasomes are mixed with one or several protein substrates and after some time the reaction is stopped. If proteasomes do not have the cups, proteins should be unfolded, e.g. synthetic peptides of known sequence. The proteasomes completely cut proteins into peptides of the length from 1 to 30 amino acids. These resulting peptides can be analysed by the methods of Mass Spectroscopy, because we know the sequence of the substrate and hence can easily calculate all possible products of proteasomal cleavage. It was shown that different sequences have different probabilities to be cut because it is hypothesized that proteasomal terminals analyse a window of amino acids around the cutting peptide bond, and all amino acids in this window have an impact on the probability of the cut. To note, several web based algorithms have been developed to predict the probability of the cut. However, it remains the open question how to predict precisely the cutting points and, hence, the resulting products of proteasomal cleavage.

At the same time the proteasome is a fantastic object for mathematical analysis, especially for modeling of a translocation of proteins inside the proteasome [1] or kinetics of proteasomal degradation [2].

Proteasomal splicing and detection of splicing products

Recently, it was shown that proteasomes not only cleave peptides but also splice it and produce a non-contiguous sequences not found in original substrate. Using CTL reactions several such splicing products have been found [3]. Unfortunately, massive search of new splicing products is really difficult due to the huge number of possible combinations. For example, for the protein of the length 23 amino acids and extein, the piece which is spliced out, of the length 3 amino acid, one can estimate the total number of possible digestion products as 53361, among them 231 cleavage products and 531130 splicing products. It is not possible to study such huge number of possible sequences with Mass Spectroscopy. To overcome this difficulty, in [4] we suggested a new method SpliceMet o for the detection of splicing products, based on a combined use of newly developed computer based algorithm, *in vitro* proteasomal degradation assays and mass spectroscopy. The main idea of the method is the generation of the databank of all possible splicing products, calculation of m/z for them, comparison of this databank with the result of mass spectroscopy methods and then stepwise exclusion of products which do not either present in the databank of demonstrate not logical kinetics. Using this method in [5] several new splicing products have been found including also trans-splicing products, i.e. spliced from two different protein molecules. By this it was shown that proteasome is a real splicing machine, and spliced products can play an important role in the cellular machinery and immunology.

Role of proteasomal splicing in immunology

In addition to the protein degradation proteasomes work as a main supplier of epitopes for MHC Class I antigenic pathway. Proteasome cut out a sequence of 9-12 amino acids which then goes through TAP machinery and couples with MHC molecules to be presented on the cell surface. Immune cells analyse these presented sequences and can evoke the immune response following the epitope recognition.

One of the key processes, for which the epitope structure is central, is the lymphocyte. Thymic maturation of lymphocytes is a coin with two faces. The positive selection brings survival signals to the T-cells that recognize presented self-antigens ‘well’ enough, otherwise launching the apoptotic machinery. The negative selection switches on the apoptotic signaling in the lymphocytes that recognize self-antigens ‘too well’ (currently not known, whether it implies either high cross-reactivity/affinity of TCRs or full T-cell signaling pathway activated), removing, as believed, potentially autoimmune clonotypes. Further selection occurs in the peripheral lymphatic system, where naïve T-cells compete for survival signals from the professional antigen-presenting cells. The

recent results on the modeling side demonstrate the efficiency of this mechanism for the repertoire diversity maintenance [5, 6].

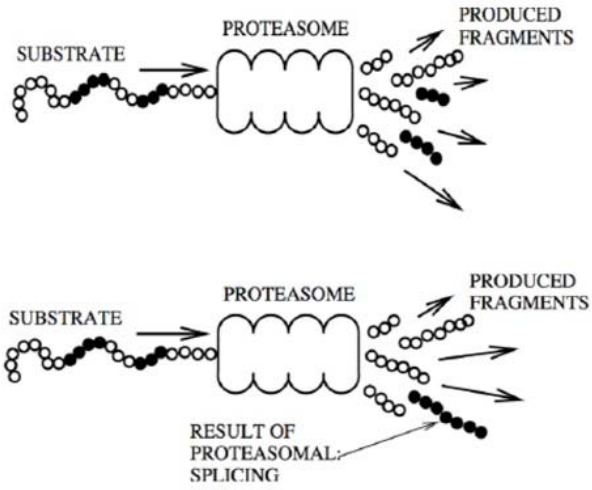

Fig. 1. Schematic illustration of the proteasomal splicing versus production of proteasomal cleavage products.
Top: proteasome cuts initial substrate and produce contiguous sequences of the initial substrate, i.e. cleavage products.
Bottom: proteasome cuts and splices to produce a sequence which does not belong to the initial substrate but spliced from its different parts

As proteasome can indeed produce spliced peptides, the sequences presented to immune response can be not just continuous parts of the proteins expressed in the cell. How our immune system manages to deal with such spliced peptides or epitopes on the both of the selection stages is unclear. The first principal question is whether the proteasomal splicing plays a constructive role in shaping the repertoire diversity. Indeed, during the maturation process the T-cells are presented with the self-peptides and are not able to undergo the positive selection unless they recognize self-antigens. The current view is that extensive thymic negative selection plus the T_{reg} peripheral function are required to avoid massive autoimmune reaction. We hypothesize that the proteasomal splicing can drastically reshape the epitopes and create effectively non-self presentation profiles either in thymus or in the periphery, largely resolving the self-reactivity problem. The second principal question is whether the splicing plays a harmful role. Indeed, rearranging self-antigens too intensively one may derive an epitope that would be identified by the immune system as pathogenic, provoking autoimmune reaction [7].

Answering these questions goes through developing and analyzing the adequate mathematical models, integrating both the proteasomal splicing and lymphocyte selection precesses. We discuss the first steps on this way.

References

1. D.S. Goldobin and A. Zaikin, "Towards quantitative prediction of proteasomal digestion patterns of proteins", *J. Stat. Mechanics*, 2009, P01009.
2. M. Mishto, F. Luciani, E. Bellavista, A. Santoro, K. Textoris-Taube, H.G. Holzhütter, P.M. Kloetzel and C. Francheschi, and A. Zaikin, "Modeling the *in vitro* 20S proteasome activity: the effect of PA28-alphabeta and of the sequence and length of polypeptides on the degradation kinetics", *Journal of Molecular Biology*, 2008, **377,** 1607-1617.
3. N. Vigneron et al., "An Antigenic peptide Produced by Peptide Splicing in the Proteasome", *Science*, 2004, **304**, 587.
4. J. Liepe, M. Mishto, K. Textoris-Taube, K. Janek, C. Keller, P. Henklein, P.M. Kloetzel, and A. Zaikin, "The 20S Proteasome Splicing Activity Discovered by SpliceMet", *PLOS Computational Biology*, 2010, **6**, e1000830; C.J. Tessone, E. Ullner, A. Zaikin, J. Kurths, and R. Toral, "Noise-induced inhibitory suppression of frequency-selective stochastic resonance", *Phys. Rev. E*, 2006, **74**, 046220.
5. E. Stirk, C. Molina-Paris and H. van den Berg, *J. Theor. Biol.*, 2008, **255**, 237.
6. M.V. Ivanchenko, *JETP Letters*, 2011, **93**, 35.
7. P. Cresswell, "Cutting and Pasting Antigenic Peptides", *Science*, 2004, **304**, 525.